Alma Mater Studiorum · Università di Bologna

SCUOLA DI SCIENZE

Dipartimento di Fisica e Astronomia

Corso di Laurea Magistrale in Astrofisica e Cosmologia

A Search for Dark Matter Radio Signatures in the Coma and Abell 2199 Galaxy Clusters

Tesi di Laurea Magistrale

Candidato:
Ruslan Akmetdinov

Relatore:
Chiar.ma
Prof.ssa Annalisa Bonafede

Correlatori:
Dott. Gianni Bernardi
Prof. Marco Regis
Dott. Emilio Ceccotti

Sessione I
Anno Accademico 2025-2026

This Thesis work was done as part of the research activity of the

Istituto di Radioastronomia - Istituto Nazionale di Astrofisica

(Bologna)

Contents

Abstract

Dark matter composes approximately 85% of the matter content of the Universe (Planck Collaboration et al., 2020); however, its particle nature remains unknown. Weakly Interacting Massive Particles (WIMPs) are among the most extensively studied dark matter candidates (Jungman et al., 1996, Bergström et al., 1998, Cirelli et al., 2024). They may produce observable signatures through annihilation or decay processes (Bertone et al., 2005). One promising indirect detection method is the search for synchrotron emission generated by secondary electrons and positrons produced in WIMP annihilation in the presence of magnetic fields in astrophysical environments (Colafrancesco et al., 2006).

The aim of this thesis is to investigate the potential of low-frequency radio observations for constraining WIMP dark matter properties using galaxy clusters as targets. The study focuses on the Coma and Abell 2199 galaxy clusters, which contain dark matter halos with masses of the order of $10^{15}\,M_\odot$ (Łokas and Mamon, 2003, Rines et al., 2002) and host magnetic fields whose properties are known (Bonafede et al., 2010; Vacca et al., 2012). These characteristics make galaxy clusters promising targets for predicting and searching for dark matter-induced synchrotron emission.

A theoretical framework describing the dark matter annihilation process and the resulting synchrotron emission is presented. The expected radio signal was modeled using the DarkMatters code (Sarkis and Beck, 2025) for different WIMP masses and annihilation channels. For the Coma cluster, we used the radio data presented by Bonafede et al. (2022). For Abell 2199, LOFAR observations at 144 MHz were processed (Shimwell et al., 2022) through a complete radio-interferometric analysis pipeline, including data extraction, calibration, imaging, deconvolution, and the search for diffuse emission.

A major challenge of indirect dark matter searches at radio wavelengths is the separation of a potential dark matter signal from radio emission produced by conventional astrophysical processes (Gaskins, 2016).

For the Coma cluster, upper limits on the WIMP annihilation cross section were derived. Assuming the thermal relic annihilation cross section, WIMP masses below approximately 1 TeV are excluded at the 95% confidence level for the $b\bar{b}$ annihilation channel. This result is consistent with recent constraints obtained from γ-ray and radio observations (Geringer-Sameth et al., 2015; Regis et al., 2021)

For Abell 2199, the final residual images were significantly affected by artifacts associated with the bright central radio galaxy 3C 338. These residual structures prevented a reliable extraction of any diffuse component potentially associated with dark matter. Consequently, upper limits on the annihilation cross section were derived using the total residual flux and the RMS noise level. It was shown that this method could potentially place constraints up to WIMP masses of ~ 100 GeV, assuming the thermal annihilation cross section.

The results demonstrate that low-frequency radio observations provide a valuable tool for indirect dark matter searches and highlight the potential of future radio facilities such as the Square Kilometre Array (Weltman et al., 2020) to place significantly stronger constraints on WIMP dark matter.

Chapter 1

Introduction

1.1 Thesis Outline

Despite strong gravitational evidence for the existence of dark matter (DM), its nature remains unknown. Among the most studied candidates are Weakly Interacting Massive Particles (WIMPs), which could either annihilate or decay into Standard Model particles (Bertone et al., 2005; Cirelli et al., 2024). These processes are expected to produce secondary electrons and positrons, which emit synchrotron radiation in the presence of magnetic fields, as well as gamma-rays from prompt emission or inverse Compton scattering on Cosmic Microwave Background (CMB) photons. Such multi-wavelength signatures offer an indirect way to constrain the properties of dark matter.

The purpose of this thesis is to derive upper limits on the WIMP masses with respect to thermal cross-section based on Low-Frequency Array (LOFAR) observations of the Coma and Abell 2199 galaxy clusters.

In Section 1.2, we examine the primary effects and phenomena that provide evidence for the existence of dark matter. These are considered on cosmological scales (Section 1.2.1), on galaxy cluster scales (Section 1.2.2), and on galactic scales (Section 1.2.3).

Next, in Section 1.3, we briefly discuss potential candidates for dark matter. After, in Section 1.4, we focus in more detail on WIMPs as a hypothetical candidate whose parameters will be investigated in the present study. We also outline the main properties of WIMP.

Then, in Section 1.5, we proceed to analyze the phenomenon of WIMP annihilation and its observable signatures, specifically the secondary radiation, which can serve as indirect evidence for the detection of WIMPs.

In Section 1.6, we discuss why the signatures of dark matter annihilation are promising to search for in galaxy clusters. In Section 1.7.1, we explain why these signatures are effectively probed for in the radio frequency range.

In Sections 1.7.2 and 1.8, we review the fundamental principles of radio interferometry and the basics of interferometric image processing. We also justify the choice of the Low-Frequency Array telescope as the primary instrument for the analysis conducted in this study.

Section 1.9 is devoted to the statistical methods used to reconstruct the parameters of both the dark matter profile and the astrophysical component.

Section 1.A describes how magnetic field profile is probed in galaxy clusters, and Section 1.B presents dark matter distribution in galaxy cluster.

Chapter 2 is devoted to the analysis of dark matter in the Coma cluster. Section 2.1 provides an overview of the main properties of the cluster. Section 2.2 describes the radio emission data that form the basis of the subsequent analysis.

Section 2.4 presents a detailed discussion of the radio emission induced by dark matter annihilation. The dependence of the predicted signal on the dark matter model parameters, including the WIMP mass, annihilation cross section, and annihilation channel, is investigated.

In Section 2.5 an analytical model of the expected emission is also constructed and later used for fitting the observational data.

Subsequently, Section 2.6 presents simulations of the dark matter and astrophysical signals together with the reconstruction of the input parameters. These simulations are used to assess the performance of the method and to identify its limitations and range of applicability.

Finally, in Section 2.7, the developed statistical methodology is applied to the Coma cluster data. Based on this analysis, upper limits on the dark matter mass are derived.

The Chapter 3 focuses on the search for induced dark matter emission in the Abell 2199 galaxy cluster. The chapter is organized into three main parts. Section 3.1 summarizes the main properties of the Abell 2199 galaxy cluster. Section 3.2 details the calibration and processing of the radio observations. Section 3.3 examines the extraction of astrophysical information and diffuse radio emission from the processed data and presents the resulting constraints on WIMP dark matter properties.

The results and conclusions are presented in Chapter 4.

1.2 Astrophysical Evidence for Dark Matter

1.2.1 Cosmological Framework

Cosmic Microwave Background (CMB) observations strongly indicates that the Universe on the large scales (larger than 200 Mpc) is nearly spatially flat and the observed density is close to the critical one, defined as:

$$\rho_0 \approx \rho_{\rm cr} = \frac{3H_0^2}{8\pi G} \approx 9 \cdot 10^{-27}\ \mathrm{kg/m^3}\,, \tag{1.1}$$

where $G \approx 6.67 \cdot 10^{-11} \frac{\mathrm{m^3}}{\mathrm{kg \cdot s^2}}$ is the gravitational constant and $H_0 \simeq 67.4 \pm 0.5 \frac{\mathrm{km}}{\mathrm{s \cdot Mpc}}$ is the Hubble constant at the present epoch (Planck Collaboration et al., 2020), which described the expansion of the Universe:

$$H_0 = \frac{\dot{a}}{a}. \tag{1.2}$$

Here $a = a(t)$ is the scale factor, it describes how the overall size of the Universe changes with time.

In the late 1990s, Riess et al. (1998) and Perlmutter et al. (1999) discovered accelerated expansion of the Universe based on observations of Type Ia supernovae. They expressed the scale factor $a(t)$ as a Taylor series (Coles and Lucchin, 2002, more details in section 1.6):

$$a(t) = a(t_0) + \dot{a}(t_0)(t - t_0) + \frac{1}{2}\,\ddot{a}(t_0)(t - t_0)^2 + \dots\,. \tag{1.3}$$

where t_0 is the present epoch and t is the arbitrary time in the vicinity of t_0 at which the scale factor is evaluated. We introduce a new parameter:

$$q_0 = -\frac{\ddot{a}(t_0)a(t_0)}{\dot{a}^2(t_0)}\,, \tag{1.4}$$

which characterizes whether the expansion of the Universe is accelerating or decelerating. We substitute H_0 using Hubble law (Eq. 1.2) and applying the definition for q_0, rewrite Eq. 1.3 as

$$a(t) = a(t_0)\left[1 + H_0(t - t_0) - \frac{q_0}{2}H_0^2(t - t_0)^2 + \dots\right]. \tag{1.5}$$

This parameter (q_0) depends on the chosen cosmological model. The current standard model is the ΛCDM, in which the Universe is assumed to be homogeneous and isotropic on large scales and composed primarily of cold dark matter (CDM) and the dark energy represented by the cosmological constant Λ is associated to the accelerated expansion of the Universe (Dodelson and Schmidt, 2020, section 1.6).

In a spatially flat Universe, the present-day deceleration parameter is determined by the matter (cold dark matter and baryonic matter) and dark energy density parameters, $\Omega_{m,0}$ and $\Omega_{\Lambda,0}$, respectively. Here, $\Omega_i = \rho_i/\rho_0$, where ρ_i is the density of a given component and ρ_0 is the critical density (see Eq. 1.1).

In a spatially flat Universe, the present-day deceleration parameter is determined by the matter (cold dark matter and baryonic matter) $\Omega_{m,0}$ and dark energy $\Omega_{\Lambda,0}$ density parameters, where $\Omega = \rho/\rho_0$, where ρ is the density for a specific component, according to:

$$q_0 = \frac{\Omega_{m,0}}{2} - \Omega_{\Lambda,0}, \qquad \Omega_{m,0} + \Omega_{\Lambda,0} = 1\,. \tag{1.6}$$

Thus, the relative contributions of matter and dark energy determine whether the expansion of the Universe decelerates ($q_0 > 0$) or accelerates ($q_0 < 0$). Using the present-day values $\Omega_{m,0} \approx 0.3$ and $\Omega_{\Lambda,0} \approx 0.7$ (Planck Collaboration et al., 2020), we obtain:

$$q_0 \approx -0.55\,, \tag{1.7}$$

which implies an accelerated expansion of the Universe and the dominance of dark energy at the present epoch. This result is consistent with the observations of Type Ia supernovae reported by Riess et al. (1998) and Perlmutter et al. (1999).

Baryonic Acoustic Oscillations and CMB power spectrum

Prior to the Cosmological recombination, baryonic matter and radiation were tightly coupled. Photons were continuously scattered by free electrons through inverse Thomson scattering, thereby smoothing out primordial density inhomogeneities. As a consequence, matter was unable to cluster and form large-scale structures. The coupled baryon–photon fluid exhibited acoustic oscillatory behavior, commonly known as *baryon acoustic oscillations* (BAOs) see (Dodelson and Schmidt (2020, section 8.6)).

These baryon–photon acoustic waves oscillated within the gravitational potential wells determined by the evolution of dark matter density perturbations, which, after the matter–radiation equality and during the subsequent matter-dominated era, were able to grow freely through gravitational instability. Thus, the gravitational potential generated by dark matter acted as a driving force for the acoustic oscillations.

This feature, namely the presence of a driving force, leads to an asymmetry in the amplitudes of the even and odd peaks (overtones) of the BAOs. By analyzing the relative heights of these peaks, one can infer the abundance of dark matter (see Fig. 1.1).

BAOs can be observed in the anisotropy pattern of the CMB temperature distribution. These anisotropies exhibit a strong scale dependence, which can be described in Fourier space. In mathematical terms, this is represented by the power spectrum of CMB temperature fluctuations, schematically shown in Fig. 1.1. For further details, see Dodelson and Schmidt (2020, chapter 9) and Balazs et al. (2026).

The results of Planck Collaboration et al. (2020), based on measurements of the CMB anisotropies, give the value of the cold dark matter density parameter as $\Omega_c h^2 = 0.120 \pm 0.001$, corresponding to $\Omega_c = 0.264 \pm 0.006$, where Ω_c denotes the present-day fractional energy density of cold dark matter relative to the critical density.

Non-linear Perturbations Growth and Large Structure Formation

Observational data indicate that the Universe is homogeneous on scales larger than approximately 100–200 Mpc (Hogg et al., 2005; Scrimgeour et al., 2012). However, when examined on smaller scales, a rich and complex structure emerges, including voids, sheets, filaments,

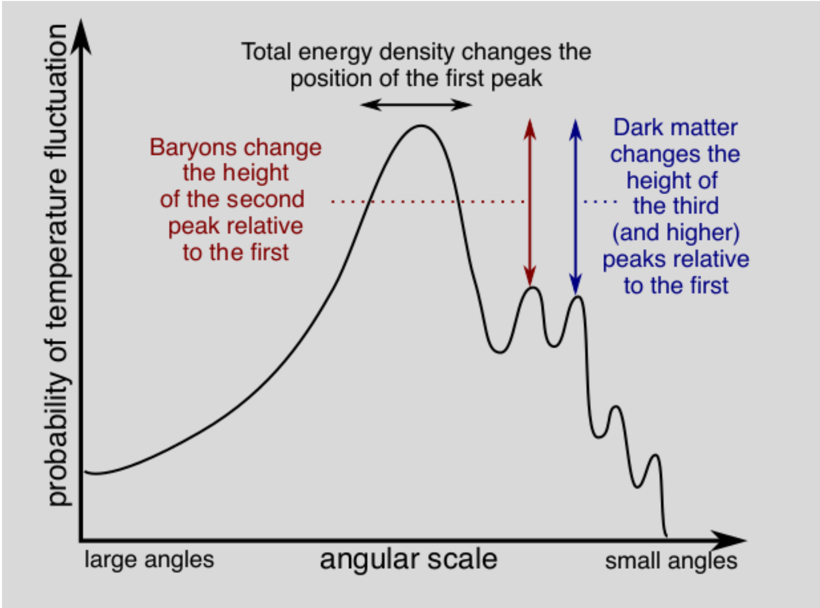

Figure 1.1 This image is a schematic representation of the observed power spectrum of CMB temperature anisotropies from Balazs et al. (2026). The geometry of the peaks: their positions and relative heights—allows one to constrain the fundamental cosmological parameters of our Universe, such as Ω_Λ, Ω_c, Ω_b, H_0, among others.

clusters and other features of the cosmic web. The inhomogeneity of the Universe can be characterized by the density contrast δ:

$$\delta_b = \frac{\delta\rho}{\rho}. \tag{1.8}$$

where $\delta\rho$ is a density perturbation and ρ is the mean background density. Based on measurements of the CMB power spectrum, the amplitude of density perturbations at the recombination was of order 10^{-5} (Planck Collaboration et al., 2020). In contrast, in the present epoch these inhomogeneities have grown significantly, reaching values of 10^3 up to 10^6 in the central regions of galaxy clusters (Cirelli et al., 2024, section 1.3.1).

We will now briefly illustrate that the growth of density perturbations would not have been possible without the presence of dark matter. For a detailed discussion of perturbation theory, see Cirelli et al. (2024, section 1.3.1), or Coles and Lucchin (2002, part 3).

In perturbation theory, one obtains an equation describing the evolution of the growth of density perturbations, $\delta(k)$, where $k = 2\pi/\lambda$ is the wave vector corresponding to the perturbation scale:

$$\frac{\partial^2\delta_k}{\partial t^2} + 2H\frac{\partial\delta_k}{\partial t} + \left(\frac{v_s^2 k^2}{a^2} - 4\pi G\rho\right)\delta_k = 0, \tag{1.9}$$

where v_s is the sound speed in the baryon–photon fluid.

Non-clustering of baryonic matter. In the early Universe, baryonic matter (protons, neutrons, and electrons) was tightly coupled to photons.The sound speed in the baryon–photon plasma was of the order of $v_s \sim c/\sqrt{3}$, resulting in pressure forces that exceeded gravitational attraction on small scales. Therefore, we can neglect the gravitational term in Eq. 1.9, since $4\pi G\rho_0 \ll \frac{v_s^2 k^2}{a^2}$. The evolution of baryonic density perturbations in this regime is described by

$$\frac{\partial^2\delta_k}{\partial t^2} + 2H\frac{\partial\delta_k}{\partial t} + \frac{v_s^2 k^2}{a^2}\delta_k = 0\,. \tag{1.10}$$

In the matter dominated era scale factor was $a(t) = (\frac{3}{2}tH_0)^{2/3}$ (see Dodelson and Schmidt, 2020, section 1.1) and substituting these expressions into the equation 1.10, we obtain

$$\frac{\partial^2 \delta_k}{\partial t^2} + \frac{4}{3t}\frac{\partial \delta_k}{\partial t} + \frac{v_s^2 k^2}{(\frac{3}{2}H_0)^{4/3} t^{4/3}}\delta_k = 0. \tag{1.11}$$

The solution of this equation describes the acoustic oscillations:

$$\delta_k = \frac{c_1 \cos\left(c_0 k t^{1/3}\right) + c_2 \sin\left(c_0 k t^{1/3}\right)}{k t^{1/3}}, \tag{1.12}$$

which corresponds to a pressure wave. The parameters c_0, c_1, and c_2 are functions of H_0 and v_s. As a result, baryonic density perturbations could not grow significantly until recombination at $z \simeq 1100$. Here, the redshift z is related to the scale factor by:

$$z = \frac{1}{a} - 1\,. \tag{1.13}$$

Thus, before recombination, the perturbations had only an oscillatory behavior, and their growth was effectively suppressed until the decoupling epoch, when baryonic matter began to cluster gravitationally. The qualitative scheme of baryonic perturbation growth is presented in the left panel of Fig. 1.2. Moreover, the amplitude of these perturbations can be determined from the CMB power spectrum.

Dark matter clustering. In the case of dark matter, in the matter dominated era, which is collision-free and pressure-free, the pressure term $\frac{v_s^2 k^2}{a^2}$ can be neglected. Then, Eq. 1.9 reduces to the following form:

$$\frac{\partial^2 \delta_k}{\partial t^2} + 2H\frac{\partial \delta_k}{\partial t} - 4\pi G \rho_0 \delta_k = 0. \tag{1.14}$$

Expressing ρ_0 in terms of the Hubble and the gravitational constants (see Eq. 1.1), we obtain

$$\frac{\partial^2 \delta_k}{\partial t^2} + \frac{4}{3t}\frac{\partial \delta_k}{\partial t} - \frac{2}{3t^2}\delta_k = 0\,, \tag{1.15}$$

giving

$$\delta_k = c_g t^{2/3} + c_d t^{-1}\,, \tag{1.16}$$

where c_g and c_d are integration constants associated with the growing and decaying modes of the density perturbation. Thus, dark matter perturbations began to grow significantly before the recombination. After decoupling, baryonic matter follows the inhomogeneities of dark matter. Schematically, this is shown in the right panel of Fig. 1.2.

For completeness, it should be noted that in the radiation-dominated era (before $z \simeq 3400$), dark matter clustering was suppressed. In this epoch, where $H = 1/(2t)$ (see Dodelson and Schmidt, 2020, section 1.1), both terms in the third component of Eq. 1.9 can be neglected because $v_s = 0$ for the dark matter fluid. In this regime, δ_k corresponds to density fluctuations of the radiation field. However, these radiation perturbations do not cluster and therefore do not contribute to the gravitational potential.

$$\frac{\partial^2 \delta_k}{\partial t^2} + \frac{1}{t}\frac{\partial \delta_k}{\partial t} = 0\,, \tag{1.17}$$

giving

$$\delta_k \sim \ln t + \text{const.} \tag{1.18}$$

Thus, dark matter effectively began to cluster after the matter-radiation equality at $z \simeq 3400$.

The growth of density perturbations from recombination to the present time is highly nonlinear, a behavior that can be explained by the presence of dark matter. The assembly of dark matter structures begins earlier, and baryonic matter subsequently follows the dark matter distribution through gravitational infall. In this framework, dark matter dominates the gravitational potential, so that baryons effectively behave as a tracer of the underlying dark matter density field on large scales.

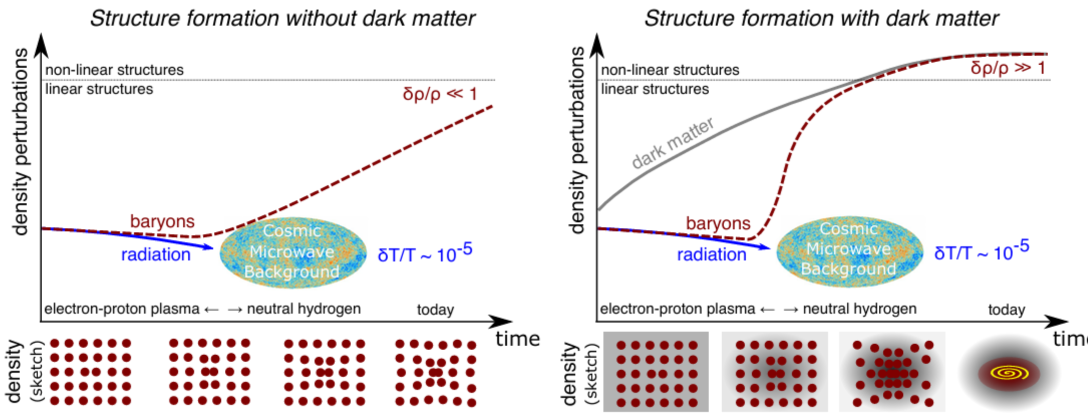

Figure 1.2 Illustration of the formation of large-scale structure in the Universe without (left) and with (right) dark matter. Adapted from Balazs et al. (2026).

1.2.2 Dark Matter in Galaxy Clusters

Weak Gravitational Lensing

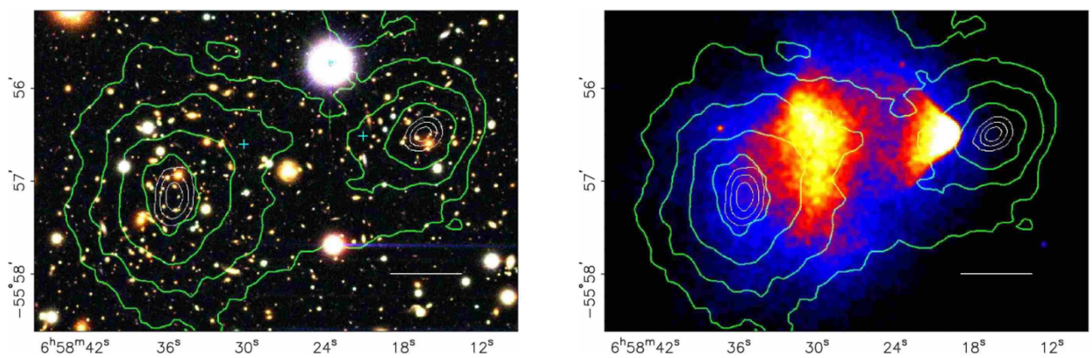

Figure 1.3 Merging galaxy cluster. In the right panel, the red and blue colors represent the X-ray luminosity observed with *Chandra*, tracing the distribution of the intracluster gas. The contours (both left and right) indicate the total mass distribution inferred from gravitational lensing constraints. The white bar corresponds to 200 kpc at the cluster distance. Adapted from Clowe et al. (2006).

Another important evidence for the existence of dark matter comes from observations of galaxy clusters during merging events. One of the most prominent early examples is the *Bullet Cluster*, reported by Clowe et al. (2006).

The majority of baryonic matter in galaxy clusters is contained in the hot intracluster gas, whose mass distribution, density, and temperature can be inferred from X-ray observations. In addition, the total mass distribution can be reconstructed using gravitational lensing techniques (see Fig. 1.3). These observations reveal a spatial separation between the dark matter component and the baryonic (gas) component.

This can be understood as follows. Initially, two galaxy clusters, each containing both dark matter and baryonic matter, were gravitationally bound systems. During the collision, the gaseous components of the clusters interacted strongly, producing shock waves and being decelerated. In contrast, the dark matter components, which interact only weakly (or not at all) with themselves and with baryonic matter, passed through each other largely unaffected. For a detailed discussion of this interpretation, see, e.g., Cirelli et al. (2024).

Dark and Baryonic Matter in Galaxy Clusters

The total mass of a galaxy cluster can be estimated using the virial theorem. For a bound system, the time-averaged kinetic energy $\langle K\rangle$ and the time-averaged gravitational potential energy $\langle U\rangle$ are related by

$$\langle K\rangle = -\frac{1}{2}\langle U\rangle. \tag{1.19}$$

Let us consider a simplified galaxy cluster of radius R, consisting of $N \gg 1$ identical galaxies, each of mass m. In this case, the virial theorem can be written in the following form:

$$N\frac{mv^2}{2} = \frac{1}{2}\frac{3}{5}\frac{G(Nm)^2}{R}. \tag{1.20}$$

The total mass of the cluster can then be expressed as

$$M_{tot} = Nm = \frac{5}{3}\frac{v^2R}{G}. \tag{1.21}$$

Using this approach, Zwicky (1933) suggested that the actual mass of a galaxy cluster is significantly greater than the visible mass (i.e., stars and gas).

Since the 1980s, X-ray astronomy has enabled more accurate estimates of both the total mass of galaxies and their gaseous component. These studies focus on the hot intracluster gas, which is assumed to be in hydrostatic equilibrium:

$$\frac{dP_g}{dr} = -g\rho_g \tag{1.22}$$

Here, P_g and ρ_g denote the gas pressure and density, respectively. Assuming the gas behaves as an ideal gas, we can write

$$P_g = \frac{T_g k_B \rho_g}{m_p\mu} \tag{1.23}$$

where k_B is the Boltzmann constant, μ is the mean molecular weight, m_p is the proton mass, and T_g is the gas temperature. Combining these equations and eliminating the pressure, we obtain

$$\frac{dT_g}{dr}\frac{k_B\rho_g}{m_p\mu} + \frac{d\rho_g}{dr}\frac{k_bT_g}{m_p\mu} = -g\rho_g \tag{1.24}$$

Finally, we can express the gas density

$$\frac{d\ln\rho_g(r)}{dr} = -\frac{m_p\mu}{k_BT_g(r)}\frac{GM_{tot}}{r^2} - \frac{d\ln T_g(r)}{dr} \tag{1.25}$$

The gas temperature profile, $T_g(r)$, and its logarithmic gradient, $d\ln T_g(r)/dr$, can be measured from X-ray observations. The total gas mass could then be estimated as

$$M_g = \int 4\pi r^2\rho_g(r)dr \tag{1.26}$$

Studies (e.g., Vikhlinin et al., 2006) show that the gas fraction, $M_g/M_{\rm tot}$, within r_{500} ranges from ~ 0.06 to 0.14, depending on the gas temperature. When corrected for the contribution of stellar components, this ratio is referred to as the *baryonic fraction*, $f_b \sim 0.16$.

1.2.3 Dark Matter on the Galactic Scales

Spiral Galaxy Rotation Curves

Spiral galaxies rotate around their symmetry axis. Their rotation velocities can be measured using the Doppler effect, through the frequency shift of the neutral hydrogen HI 21 cm emission line. Based on these measurements, Rogstad and Shostak (1972) construct the rotational velocity of a galaxy as a function of the distance from the galactic center.

The total mass of a galaxy enclosed within a radius r and its circular rotation velocity can be estimated using Newtonian:

$$v_{circ}(r) = \sqrt{\frac{GM(r)}{r}} \quad \Rightarrow \quad M(r) = \frac{v_{circ}^2(r)r}{G} \tag{1.27}$$

Rogstad and Shostak (1972), using observations of different galaxies, showed that the total mass of neutral hydrogen HI accounts for only $\sim 11\%$ of the total galactic mass. This behavior implies the presence of an additional, unseen mass component, such as an extended dark matter halo.

In Fig. 1.4 from Cirelli et al. (2024), the rotation curves of two galaxies are shown, together with the contributions of different components—disk, bulge, gas, and dark matter—to the total rotation velocity of the system. The observed rotation curves do not decline with radius as would be expected from the stellar and gas components alone, which indicates the presence of an additional, spatially extended dark matter component beyond the optical disk that maintains the approximately flat rotation profile at large radii (Rubin et al., 1978; Sofue and Rubin, 2001; de Blok et al., 2008).

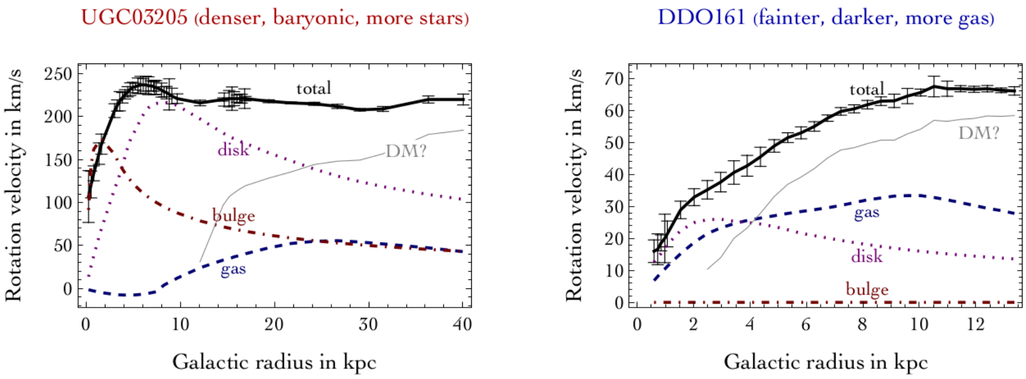

Figure 1.4 Galaxy rotation curves for star-rich (left) and gas-rich (right) galaxies. The different curves represent the contributions from the disk, bulge, gas, and an additional unseen mass component. Adapted from Cirelli et al. (2024).

1.3 Dark Matter Candidates

In this section, we discuss several leading candidates that could account for the nature of dark matter and some basic properties of it. Some of these candidates are illustrated in Fig. 1.5.

Dark matter candidates can be classified into several categories. For example, they may include modifications of gravity, such as those highlighting the limitations of general relativity. They could also be light bosons: *axions* and *axion-like particles* (ALPs), standard neutrinos, or a new type called *sterile neutrinos*. Alternatively, candidates may be large macroscopic objects, such as *MACHOs* or *primordial black holes*. In this thesis, we will focus on Weakly Interacting Massive Particles, shortly *WIMPs*. However, before doing so, let us briefly discuss the other candidates.

1.3.1 Neutrinos

According to the Standard Model, our Universe contains hundreds of neutrinos per cubic centimeter of space. These neutrinos fill the Universe much like the CMB photons. Their

Figure 1.5 Schematic representation of possible candidates for dark matter. From Bertone and Tait (2018).

temperature is slightly lower than that of the CMB, given by $T_\nu = \left(\frac{4}{11}\right)^{1/3} T_\gamma \approx 1.95$ K. This is because neutrinos decoupled from the cosmic plasma earlier, at temperatures of the order of MeV, and their temperature subsequently decreased with the expansion of the Universe, whereas photons were slightly heated during the annihilation of electrons and positrons at $T \sim 0.5$ MeV. Therefore, the total amount of neutrinos could be estimates as

$$n_\nu = 3\frac{3}{4}\frac{2\zeta(3)}{\pi^2}T_\nu^3 \approx 336 \ \text{cm}^{-3} \tag{1.28}$$

The factor of 3 accounts for the three neutrino flavors (ν_e, ν_μ and ν_τ). The factor of 3/4 appears because neutrinos are fermions and therefore obey Fermi–Dirac statistics (as opposed to bosons, which follow Bose–Einstein statistics). And n_ν corresponds to the total number density of all neutrino and antineutrino species today.

In 2015, the Nobel Prize was awarded to Takaaki Kajita and Arthur McDonald for the discovery of neutrino neutrino oscillations, which shows that neutrinos have mass. For instance, measurements indicate that the lower bound on the sum of neutrino masses is approximately 0.06 eV (Fukuda et al., 1998). Thus, we can estimate the contribution of neutrinos to the total energy density of the Universe, Ω_ν

$$\Omega_\nu = \frac{n_\nu \langle m_\nu \rangle}{\rho_0} \approx 1.4 \cdot 10^{-3} \tag{1.29}$$

In the Standard Model, neutrinos can account for no more than 1% of the dark matter abundance in the Universe. For more details, see Dodelson and Schmidt (2020, section 2.4.4).

1.3.2 MACHO

Since the 1980s, the hypothesis that dark matter could consist of Massive Astrophysical Compact Halo Objects (MACHOs) has been widely discussed (Hegyi and Olive, 1983, Alcock et al., 1995). MACHOs could include planets, faint stars, brown dwarfs, or black holes. However, such dark matter would be baryonic, which is strongly disfavored by observations of CMB anisotropies, indicating that the vast majority of dark matter must be non-baryonic and cold.

At present, MACHOs are primarily of historical interest. For example, microlensing studies, such as Optical Gravitational Lensing Experiment (Udalski et al., 2015, OGLE) and Mróz et al. (2024), conducted in the Milky Way and the Large Magellanic Cloud, have demonstrated that no more than $\sim 10\%$ of a galaxy's dark matter halo can consist of MACHOs in the mass range 10^{-5}–$10^{3}\,M_{\odot}$.

1.3.3 Primordial Black Holes

A compelling dark matter candidate is primordial black holes (PBHs). Black holes with a wide range of masses, from 10^{-5} g to $10^{5}, M_{\odot}$, could have formed in the early Universe as a result of extreme compression associated with the Big Bang. For more details see Carr et al. (2021) or Cirelli et al. (2024, section 3.1.1).

Low-mass PBHs, with $M \lesssim 10^{-18}\,M_{\odot}$, according to Hawking radiation (Hawking, 1974), would lose mass so rapidly that they would not have survived to the present day. More massive PBHs, up to $10^{-16}\,M_{\odot}$, at the current stage of cosmic evolution would emit gamma- and X-ray radiation during their evaporation; however, such emission or signatures of this emission is not detectable by instruments such as *INTEGRAL* or *Voyager-1*, the latter having measured the electron–positron flux.

PBHs in the mass range $5 \times 10^{-15}\,M_{\odot}$ to $10^{-13}\,M_{\odot}$ can be ruled out Cirelli et al. (2024, section 1.3.1), as such black holes could collide with white dwarfs or neutron stars, subsequently accreting their material and potentially triggering supernova explosions at rates far exceeding what is currently observed. This places strong limits on dark matter candidates in this mass range.

Objects of higher mass from $10^{-11}M_{\odot}$ to $10^{-6}M_{\odot}$ have also been excluded through microlensing observations conducted by the Subaru HSC experiment (Niikura et al., 2019).

1.3.4 Particle Candidates

Since the late 1980s particle DM paradigm are widely discussed (Bertone and Tait, 2018). Any viable particle dark matter candidate must satisfy a number of cosmological and astrophysical constraints. DM is required to be cold, namely non-relativistic at the cosmological recombination. This condition is essential for the formation of large-scale structure in the Universe.

Furthermore, dark matter must be electrically neutral or, at most, carry an extremely small electric charge, since otherwise it would interact with photons via electromagnetic forces, which is not observed. Moreover, cosmological observations (Planck Collaboration et al., 2020) show that dark matter behave as a collisionless fluid. Thus, its interaction cross-section must be significantly smaller than the characteristic strong nuclear cross section (i.e. $\sim 10^{-26}\,\mathrm{cm}^{2}$), see Cirelli et al. (2024, section 3.3)

Among the numerous particle dark matter candidates, sterile neutrinos (see Section 1.3.1), axion-like particles (ALPs), and weakly interacting massive particles (WIMPs) are among the most widely studied. Since the present work is devoted to searching for signatures of WIMP annihilation, we discuss the relevant WIMP properties and parameters in more detail in Section 1.4.

1.4 WIMP Parameters

In this section, we discuss the main constraints on the parameters of Weakly Interacting Massive Particles (WIMPs). The Tremaine–Gunn criterion, which establishes a lower bound on the WIMP mass, is presented in Section 1.4.1. In the following Section 1.4.2 the upper limit on the WIMP mass is discussed. Then, in Section 1.4.3, we examine the freeze-out effect and the associated constraint on the annihilation cross-section, the so-called *thermal* or *relic* WIMP annihilation cross-section, $\langle\sigma v\rangle \approx 3 \times 10^{-26}$ cm^{3}s^{-1}. This represents one of the key constraints on WIMP properties. Finally, in Section 1.4.4, we provide an overview of experiments probing the parameter space of WIMPs.

1.4.1 Lower Limit of the WIMP Mass

Tremaine and Gunn, 1979 derived a lower bound on the mass of fermionic dark matter particles by applying the Pauli exclusion principle to dark matter in galaxies. Within a unit phase-space element, no more than g dark matter particles can be present, where g is the number of internal degrees of freedom. This leads to the constraint

$$n < g\frac{p^3}{h^3}, \tag{1.30}$$

where n is the number density of dark matter particles and $p = M_\chi \sigma_v$ is the characteristic momentum, taken as the product of the particle mass and its typical velocity.

We identify this velocity as the velocity dispersion σ_v, which can be estimated from the virial theorem:

$$\sigma^2 \approx \frac{GM}{R} \approx G\rho R^2, \tag{1.31}$$

where ρ is the mean mass density of the system.

Expressing the number density as $n = \rho/m_\chi$ and substituting Eqs. (1.30) and (1.31), we obtain

$$m_\chi > \left(\frac{h^3}{gG\sigma R^2}\right)^{1/4} \approx 40\,\mathrm{eV}. \tag{1.32}$$

Thus, the Tremaine-Gunn argument places a lower bound of several tens of eV on the mass of fermionic dark matter, adopting representative values $\sigma_v \approx 100$ km/s and $R \approx 10$ kpc.

1.4.2 Upper Limit on the WIMP Mass

Griest and Kamionkowski (1990) derived a fundamental upper bound on the WIMP mass. In their approach, the particle wave function is expanded in terms of spherical harmonics, leading to an asymptotic expansion of the annihilation cross-section in powers of the relative velocity:

$$\langle\sigma v\rangle = a + bv^2 + \dots$$

which contains only even powers of v in this expansion, as odd terms would violate spatial symmetry.

During freeze-out (see Section 1.4.3), the WIMP mass exceeds the temperature of the Universe by a factor of $\sim$ 20–30. In this regime, dark matter particles can be treated as non-relativistic. Consequently, the expansion of the annihilation cross-section is typically truncated after the first few terms, corresponding to the so-called s-wave (constant), p-wave (v^2), and d-wave (v^4) contributions.

For particles in thermal equilibrium in the early Universe, partial-wave unitarity of the S-matrix imposes an upper limit on the annihilation cross section. Because the relic abundance scales inversely with the annihilation cross section, $\Omega_c \propto \langle\sigma v\rangle^{-1}$ (see Section 1.4.3), this upper limit implies a lower bound on the relic abundance, which grows with mass. By requiring that this does not exceed the observed dark-matter density, we obtain an upper bound on the WIMP mass.

As a result, stable elementary particles with masses exceeding approximately 340 TeV are strongly disfavored within the standard thermal WIMP scenario.

Smirnov and Beacom (2019) included the effects of Sommerfeld enhancement and showed that this upper bound is reduced to approximately 140 TeV for self-conjugate dark matter particles and 100 TeV for non-self-conjugate particles.

1.4.3 Thermal Production of WIMPs

The history of a generic WIMP begins at very early times (high temperature), when the WIMP was in equilibrium with the rest of the cosmic plasma. As the Universe expanded and cooled, the particle underwent *freeze-out*, when the annihilation rate dropped below the expansion rate.

In this section we solve the Boltzmann equation for such particles to determine the freeze-out epoch and relic abundance. For more details see Dodelson and Schmidt (2020, section 4.4).

The Boltzmann equation for interacting particles in an expanding Universe is given by

$$\frac{\partial n_1}{\partial t} + 3Hn_1 = n_1^{(0)} n_2^{(0)} \langle \sigma v \rangle \left(\frac{n_3 n_4}{n_3^{(0)} n_4^{(0)}} - \frac{n_1 n_2}{n_1^{(0)} n_2^{(0)}} \right) \tag{1.33}$$

Here $\langle \sigma v \rangle$ is the thermally averaged cross section, and n_i is the number density of i-th species, and $n_i^{(0)}$ is the same distribution but in thermal equilibrium. We assume the following reaction

$$\chi + \chi \leftrightarrow \psi + \psi \tag{1.34}$$

where two WIMPs χ annihilate into two Standard Model particles ψ. In the early hot Universe this reaction could proceed in both directions. The quantities n_1 and n_2 denote the number densities of dark matter particles, while n_3 and n_4 describe the number densities of Standard Model particles. We assume that all Standard Model particles remain in thermal and chemical equilibrium, so that their number densities satisfy $n_3 = n_3^{(0)}$ and $n_4 = n_4^{(0)}$. We also consider a single dark matter species, such that $n \equiv n_1 = n_2$. Thus, we obtain

$$\frac{\partial n}{\partial t} + 3Hn = n^{(0)} n^{(0)} \langle \sigma v \rangle \left(1 - \frac{n \cdot n}{n^{(0)} \cdot n^{(0)}} \right). \tag{1.35}$$

The left part of this equation could be expressed as

$$\frac{dn}{dt} + 3Hn = a^{-3} \frac{d}{dt}(a^3 n) \tag{1.36}$$

Let's call $n^{(0)} = n_{eq}$ and obtain

$$a^{-3} \frac{d}{dt}(a^3 n) = \langle \sigma v \rangle \left(n_{eq}^2 - n^2 \right). \tag{1.37}$$

We now do two changes of variables. First, we introduce Y

$$Y = \frac{n}{T^3} \text{ and } Y_{eq} = \frac{n_{eq}}{T^3}, \tag{1.38}$$

from which Eq. 1.37 becomes

$$\frac{dY}{dt} = T^3 \langle \sigma v \rangle \left(Y_{eq}^2 - Y^2 \right). \tag{1.39}$$

Secondly, we change the time variable from t to x, defined as

$$x = \frac{M_\chi}{T} \text{ and } dx = xHdt. \tag{1.40}$$

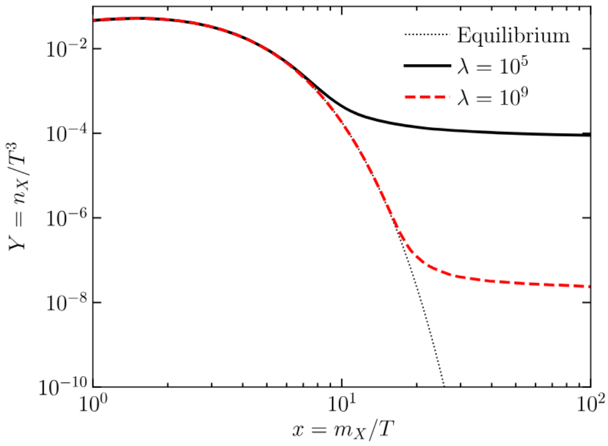

Figure 1.6 The number-density abundance of a WIMP χ as a function of x, where $x = M_\chi/T$. x is proportional to the scale factor $x \propto a$. The dashed curve represents the equilibrium number density. The two solid curves correspond to the abundance of the DM for two distinct values of λ. The parameter λ describes the the ratio between the Hubble expansion rate and the annihilation rate. From Dodelson and Schmidt (2020, section 4.4)

.

At early cosmic time, the expansion of Universe was dominated by radiation, whose energy-density is proportional to T^4. By replacing this in Eq. 1.52, we obtain

$$H \propto \sqrt{\rho} \propto \sqrt{T^4} \propto x^{-2} \text{ and } H = \frac{H(M_\chi)}{x^2}. \tag{1.41}$$

Here $H(M_\chi)$ is a time-independent normalization factor corresponding to the Hubble expansion rate at $T = M_\chi$, serving as a reference (normalized) Hubble parameter. Combining Eq. 1.39 with Eq. 1.41 we get

$$\frac{dY}{dt} = -\frac{M_\chi^3 \langle \sigma v \rangle}{H(M_\chi)} \frac{1}{x^2} \left(Y^2 - Y_{eq}^2 \right). \tag{1.42}$$

This type of equation belongs to the class of Riccati equations, which in general does not have an analytical solution. The numerical solution of Eq. 1.42 is shown in Fig. 1.6

However, it is possible to obtain an analytical solution for Y_∞ in the asymptotic limit of Eq. 1.42. The value of Y_∞ is related to the present-day dark matter relic abundance, corresponding to $\Omega_c \simeq 0.26$. In the case of $x \gg 1$ ($T \ll M_\chi$), we can neglect the Y_{eq} term in Eq. 1.42, because it rapidly approaches zero.

$$\frac{dY}{dx} \simeq -\frac{\lambda Y^2}{x^2}, \tag{1.43}$$

where $\lambda = \frac{M_\chi^3 \langle \sigma v \rangle}{H(M_\chi)}$. The solution of eq.1.43 is

$$Y_\infty \simeq \frac{x_f}{\lambda}, \tag{1.44}$$

where x_f is the freeze-out epoch, typically of order $\simeq 20$ (see Fig. 1.6). Returning back to the original variables

$$n_\infty = T_f^3 Y_\infty = T_f^3 x_f \frac{\left(\frac{8\pi G}{3} g_* \frac{\pi^2}{30} \right)^{1/2} M_\chi^2}{M_\chi^3 \langle \sigma v \rangle} \tag{1.45}$$

$$\langle \sigma v \rangle = T_f^3 x_f \frac{\left(\frac{8\pi G}{3} g_* \frac{\pi^2}{30} \right)^{1/2}}{\rho_0 \Omega_{DM}} \tag{1.46}$$

A crucial point is that the freeze-out temperature T_f differs from the present-day CMB temperature due to entropy conservation in the expanding Universe. For this reason, the temperatures of cosmic neutrinos and CMB photons differ as well. In the early Universe, entropy was distributed across a large range of Standard Model particles, whereas today only photons and neutrinos carry it: $g_{\text{now}} \approx 2 + \frac{7}{8} \cdot 6 \cdot \left(\frac{4}{11}\right)^{4/3} \approx 3.36$. The first term corresponds to the photon contribution; the second term corresponds to the contribution of neutrinos and antineutrinos (three flavors, each with a particle and an antiparticle), with the factor 7/8 arising from Fermi–Dirac statistics. The factor $(4/11)^{4/3}$ accounts for the difference between the neutrino and photon temperatures. Note that $g_*^{\text{freeze-out}} \approx 106.75$.

$$g_*^{\text{freeze-out}}\, T_f^3\, a_f^3 = g^{\text{now}}\, T_0^3\, a_0^3 \tag{1.47}$$

From Eq. 1.46 we obtain

$$\langle \sigma v \rangle = \frac{T_0^3 g^{\text{now}}}{g_*} x_f \frac{\left(\frac{8\pi^3}{90} g_*\right)^{1/2}}{\rho_0 \Omega_{DM} M_{Pl}}, \tag{1.48}$$

here all quantities are expressed in GeV units, and the gravitational constant is written in terms of the Planck mass. Solving this equation we find

$$\langle \sigma v \rangle \approx 1.52 \cdot 10^{-9} \;\; \text{GeV}^{-2}, \tag{1.49}$$

or by converting to CGS units

$$\langle \sigma v \rangle \approx 2 \cdot 10^{-26} \;\; \text{cm}^3\text{s}^{-1}. \tag{1.50}$$

The thermal cross-section of the WIMP is mass-independent. Here, we just presented the standard derivation of the canonical WIMP annihilation cross section. In the literature (e.g. Dodelson and Schmidt, 2020) and throughout this work, we adopt the commonly used reference value of $\langle \sigma v \rangle = 3 \cdot 10^{-26}\,\text{cm}^3\text{s}^{-1}$.

A more detailed and accurate analysis by Steigman et al. (2012) shows that the annihilation cross section may deviate from this canonical value and exhibits a dependence on the WIMP mass, as illustrated in Fig. 1.7.

To complete the derivation of the thermal annihilation cross section, we now discuss the properties of the freeze-out parameter x_f in more detail and provide an estimate of its typical value. By equating the annihilation rate $\langle \sigma v \rangle n_{eq}(x_f)$ and the Hubble rate H. For non-relativistic matter the equilibrium number density follows the Maxwell-Boltzmann distribution:

$$n_{eq}(T) = g \left(\frac{M_\chi T}{2\pi}\right)^{3/2} e^{-M_\chi/T} = g \left(\frac{M_\chi^2}{2\pi x}\right)^{3/2} e^{-x} \tag{1.51}$$

The Hubble rate in the radiation-dominated era

$$H^2 = \frac{8\pi G}{3} \rho_\gamma, \tag{1.52}$$

with the radiation energy density

$$\rho_\gamma = \frac{\pi^2}{30} g_* T^4, \tag{1.53}$$

where g_* is the total number of degrees of freedom

$$g_* = g_{bosons} + \frac{7}{8} g_{fermions} \approx 106.75 \tag{1.54}$$

The factor $\frac{7}{8}$ appears because of the different statistics for bosons and fermions.

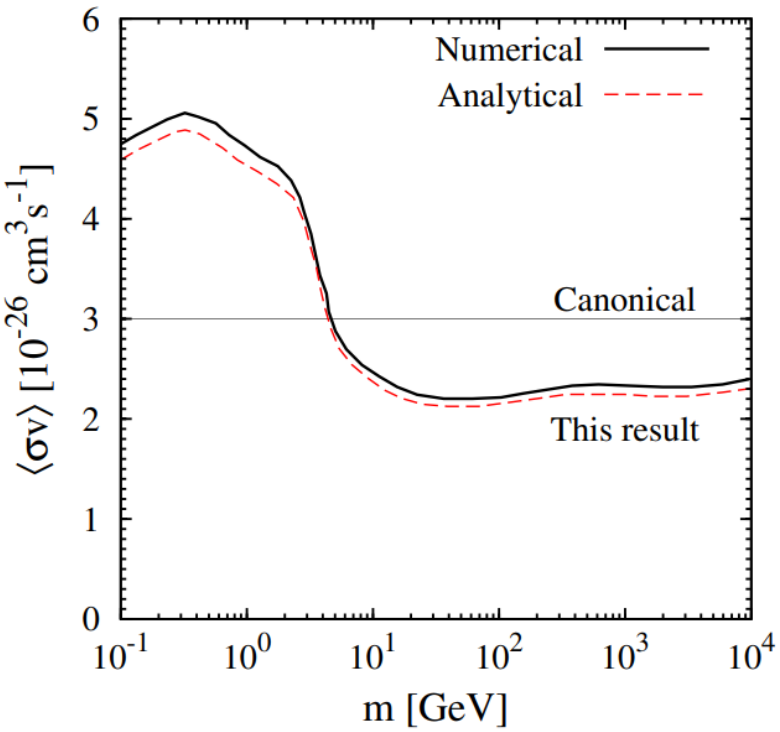

Figure 1.7 The black solid line shows the thermal annihilation cross section as a function of the WIMP mass, while the grey solid line represents the canonical thermal cross section. From Steigman et al. (2012).

For leptons there are three kind of particles e, μ, τ, each with an antiparticle and two spin states. There are also three types of neutrinos with their antiparticles, giving the total $g_{leptons} = 18$. There are also six quark flavors (three colors, two spins, plus antiquarks) $g_{quarks} = 72$. This gives $g_{\mathrm{fermions}} = 90$. The bosonic content comprises eight gluons with two polarizations $g_{gluons} = 16$, the four electroweak gauge bosons W^+, W^-, Z, γ with two polarizations each $g_{\mathrm{EW}} = 8$, and the Higgs doublet $g_{\mathrm{Higgs}} = 4$, giving $g_{\mathrm{bosons}} = 28$.

The Hubble rate is therefore

$$H = \left(\frac{8\pi G}{3} g_* \frac{\pi^2}{30} T^4\right)^{1/2} = \left(\frac{8\pi G}{3} g_* \frac{\pi^2}{30} M_\chi^4\right)^{1/2} x^{-2} \tag{1.55}$$

Equating the Hubble rate from Eq. 1.55 to the annihilation rate from Eq. 1.51 gives

$$\langle \sigma v \rangle g \left(\frac{M_\chi^2}{2\pi x}\right)^{3/2} e^{-x} = \left(\frac{8\pi G}{3} g_* \frac{\pi^2}{30} M_\chi^4\right)^{1/2} x^{-2} \tag{1.56}$$

from which the freeze-out value x_f can be obtained

$$e^{x_f} = x_f^{1/2} \frac{\langle \sigma v \rangle M_\chi M_{Pl}}{8\pi^3/\sqrt{90}} \frac{g}{\sqrt{g_*}} \tag{1.57}$$

Solving numerically this equation gives $x_f \approx 26$. Here the gravitational constant is expressed in terms of the Planck mass as $G = M_{Pl}^{-2}$.

1.4.4 WIMP Detection Experiments

Direct detection experiments search for the scattering of dark matter particles off nucleons or electrons. It is assumed that a large flux of dark matter particles, bound within the halo

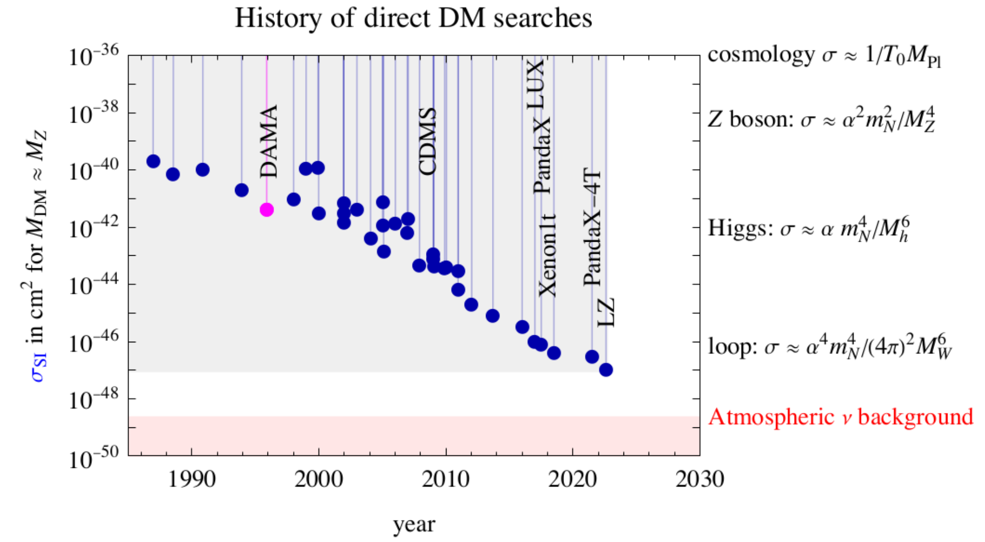

Figure 1.8 Evolution of upper limits from direct detection experiments on the spin-independent dark matter–nucleon scattering cross section, assuming a dark matter mass comparable to that of the Z boson. From Cirelli et al. (2024).

of our Galaxy, passes through the Earth every second. Consequently, dark matter particles may traverse terrestrial detectors and occasionally scatter off nuclei or electrons within the detector material.

A major experimental challenge is the extreme rarity of such events, with expected rates potentially below one event per ton of detector material per year.

Under the assumption of elastic scattering, the highest sensitivity of these experiments typically peaks for WIMP masses around $\sim 50, \mathrm{GeV}$ in the case of nuclear recoils and in the $\sim$ MeV range for electron recoils.. The historical evolution of upper limits on the WIMP–nucleon cross section is shown in Fig. 1.8.

For example, the PandaX-II experiment (Cui et al., 2017), one of the most sensitive direct detection experiments for WIMP masses around 40 GeV, reported an upper limit on the spin-independent WIMP–nucleon cross section of $8.6 \times 10^{-47}\,\mathrm{cm}^2$ at 90% confidence level.

Such experiments place upper limits on the WIMP–nucleon elastic scattering cross section on nuclei at the level of $\sim 10^{-46}$–$10^{-47}, \mathrm{cm}^2$, which is approximately ten–twelve orders of magnitude smaller than the typical thermal annihilation cross section ($\sigma \sim 10^{-35}\,\mathrm{cm}^2$), assuming a WIMP velocity of order $0.1, c$ at the freeze-out epoch. at freeze-out.

If dark matter is composed of WIMPs, its scattering cross section with baryons is expected to be strongly suppressed.

1.5 WIMP Annihilation Signatures

The process of dark matter particle annihilation is described below, leading to the production of secondary Standard Model particles, which are assumed to eventually decay into electrons and positrons. This is discussed in Colafrancesco et al. (2006), Storm et al. (2017), Regis et al. (2021), Egorov (2023) and others.

In this section, we discuss the theoretical framework. First, we outline the main concepts and then present the full derivation in a more rigorous way.

1. Two DM particles annihilate and produce a pair of Standard Model (SM) particles. These SM particles subsequently undergo secondary decays, generating cascades of stable particles.

2. The secondary electrons and positrons, propagating in the presence of the intracluster magnetic field, emit synchrotron radiation.
3. Given the DM distribution within the galaxy cluster, we estimate the number density of WIMPs and the rate of annihilation processes.
4. Electrons and positrons lose energy through various astrophysical processes. These energy losses affect the equilibrium energy spectrum of particles.
5. Using this information, we determine the energy spectrum and number density of the secondary electrons and positrons.
6. By integrating over the cluster volume, we estimate the expected emission from secondary electrons and positrons as a footprint of dark matter annihilation.
7. By comparing the theoretically predicted emission with observational data, we constrain the best-fit WIMP parameters, namely the particle mass and the annihilation cross-section.

1.5.1 Dark Matter Annihilation Channels

We consider the following model: two dark matter particles (χ) annihilate, releasing an amount of energy equal to $2m_\chi c^2$. As a result, a pair of Standard Model (SM) particles (ψ) is produced,

$$\chi + \chi \to \psi + \psi \,. \tag{1.58}$$

The annihilation can proceed through different channels, including quark–antiquark pairs ($b\bar{b}$, $t\bar{t}$, and other quark flavors), leptonic channels ($e^- e^+$, $\mu^- \mu^+$, $\tau^- \tau^+$), electroweak gauge bosons ($W^- W^+$ and ZZ), photons ($\gamma\gamma$), gluons (gg), and Higgs bosons (hh) (Cirelli et al., 2011).

Table 1.1 The masses of Standard Model fundamental particles (from Particle Data Group Workman et al. (2022))

Particle	**Mass [GeV/c^2]**	**Notes**
	Leptons	
Electron (e)	5.11×10^{-4}	Charged lepton
Muon (μ)	0.106	Charged lepton
Tau (τ)	1.78	Charged lepton
	Quarks	
Up (u)	2.2×10^{-3}	Current quark mass
Down (d)	4.7×10^{-3}	Current quark mass
Strange (s)	96×10^{-3}	Quark
Charm (c)	1.27	Quark
Bottom (b)	4.18	Quark
Top (t)	173	Heaviest quark
	Bosons	
W boson (W)	80.4	Weak gauge boson
Z boson (Z)	91.2	Weak gauge boson
Higgs boson (H)	125	Scalar boson

These secondary particles, characterized by the energy distribution dN_i/dE, may subsequently undergo further decays (if they are unstable), giving rise to a particle cascade. Ultimately, an ensemble of stable "granddaughter" particles is produced, described by a specific energy distribution dN_f/dE, which can be obtained from the following expression:

$$\frac{dN_f}{dE} = \sum_i B_i \frac{dN_{i\to f}}{dE} \,. \tag{1.59}$$

Here, B_i denotes the branching ratio of the $i \to f$ decay channel. For more details, see Cirelli et al. (2024, section 6.1). The parameters of leptons, quarks, and bosons are summarized in Table 1.1.

1.5.2 Secondary Electron–Positron Emission

From this ensemble of secondary particles, we focus exclusively on electrons and positrons, since their presence in a magnetic field leads to synchrotron radiation, which can be mainly observed in the radio band.

The synchrotron power emitted per unit frequency by a single electron in the presence of a magnetic field is given by

$$P_\nu(\nu, E, r, z) = \int_0^\pi d\theta \frac{\sin\theta}{2} 2\pi\sqrt{3} r_0 \nu_0 m_e c \sin\theta F\left(\frac{x}{\sin\theta}\right) \tag{1.60}$$

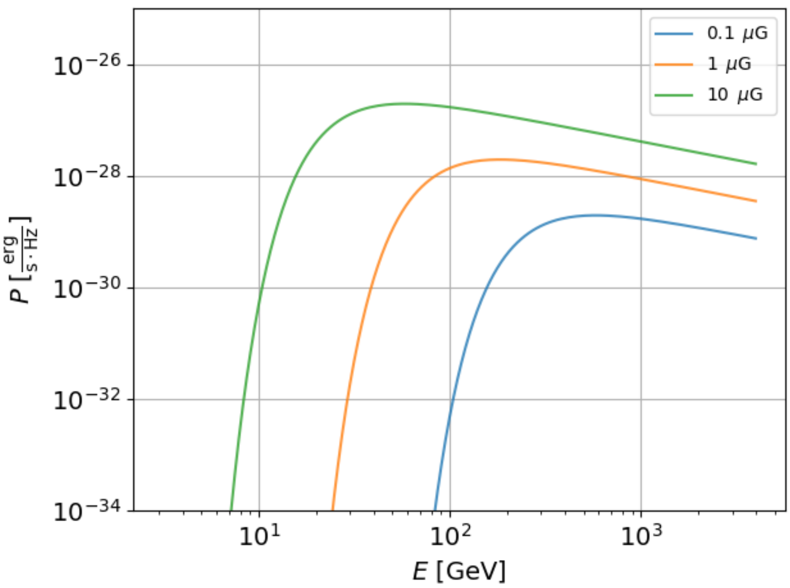

Figure 1.9 Synchrotron emission power of a single electron at 140 MHz as a function of electron energy. The emission depends on the magnetic field.

where $r_0 = e^2/(m_e c^2)$ is the classical electron radius, θ is the pitch angle, and $\nu_0 = eB/(2\pi m_e c)$ is the non-relativistic gyrofrequency. Following notation of Colafrancesco et al. (2006), we define quantities x and $F(x)$ we defined them as

$$x = \frac{2\nu(1+z)}{3\nu_0\gamma^2}\,, \tag{1.61}$$

$$F(x) = x\int_x^\infty d\xi\, K_{5/3}(\xi) \approx 1.25\, x^{1/3} \exp(-x) \left(648 + x^2\right)^{1/12}. \tag{1.62}$$

Here, $K_{5/3}(\xi)$ is the modified Bessel function of the second kind of order 5/3. As shown in Eqs. 1.61–1.62 and in Fig. 1.9, the synchrotron emission produced by a single electron depends on the magnetic field and on its energy expressed in the terms of Lorentz-factor.

The synchrotron power spectrum per frequency per electron can be simplified as

$$P_\nu(\nu, E, r, z) = \sqrt{3}\pi\nu_0 r_0 m_e c \int_0^\pi \sin^2\theta \cdot 1.25 \frac{x^{1/3}}{\sin^{1/3}\theta} exp(-\frac{x}{\sin\theta})[648 + \frac{x^2}{\sin^2\theta}]^{1/12} d\theta$$

Fig. 1.9 shows the single-electron synchrotron emissivity at 140 MHz as a function of electron energy and the magnetic field, the redshift is set to zero.

1.5.3 Dark Matter Distribution and Annihilation Rate

To estimate the total flux as a signature of the WIMP annihilation, we must determine the particle number density and the corresponding rate of this process.

Let σ denote the annihilation cross section and n_χ the total number density of DM particles. Then, the mean free path is given by

$$\lambda = \frac{1}{\frac{1}{2}n\sigma}, \tag{1.63}$$

the coefficient 1/2 in front of the number density accounts for the presence of both DM and anti-DM particles species. The typical interaction time t can be written as

$$t = \frac{\lambda}{v} = \frac{1}{\frac{1}{2}n_\chi \sigma v}. \tag{1.64}$$

We now average over the dark matter particle velocities to obtain the thermally averaged annihilation cross section $\langle \sigma v \rangle$, as discussed in Section 1.4.3. From this point onward, the annihilation cross section is understood to denote the thermally averaged quantity $\langle \sigma v \rangle$.

In a volume V, there are $N_\chi = n_\chi V$ dark matter particles. In the annihilation process, each pair of interacting particle releases an energy of $2M_\chi c^2$. The total energy production rate is therefore given by

$$Q = \frac{N_\chi}{2}\frac{1}{t}2M_\chi c^2 = \frac{n_\chi V M_\chi c^2}{t} = \frac{n_\chi^2 M_\chi c^2 \sigma v V}{2} \tag{1.65}$$

Where we also take into account the relation between density and number density

$$n_\chi = \frac{\rho_\chi}{M_\chi}. \tag{1.66}$$

The dark matter density profile can be described by the Navarro–Frenk–White (NFW) profile (Navarro et al., 1996), or by other commonly used parameterizations (For more details, see Section 1.B). The total energy production per unit time per unit volume is

$$Q = \frac{\rho_\chi^2 c^2}{2M_\chi}\langle \sigma v \rangle \tag{1.67}$$

Here, $Q = Q(\langle \sigma v \rangle, M_\chi, R)$ is the *source term*, which depends on the velocity-averaged annihilation cross section (hereafter simply named as the cross section), the dark matter particle mass, and the dark matter density profile as a function of the distance R from the cluster center. Equation 1.67 is hereafter referred to as the *source term equation*.

The energy injected by the source term Q is distributed among an ensemble of secondary stable particles according to an energy spectrum.

$$Q(E, r) = \sum_f Q_f(E, r) \tag{1.68}$$

Where

$$Q_f(E, r) = \int_E^{M_\chi c^2} E' \frac{dn_f}{dE}(E', r) dE' \tag{1.69}$$

Where dn_f/dE is the energy spectrum of the f-th species of injected particles. Hereafter, we will focus only on electrons and positrons and will rename the source term corresponding to electrons $Q_e(E, r)$ as $Q(E, r)$.

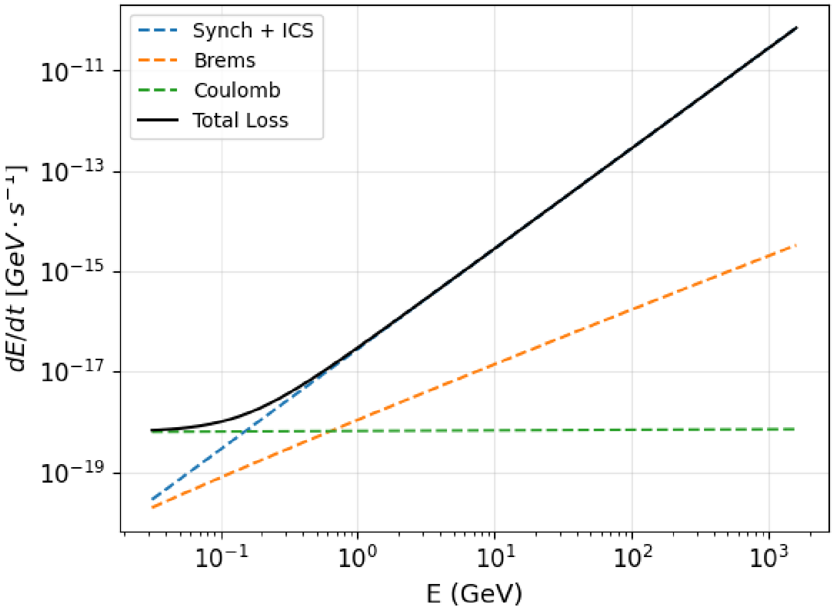

Figure 1.10 The energy-loss term is shown for a magnetic field strength of $B = 1\,\mu$G and an electron number density of $n_e = 10^{-3}\,\text{cm}^{-3}$, which are typical values for galaxy clusters. The total energy-loss rate is represented by the solid black line, while the combined synchrotron and inverse Compton contributions are shown by the blue dashed line. For electron energies greater than a few tenths of a GeV, Coulomb and bremsstrahlung losses become negligible.

1.5.4 Loss Term

To understand the energy spectrum of electron in thermal equilibrium, it is necessary to take into account the rate of electron energy losses. We consider four primary energy loss mechanisms: synchrotron radiation, inverse Compton scattering, bremsstrahlung (or free-free) emission, and ionization (or Coulomb) losses.

$$b_{loss}(E, B, n_e) = b_{\text{Synch}}(E, B) + b_{\text{ICS}}(E) + b_{\text{Brem}}(E, n_e) + b_{\text{Coul}}(E, n_e) \tag{1.70}$$

According to Sarkis and Beck (2025), and in agreement with Egorov (2022), the coefficients of the energy-loss terms can be written as

$$\begin{cases} b_{\text{Synch}} = 2.5 \cdot 10^{-18} \left(\dfrac{B}{1\mu\text{G}}\right)^2 \left(\dfrac{E}{1\text{GeV}}\right)^2 \\ b_{\text{ICS}} = 0.26 \cdot 10^{-16} \left(\dfrac{E}{1\text{GeV}}\right)^2 \\ b_{\text{Brem}} = 7.1 \cdot 10^{-20} \gamma \left(\dfrac{n_e}{1\,\text{cm}^{-3}}\right) (\ln\gamma + 0.36) \\ b_{\text{Coul}} = 7.6 \cdot 10^{-18} \left(\dfrac{n_e}{1\,\text{cm}^{-3}}\right) \left(\ln\dfrac{\gamma}{n_e} + 73\right) \end{cases}$$

Here, γ and E denotes the Lorentz factor and the energy (in GeV) of the particle, B is the magnetic-field strength in μG, and n_e is the electron number density measured in cm^{-3}. The total energy-loss term is given in units of $\text{GeV}\,\text{s}^{-1}$.

For high-energy particles ($E > 1$ GeV), the dominant energy-loss mechanisms are synchrotron radiation and inverse Compton scattering, both of which scale as the square of the particle energy. An example of the total energy-loss term is presented in Fig. 1.10.

1.5.5 Energy Spectrum of Secondary Electrons and Positrons

In Section 1.5.2 we showed the synchrotron power emission by a single electron. The next step is understanding the total number-density of electrons with certain energy E. From which we will be able to estimate the expected total flux from a galaxy cluster. The evolution of the electron power spectrum is described by the diffusion equation

$$\frac{\partial}{\partial t}\frac{dn_e}{dE}(E,r) = \nabla\left[D(E,r)\nabla\frac{dn_e}{dE}\right] + \frac{\partial}{\partial E}\left[b_{loss}(E,r)\frac{dn_e}{dE}\right] + Q(E,r) \tag{1.71}$$

where dn_e/dE is the electron equilibrium spectrum, $Q(E,r)$ the source (see Eq 1.67 and Eq. 1.69), $D(E,r)$ is the spatial diffusion coefficient, $b_{loss}(E,r)$ is the energy loss term described in Eq. 1.70.

As a result, the energy loss processes govern the evolution of the electron distribution, allowing the diffusion term in the diffusion equation to be neglected. Let us consider the stationary case

$$\frac{\partial}{\partial t}\frac{dn_e}{dE} = 0; D = 0 \tag{1.72}$$

The diffusion equation becomes

$$0 = \frac{\partial}{\partial E}\left[b_{loss}(E,r,z)\frac{dn_e}{dE}\right] + Q(E,r) \tag{1.73}$$

from which we derive the equilibrium electron spectrum

$$\frac{dn_e}{dE}(E,r) = -\frac{1}{b_{loss}(E,r)}\int_E^{M_\chi c^2} Q(E',r)dE' \tag{1.74}$$

The upper integration limit corresponds to the maximum energy at which the particles can be injected into the system, which is the DM particle mass $M_\chi c^2$. The lower limit corresponds to the fact that only electrons injected with energies $E' \geq E$ can contribute to the equilibrium spectrum at energy E after energy losses.

1.5.6 Synchrotron Emission from Dark Matter Annihilation

Now that we know both the equilibrium electron energy spectrum given by Eq. 1.74 and the synchrotron emissivity of a single electron given by Eq. 1.60, we can combine them to obtain the total synchrotron emissivity:

$$J_\nu(r,z) = 2\int_{m_e c^2}^{M_\chi c^2} P_\nu(E,r,z)\,\frac{dn_e}{dE}(E,r)\,dE\,. \tag{1.75}$$

The factor of 2 accounts for contributions from both electrons and positrons. Evaluating this integral yields the synchrotron emissivity per unit volume as a function of radius within the galaxy cluster. Assuming spherical symmetry of the cluster, we estimate the flux per unit projected area (the surface brightness).

$$I_\nu(r) = \frac{1}{4\pi}\int_r^\infty J_\nu(r')\frac{r'dr'}{\sqrt{r'^2 - r^2}} \tag{1.76}$$

In Sections 1.5.1–1.5.6, we obtained estimates of the expected emission from dark matter particle annihilation, parameterized in terms of WIMP properties such as mass and annihilation cross-section. By comparing observations of real astrophysical sources with the theoretical predictions presented above, one can derive constraints or upper limits on the mass and cross-section of WIMPs.

1.6 Galaxy Clusters as Laboratories for Probing Dark Matter

A useful quantity for estimating the annihilation signal from DM particles is the so-called J-factor. The expected signal from secondary particles can be separated into two components:

$$I = \phi \times J, \tag{1.77}$$

where ϕ depends on the WIMP properties, such as particle mass, annihilation cross-section, and annihilation channel, while the second term J, so-called J-factor, contains the dependence on the astrophysical properties of the source:

$$J = \int \rho_{\mathrm{DM}}^2 \, dl \, d\Omega \approx \frac{\rho_s^2 R_s^3}{r^2}, \tag{1.78}$$

here, ρ_s denotes the characteristic dark matter density and R_s the scale radius of the halo. The index s refers to the parameters of the NFW profile (see Section 1.B), while r is the distance from the source.

The larger the J-factor, the higher the expected flux from dark matter annihilation. Below, we compare several characteristic classes of astrophysical objects, including dwarf galaxies, galaxies, and galaxy clusters. The estimated J-factors are summarized in Table 1.2.

- **Dark matter in dwarf galaxies.** Dwarf galaxies were analyzed by Regis et al. (2015). The main advantage of these objects is the absence, or very low level, of intrinsic radio emission, which makes them particularly suitable targets for indirect dark matter searches. Using observations of the Large Magellanic Cloud, Regis et al. (2021) derived a lower limit on the WIMP mass of approximately 500 GeV.

- **Dark matter searches in galaxies.** Among galaxies, two of the most promising candidates for dark matter searches are the Andromeda galaxy (M31) and the Milky Way (Egorov, 2022). According to Table 1.2, M31 possesses one of the highest J-factors among nearby astrophysical sources. However, a significant disadvantage is the presence of strong astrophysical background emission. As a result, one has to model and separate the conventional astrophysical emission from a possible dark matter contribution. A detailed analysis of dark matter signatures in M31 was performed by Egorov (2023), where the upper-limit of WIMPs mass was set as an order of 100 GeV.

- **Dark matter in galaxy clusters.** Galaxy clusters contain enormous amounts of dark matter, contributing up to 80–90% of the total cluster mass (see, e.g., Vikhlinin et al. (2006)). Although their characteristic J-factors are typically lower than those of dwarf galaxies or nearby galaxies, galaxy clusters may experience an additional enhancement of the annihilation signal due to dark matter substructures concentrated toward the cluster. This effects is referred to as the *substructure boost factor*. Another important advantage is that the magnetic fields in galaxy clusters can be independently estimated through Faraday rotation measurements (see Section 1.A).

  On the other hand, galaxy clusters contain diffuse non-thermal emission of astrophysical origin. It is necessary to separate this component from the potential dark matter-induced emission.

  The theoretical foundations for searches of WIMP annihilation signatures in galaxy clusters were established by Colafrancesco et al. (2006).

Table 1.2 Characteristic properties of astrophysical objects commonly used in indirect dark matter searches. J-factor estimated by Eq. 1.78

Object	Type	ρ_s [GeV cm^{-3}]	R_s [kpc]	M [$M_\odot$]	Distance [Mpc]	J-factor [GeV^2 cm^{-5}]
Fornax	Dwarf galaxy	0.15	0.67	$5 \cdot 10^7$	0.15	$9 \cdot 10^{14}$
Carina	Dwarf galaxy	0.4	0.24	$6 \cdot 10^6$	0.076	10^{15}
M31	Galaxy	0.12	10.4	10^{12}	0.78	$8 \cdot 10^{16}$
Coma	Galaxy cluster	0.01	290	$1.4 \cdot 10^{15}$	101	$7 \cdot 10^{14}$
Abell 2199	Galaxy cluster	0.02	180	$7.6 \cdot 10^{14}$	128	$4 \cdot 10^{14}$

1.7 Overview of Radio Interferometry

1.7.1 Radio Interferometry for Searching DM Signatures

Fig. 1.11 shows the expected radio emission from dark matter annihilation as a function of the distance from the center of the Coma Cluster for different observing frequencies ranging from 10 MHz to 100 GHz. We find that the expected flux is higher at lower frequencies.

Ground-based observations are fundamentally limited at the low-frequency end by the Earth's ionosphere, whose plasma cut-off reflects or absorbs incoming radiation below ~ 10 MHz. Above this limit, the decametre-to-metre range up to ~ 1 GHz remains observable, and this window is of greatest interest here: as shown in Fig. 1.11, the expected DM signal rises towards lower frequencies, with the sub-GHz range probing the lightest DM particle masses, where the predicted flux is largest.

Several current generation interferometers provide access to this band: MWA (Lonsdale et al., 2009, Murchinson Widefield Array) covers the 70 to 300 MHz range, uGMRT (Gupta et al., 2017, updated Giant Metrewave Radio Telescope) spans from 50 to 1500 MHz across its bands, LWA (Ellingson et al., 2009, Long Wavelength Array) and NenuFAR (Zarka et al., 2012, New extension in Nançay upgrading LOFAR) access the lowest frequencies (10–85 MHz), and VLA (Perley et al., 2011, Very Large Array) can access the 58-84 and 230-470 MHz ranges with the 4- and P-bands, respectively. In the near future, SKA-Low (Dewdney et al., 2009, Square Kilometer Array) will be the most sensitive telescope mapping the 50–350 MHz frequency range. Among these facilities, LOFAR (van Haarlem et al., 2013, Low Frequency Array) operates in the 10–240 MHz frequency range, provides one of the highest sensitivities at around 150 MHz, and offers archival observations with integration times of tens of hours for targets of interest.

1.7.2 Introduction to Radio Interferometry

The derivations presented in this section are based on *Synthesis Imaging in Radio Astronomy II* by Taylor et al. (1999).

Let us consider a single antenna whose position in space is specified by the vector $\vec{r}$. We also assume the presence of a distant point source located at position $\vec{R}$, such that $R \gg r$. This source produces an electric field $\vec{E}(\vec{R}, t)$, which propagates toward the observer in the form of electromagnetic waves.

Due to the linearity of Maxwell's equations, the electric field $\vec{E}$ can be decomposed into a superposition of monochromatic components $\vec{E}_\nu$, and any time-dependent signal may be expressed into a Fourier series, which likewise preserves linearity. Consequently, we consider the electric field component $\vec{E}_\nu(\vec{R})$ to be time-independent and quasi-monochromatic.

Under these assumptions, the electric field measured by the antenna can be written as

$$E_\nu(\vec{r}) = \int\int\int P_\nu(\vec{R}, \vec{r}) E_\nu(\vec{R}) dxdydz \tag{1.79}$$

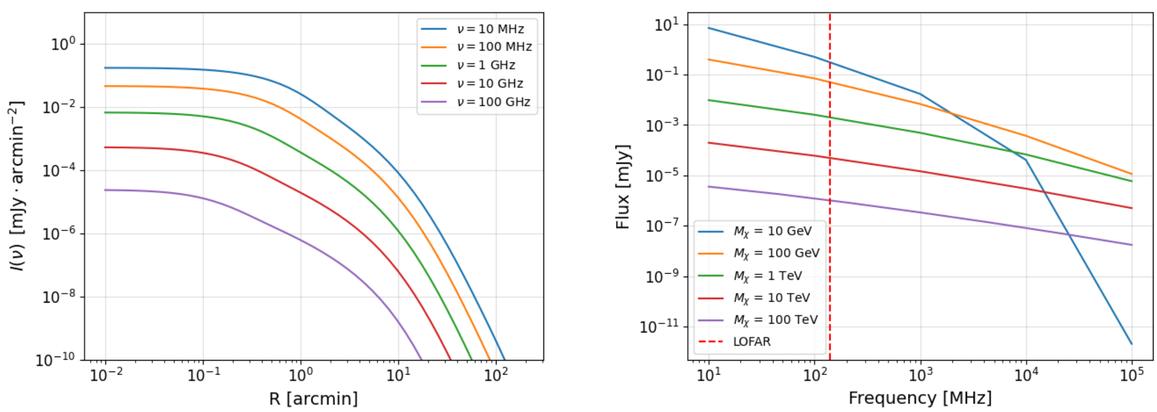

Figure 1.11 Left panel shows the expected synchrotron emission from dark matter annihilation calculated for different observing frequencies from the Coma Cluster. The input parameters are a WIMP mass of 100 GeV, an annihilation cross-section of 10^{-26} cm^3 s^{-1}, and the $b\bar{b}$ annihilation channel. The simulation was performed using the *DarkMatters* code; see Section 2.4 for details.
The right panel shows the total expected flux from the Coma Cluster at different observing frequencies. The vertical line indicates the central observing frequency of LOFAR. The simulations were performed for WIMPs with a fixed $b\bar{b}$ annihilation channel and an annihilation cross-section of 10^{-26} cm^3 s^{-1}, for different masses ranging from 10 GeV to 100 TeV.

where the *propagator* $P_\nu(\vec{R}, \vec{r})$, describes the contribution of the electric field at the source position $\vec{R}$ to the electric field at the observation point $\vec{r}$. Treating the electric field from each source element as a spherical wave, the propagator takes the form

$$E_\nu(\vec{r}) = \int E_\nu(\vec{R}) \frac{1}{R} e^{-2\pi\nu i|\vec{R}-\vec{r}|/c} dS \tag{1.80}$$

where dS is an element of the spherical surface of radius R enclosing the source. This electric field can be measured by a single antenna.

In practice, however, interferometers are commonly used (see Fig. 1.12) The simplest interferometer consists of two antennas, measuring $E_\nu(\vec{r}_1)$ and $E_\nu(\vec{r}_2)$ respectively. The correlation of their signal at frequency ν is then given by

$$V_\nu(\vec{r}_1, \vec{r}_2) = \langle E_\nu(\vec{r}_1) E^*_\nu(\vec{r}_2) \rangle \tag{1.81}$$

The asterisk denotes complex conjugation and $\langle \cdot \rangle$ the time ensemble average. Substituting Eq. 1.80 for each field in Eq. 1.81 gives

$$V_\nu(\vec{r}_1, \vec{r}_2) = \langle \int \int E_\nu(\vec{R}_1) E^*_\nu(\vec{R}_2) e^{-2\pi i\nu|\vec{R}_1-\vec{r}_1|/c} e^{2\pi i\nu|\vec{R}_2-\vec{r}_2|/c} \rangle \frac{dS_1 dS_2}{R_1 R_2} \tag{1.82}$$

Under the far-field approximation ($R \gg r$), we assume $R_1 \simeq R_2 \simeq R$ and $R \gg r_1, r_2$. In this limit, the wavefront can be approximated as plane waves. Therefore, the distances can be expanded as

$$|\vec{R}_1 - \vec{r}_1| - |\vec{R}_2 - \vec{r}_2| \simeq \hat{s} \cdot (\vec{r}_1 - \vec{r}_2), \tag{1.83}$$

where $\hat{s}$ is the unit vector pointing in the direction of the source. Thus we obtain

$$V_\nu(\vec{r}_1, \vec{r}_2) = \int \langle |E_\nu(\vec{R})|^2 \rangle e^{-2\pi i\nu\hat{s}\cdot(\vec{r}_1-\vec{r}_2)/c} d\Omega \tag{1.84}$$

where $d\Omega$ is the solid-angle element. We identify $|E_\nu(\vec{R})|^2$ with the source intensity $I(\hat{s})$.

We choose a reference plane perpendicular to the direction toward the source, where the vector u points to the east and the vector v points to the north. Together, they define

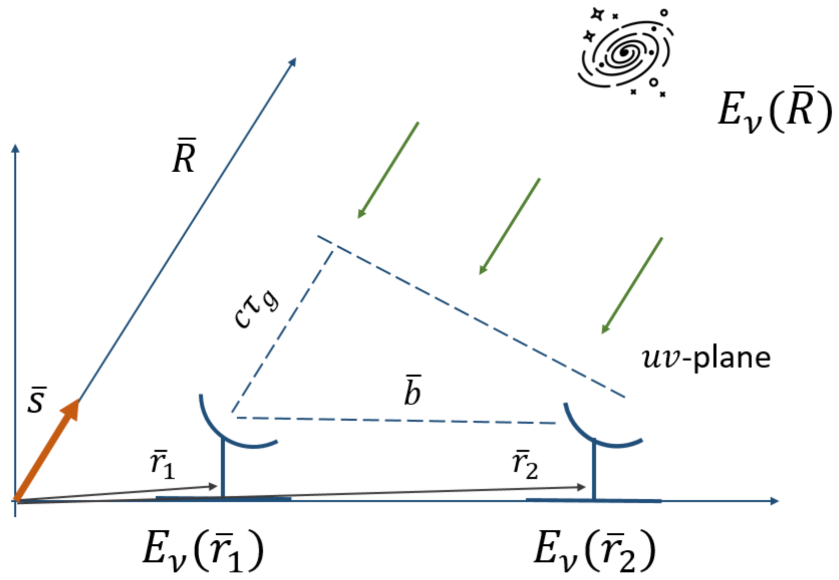

Figure 1.12 A basic interferometer consisting of two antennas located at positions $\vec{r}_1$ and $\vec{r}_2$, receiving radiation from a distant monochromatic source. Using the propagator function, the electric field at each antenna can be calculated, allowing the correlation of the received signals to be determined. The figure indicates the position in the uv-plane, the baseline $\vec{b} = \vec{r}_2 - \vec{r}_1$, the geometric delay ct_g, and the unit vector $\hat{s}$ pointing toward the source.

the *uv-plane*. In this plane, the baseline vector can be written as $\vec{r}2 - \vec{r}1 = (u, v, w), \lambda$, where λ is the observing wavelength, and the source direction is given by the unit vector $\hat{s} = (l, m, \sqrt{1 - l^2 - m^2})$. This plane is tangent to the celestial sphere, and l and m are called direction cosines, with $l = \sin\theta_x$ and $m = \sin\theta_y$ (where θ_x and θ_y are the sky coordinates). For a coplanar array ($w = 0$), this gives the van Cittert–Zernike relation:

$$V_\nu(u, v, \omega = 0) = \int\int I_\nu(l, m) \frac{e^{-2\pi i(ul+vm)}}{\sqrt{1 - l^2 - m^2}} dldm. \quad (1.85)$$

This quantity V_ν is called visibility. Visibilities are complex-valued quantities and can be written as $V_\nu = Ae^{-i\phi}$, where A is the amplitude and ϕ is the phase (as also done for antenna gains later in Section 1.7.3).

With the flat-sky approximation ($\theta \ll 1$, so $\sqrt{1 - l^2 - m^2} \simeq 1$), which holds for a small field of view, Eq. 1.85 reduces to the two-dimensional Fourier transform of the sky brightness distribution I_ν.

Moreover, each pair of antennas measures a single point in the uv-plane, but contributes two conjugate visibilities: one at coordinates (u, v) and its Hermitian counterpart at $(-u, -v)$, reflecting the relation $V_\nu(-u, -v) = V_\nu^*(u, v)$ (see also the central panel of Fig. 1.13).

The interferometer elements have different sensitivity in different directions. This angular response is encoded in the *primary beam* $A_\nu(l, m)$

$$V_\nu(u, v) = \int\int A_\nu(l, m) I_\nu(l, m) e^{-2\pi i(ul+vm)} dldm \quad (1.86)$$

In practice, the spatial coherence function V is sampled through discrete coverage of the uv-plane. This sampling can be described by a *sampling function* or *window function* $S(u, v)$, which may be written as

$$S(u, v) = \begin{cases} 1, & \text{if data were taken at this } uv\text{-point}, \\ 0, & \text{if not.} \end{cases} \quad (1.87)$$

As a result of sampling we can measure only

$$I_\nu^D(l,m) = \int\int V_\nu(u,v)S(u,v)e^{2\pi i(ul+vm)}dudv \tag{1.88}$$

$I_\nu^D(l,m)$ is called the dirty image. The dirty image arises because the uv-coverage is incomplete and discrete. In other words, the expression can be written as a convolution:

$$I_\nu^D = I_\nu * B_\nu \tag{1.89}$$

Where $B_\nu(l,m)$ is called *dirty beam* or *point spread function* (PSF) and

$$B_\nu(l,m) = \int\int S(u,v)e^{2\pi i(ul+vm)}dudv \tag{1.90}$$

Only if the sampling region $S(u,v)$ covers the entire plane would PSF $B_\nu(l,m)$ become a delta function and $I^D = I_\nu$ exactly.

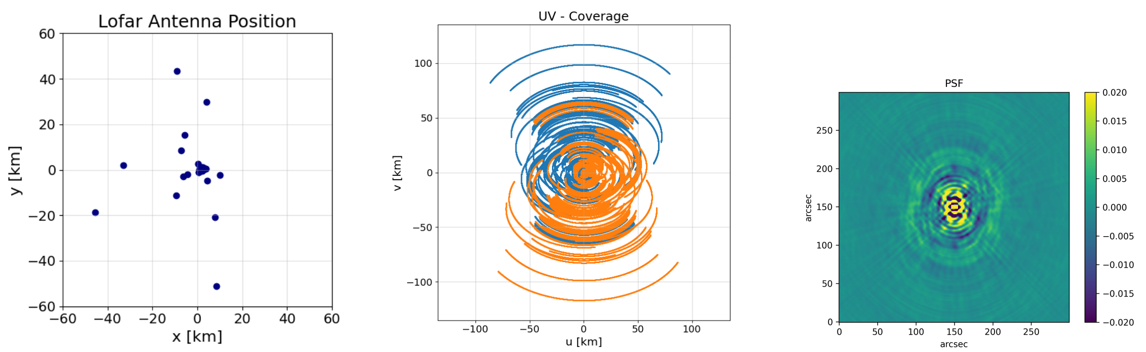

Figure 1.13 The left panel shows the LOFAR HBA station positions. The central panel shows the corresponding uv-coverage, while the right panel shows the resulting PSF.

1.7.3 Data Calibration

A two-element interferometer measures the correlation of the signals received by a pair of antennas i and j along a given baseline projected onto the uv-plane. In the absence of instrumental and propagation effects, this equals the true visibility V_{ij}^T, which is essentially the Fourier transform of the sky brightness (Eq. 1.86). In real observational scenarios, the true sky signal is corrupted by instrumental and propagation effects, which lead to the observed visibilities V_{ij}^O. The purpose of calibration is to model and remove these effects in order to recover V_{ij}^T. The two quantities are related by the radio interferometry measurement equation (Hamaker et al., 1996, RIME):

$$V_{ij}^O = G_{ij}(\nu,t)V_{ij}^T + \varepsilon_{ij}(\nu,t) + \eta_{ij}(\nu,t), \tag{1.91}$$

where G_{ij} is the baseline-based complex gain (also known as a Jones matrix), ε_{ij} is a baseline-based complex offset, and η_{ij} is stochastic complex noise. Most of the corrupting effects are antenna-based, which gives

$$G_{ij}(\nu,t) = G_i(\nu,t)G_j^*(\nu,t) = a_i(\nu,t)a_j(\nu,t)e^{i(\phi_i(\nu,t)-\phi_j(\nu,t))}, \tag{1.92}$$

where $a_j(\nu,t)$ and $\phi_j(\nu,t)$ correspond to the amplitude and phase of the complex gain of each antenna.

For an array of N antennas, there are $N(N-1)/2$ baseline equations but only N antenna gains to determine. The system is therefore overdetermined and can be solved through calibration by estimating the amplitude and phase of the gain for each antenna in the array. All determined gains ($G_i(\nu, t)$ depend on both frequency and time; however, in many cases the time and frequency variations can be treated independently, allowing them to be solved separately.

When visibilities are strongly corrupted, for example by radio-frequency interference (RFI) or malfunctioning antennas, they are excluded from the analysis (*flagged*). In many cases, corrupted data are identified before calibration, for example due to RFI in specific frequency channels. Additional corrupted data can also be identified during calibration by checking the gains. At low frequencies, ionospheric effects can cause fast phase changes in the visibilities, which makes it easier to detect problematic data.

1.7.4 Image Cleaning

An interferometric array yields samples of complex visibilities (see Eq. 1.85 and Eq. 1.88), from which the sky brightness distribution, namely an image, can be recovered through a two-dimensional Fourier transform. However, because the dirty beam exhibits sidelobes that degrade the image quality, deconvolution techniques are required to remove these sidelobes and produce higher-quality images. Among these techniques, the *CLEAN* family of algorithms is the most commonly used approach for recovering I_ν from I_ν^D.

For example, the Högbom (1974) *CLEAN* algorithm solves the convolution equation by modeling the sky brightness distribution as a superposition of point sources (i.e. delta functions).

The main steps of the Högbom 1974 CLEAN algorithm are illustrated in Fig.1.14 and are as follows:

1. Identify the location of the strongest peak in the *dirty image* **(b)**, usually determined from the absolute value of the image intensity.

2. Subtract a fraction of this peak, scaled by a loop gain (or damping factor) **(c)**, convolved with the *dirty beam*, from the *dirty image* **(d)**.

3. Record the position and amplitude of the subtracted peak in a list of CLEAN components, which eventually form the *source model* **(c)**.

4. Repeat the previous three steps iteratively until a stopping criterion is reached, such as a predefined number of iterations or until the brightest peak of the residual *dirty image* falls below a certain threshold level **(e)**. The remaining image is referred to as the *residual image* **(f)**. In an ideal case, where all the sources have been cleaned correctly, residual image should be just thermal noise (which is the lowest brightness achievable in a residual image).

5. Convolve the final *source model* **(g)** with the *clean beam*, usually obtained from a gaussian fitted to the main lobe of the dirty beam, and add to the *residual image* **(f)**, to obtain the so-called restored (or *deconvolved*) image **(i)**.

Several extensions of the original Högbom CLEAN algorithm have been proposed, including the Clark CLEAN (Clark, 1980) and Cotton–Schwab CLEAN (Schwab, 1984) algorithms. These methods improve the computational efficiency of the deconvolution by partially operating in visibility space rather than entirely in the image plane. In particular, the Cotton–Schwab algorithm iteratively subtracts the source model directly from the visibilities and recomputes the residual image, significantly reducing the computational cost and improving the accuracy

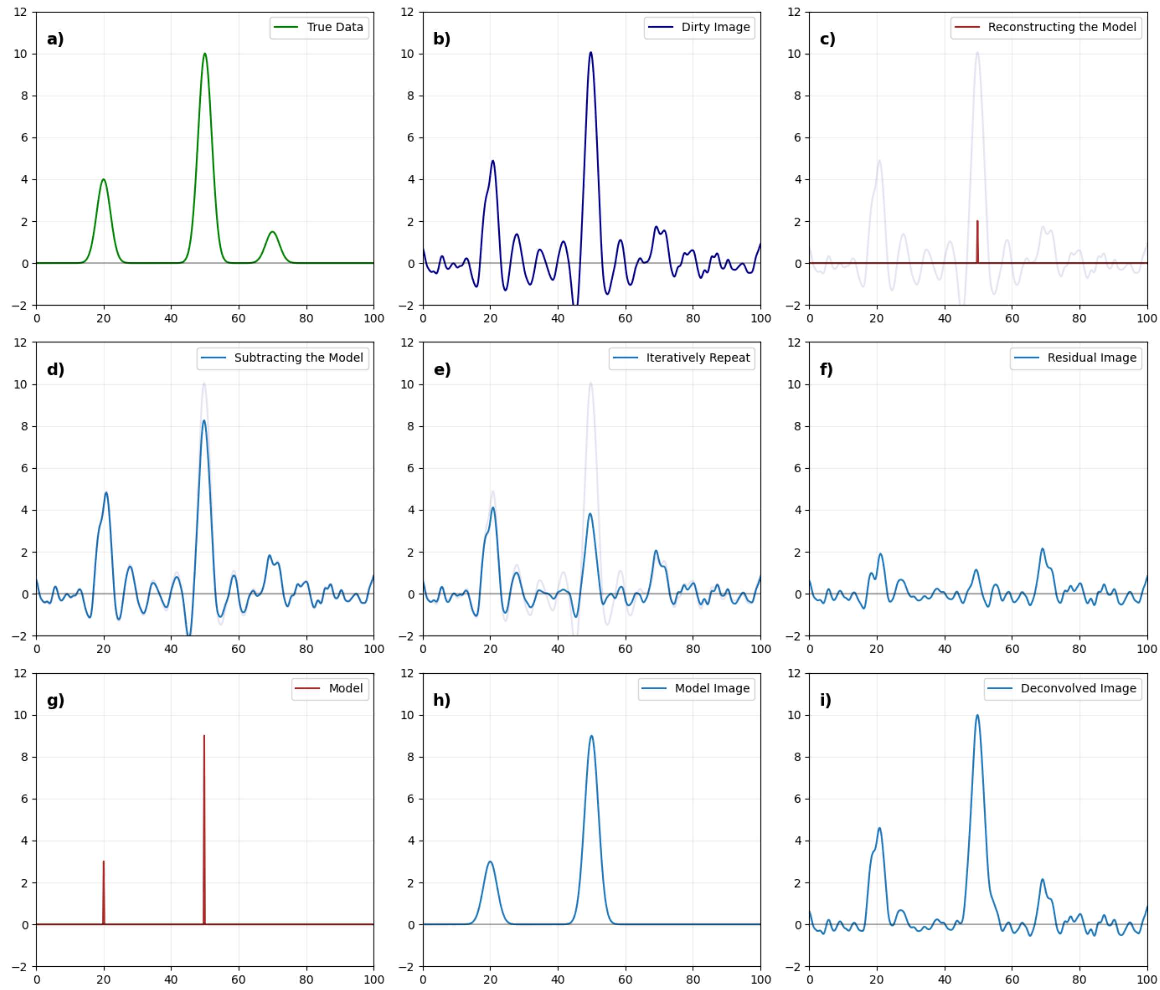

Figure 1.14 The figure illustrates the Högbom 1974 CLEAN algorithm. Panel **(a)** shows the true signal consisting of three sources: a strong, an intermediate, and a weak source. Panels **(b–f)** demonstrate the deconvolution procedure. The CLEAN model shown in panel **(g)** and the corresponding model image in panel **(h)** successfully recover the strong and intermediate sources; however, the weak source remains undetected. Finally, by adding the residual image from panel **(f)**, the final deconvolved image shown in panel **(i)** is obtained. This final image can subsequently be used for measurements of the physical properties of the observed sources and diffuse emission.

of the reconstruction. This approach forms the basis of most modern CLEAN implementations and can naturally account for non-coplanar baselines (the w-term).

A further limitation of the original CLEAN algorithm is its assumption that the sky brightness distribution can be represented as a collection of point sources. While appropriate for compact emission, this approximation performs poorly for extended structures and often requires a large number of CLEAN components. To address this issue, *multi-scale* deconvolution algorithms have been developed, in which the sky brightness is represented as a combination of components with different spatial scales. Common choices include Gaussian basis functions, whose Fourier transforms are analytically known (Cornwell, 2008; Greisen et al., 2009; Offringa and Smirnov, 2017).

1.8 The Low Frequency Array

The Low-Frequency Array (van Haarlem et al., 2013, LOFAR) is a radio interferometer located primarily in the Netherlands, with additional stations distributed across Europe. The central part of the array is shown in Fig. 1.15.

Figure 1.15 The central part of LOFAR. From van Haarlem et al. (2013)

Each LOFAR station is made up of two types of receivers: the Low-Band Antenna (LBA), sensitive to the $10 - 90$ MHz frequency range, and the High-Band Antenna (HBA), sensitive to the $110 - 240$ MHz range. The size and distribution of HBA and LBA within a station change with the distance from the center of the array, such that LOFAR stations are classified into three types, as shown in Fig. 1.16:

- Core stations: 24 LBA and 48 HBA stations located within a maximum distance of 2 km from the array center. In LOFAR, the HBA dipoles are the fundamental receiving elements. These dipoles are grouped into tiles arranged in a 4×4 grid. A collection of tiles forms a single HBA station (24 tiles for core stations, 48 for remote stations, and 96 for international stations).

  Each HBA station in the core is split into two sub-stations, HBA0 and HBA1, each consisting of 24 tiles (see Fig. 1.15). These sub-stations can operate either jointly as a single station or independently as separate stations. Operating them independently increases the number of baselines, thereby improving the *uv*-coverage.

- Remote stations: 14 stations, each equipped with 96 LBA and 48 HBA tiles, are distributed across the Netherlands, providing a maximum baseline of 120 km. An inner observing mode can be used, in which only the inner 24 HBA tiles are activated to match the configuration of the core stations.

- International stations: 14 stations, each with 96 LBA and HBA **tiles**, are distributed across Europe, extending the maximum baseline to 2000 km, enabling very long baseline interferometry (VLBI) with the same instrument.

LOFAR is not a typical interferometer with dishes that can point and track a source. The antennas within a LOFAR station are fixed and do not physically move. Pointing is instead performed via beamforming (Thompson et al., 2017, Chapter Antennas and Arrays): the signal from each antenna is time-delayed before summing, so that waves from the desired direction add coherently while those from other directions are suppressed. By adjusting these delays, the station beam across the sky can be electronically steered (van Haarlem et al., 2013).

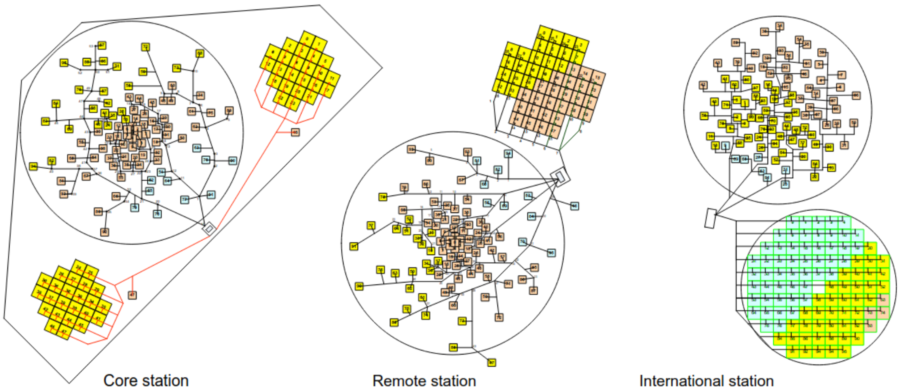

Figure 1.16 The core, remote, and international LOFAR stations layout. Layout is not drawn in scale. The HBA tiles are shown as small squares, while the LBA dipoles are indicated by large circles. Adapted from van Haarlem et al. (2013)

1.8.1 UV-Coverage

The image quality dependents on how well the uv-plane is sampled (for e.g. central panel of Fig. 1.13). A poorly sampled uv-plane can result in strong side-lobes in the synthesized beam (see e.g. right panel of Fig. 1.13) that limiting the overall dynamic range of an image. Moreover, since an interferometer samples discrete points in the uv-plane, the resulting incomplete uv-coverage causes a loss of information of the angular scales that are not sampled. This limitation is particularly important when imaging extended sources.

1.8.2 Angular Resolution

The ability to identify and characterize structures of different angular sizes depends on the angular resolution of an interferometric array.

$$\theta_{res} = \alpha \frac{\lambda}{b_{\max}} \tag{1.93}$$

Where λ is the observing wavelength, b_{max} is the longest baselength up to 3.5 km for core stations and 120 km for remote stations. α is a parameter depends on the array configuration and the imaging weighting scheme (natural, uniform and others). In practice, the resolution also depends on the position of the source in the sky relative to the array zenith: the farther from the zenith the target source is, the more the baselines are foreshortened in projection along the source–zenith direction. This compresses the uv-coverage along that axis, resulting in an elongated, elliptical synthesized beam.

1.8.3 Sensitivity

The sensitivity of the telescope observations can be expressed by using the *system equivalent flux density* (SEFD), defined as the flux density of a hypothetical source that produces the same power to the receiver as the system noise itself. Figure 1.17 shows the SEFD as a function of frequency for the LOFAR core and remote HBA stations.

An increase in the integration time, bandwidth, and number of antennas participating in the observations improves the signal-to-noise ratio. The corresponding system sensitivity can be estimated using Eq. 1.94.

$$\Delta S = \frac{W}{\sqrt{2(2\delta\nu\delta t)\left[\frac{N_c(N_c-1)}{2S_c^2} + \frac{N_cN_r}{S_cS_r} + \frac{N_r(N_r-1)}{2S_r^2}\right]}} \tag{1.94}$$

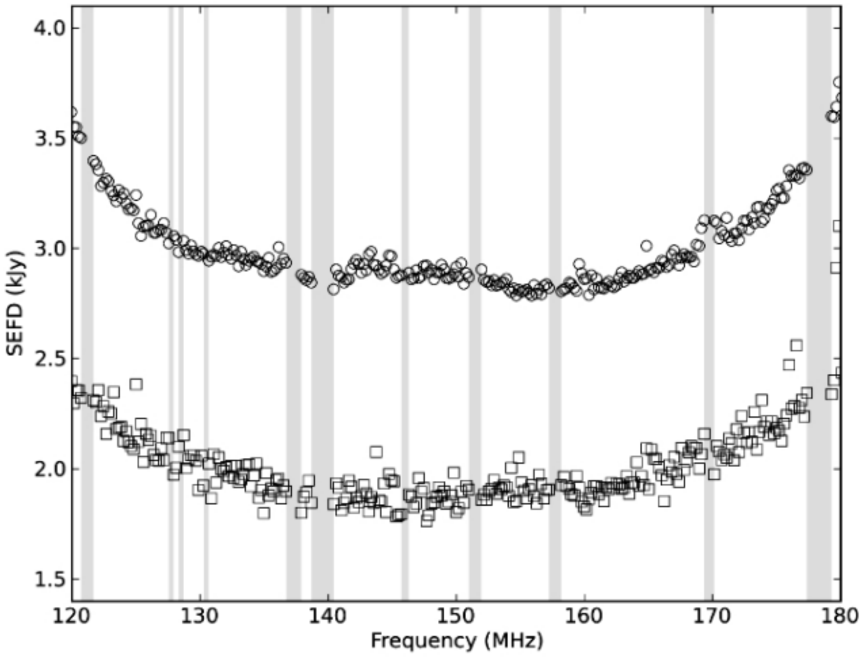

Figure 1.17 System equivalent flux density (SEFD) as a function of frequency for core stations (circles) and remote HBA stations (squares). Adapted from van Haarlem et al. (2013).

Here, W denotes the noise amplification factor introduced by the weighting scheme, while N_c and N_r represent the numbers of core and remote stations, respectively. The quantities S_c and S_r correspond to the SEFD values for the core and remote stations.

For simplicity, one may assume $S_c \approx S_r \approx S$ and define the total number of stations as $N = N_r + N_c$. In this case, Eq. 1.94 can be simplified to

$$\Delta S = \frac{S}{\sqrt{N(N-1)(2\delta\nu\delta t)}}. \tag{1.95}$$

1.9 Bayesian Monte Carlo Sampling

Bayesian Monte Carlo sampling is a widely used method in astrophysics and cosmology for reconstructing posterior distributions and recovering the likelihood surface (Lewis and Bridle, 2002; Bernardi et al., 2016; Sharma, 2017; Planck Collaboration et al., 2020). According to Bayes' theorem, the posterior distribution of the parameter set $\{\lambda_i\}$ given the data x_{obs} is:

$$P(\{\lambda_i\} \mid x_{obs}) \propto \mathcal{L}(x_{obs} \mid \{\lambda_i\})\, \Pi(\{\lambda_i\}), \tag{1.96}$$

where $\Pi(\{\lambda_i\})$ denotes the *prior* distribution and $\mathcal{L}(x_{obs} \mid \{\lambda_i\})$ is the *likelihood* function. Frequently, priors for each parameter λ_i are assumed to be independent and uniform, defined over the interval

$$\lambda_i \in [\lambda_{\mathrm{min},i}, \lambda_{\mathrm{max},i}]. \tag{1.97}$$

Assuming Gaussian, uncorrelated uncertainties, the log-likelihood is

$$\ln(\mathcal{L}(x_{\mathrm{obs}} \mid \{\lambda_i\})) \propto -\frac{1}{2}\sum_{\mathrm{obs}} \frac{[I_{\mathrm{obs}}(x_{\mathrm{obs}}) - I_{\mathrm{model}}(x_{\mathrm{obs}}, \{\lambda_i\})]^2}{\sigma^2_{\mathrm{obs}}(x_{\mathrm{obs}})}, \tag{1.98}$$

where $I_{\mathrm{obs}}(x_{\mathrm{obs}})$ is the observed profile evaluated at the observed points x_{obs}, $I_{\mathrm{model}}(x_{\mathrm{obs}}, \{\lambda_i\})$ is the model prediction profile evaluated at the same points and dependent on the parameter set $\{\lambda_i\}$, and $\sigma_{\mathrm{obs}}(x_{obs})$ represents the corresponding observational uncertainty.

The posterior distribution $P(\{\lambda_i\} \mid x_{\rm obs})$ is sampled using Markov Chain Monte Carlo (MCMC) techniques (Metropolis et al., 1953; Hastings, 1970) in order to reconstruct the parameter constraints. These methods construct a Markov chain whose equilibrium distribution corresponds to the target posterior.

In this work, we employ an affine-invariant ensemble sampler (Foreman-Mackey et al., 2013), which efficiently explores the parameter space even in the presence of strong correlations between parameters.

In the context of this thesis, this Bayesian framework serves as a statistical tool for analyzing the observed radio profiles. Specifically, in Chapter 2, this method will be applied to the Coma galaxy cluster to reconstruct the model emission. By exploring the likelihood surface via MCMC sampling, we evaluate the accuracy of the parameter reconstruction.

1.A Probing Magnetic Fields via Faraday Rotation

The magnetic field of the galaxy cluster can be derived from the Faraday effect

$$\Psi_{obs} = \Psi_{int} + \lambda^2 \cdot RM, \tag{1.99}$$

where Ψ_{obs} and Ψ_{int} are observed and initial polarization angle, λ is an observational wavelength and RM is a Faraday rotation measure.

$$RM \sim \int n_e(l)B_{||}(l)dl \tag{1.100}$$

It depends on the parallel component of the magnetic power of medium $B_{||}$ and the electron number density n_e along the line of sight. Last value could be measured from X-Ray observations. For Coma cluster n_e was well described by Briel et al. (1992) with β -model

$$n_e(r) = n_0 \left(1 + \frac{r^2}{r_c^2}\right)^{-\frac{3}{2}\beta} \tag{1.101}$$

For Coma cluster $\beta = 0.75 \pm 0.03$, $r_c = 291 \pm 17$ kpc, $n_0 = 3.44 \pm 0.04 \cdot 10^{-3}\mathrm{cm}^{-3}$. The polarization angle could be obtained from radio observations from each band separately For the polarization analysis, is used two images containing the Stokes Q and U components. These images allow to derive the linear polarization angle across the source from each band separately

$$\Psi = \frac{1}{2}\arctan\frac{U}{Q} \tag{1.102}$$

In the case of the Coma Cluster, Bonafede et al. (2010) estimate a central magnetic field strength of $B_0 = 4.7 \pm 0.7, \mu$G and a radial slope $\eta = 0.5 \pm 0.2$ (at the 1σ confidence level). The magnetic field was well described by a Kolmogorov power spectrum, with minimum and maximum scales of $\Lambda_{\min} \sim 2$ kpc and $\Lambda_{\max} \sim 34$ kpc, respectively. The magnetic field spatial profile is given by:

$$\langle B(r)\rangle = \langle B_0\rangle \left(\frac{n_e(r)}{n_0}\right)^{\eta} \tag{1.103}$$

The Kolmogorov power spectrum for a magnetic field describes how the field's energy is distributed across spatial scales in a turbulent medium. In this model Kolmogorov (1941) shows larger-scale fluctuations contain more energy, while smaller scales have progressively less, following a stochastic vector field with a power spectrum:

$$|B_k|^2 \propto k^{-n}, \quad k = \frac{2\pi}{\lambda} \tag{1.104}$$

where k is the wavenumber corresponding to scale λ and n is the Kolmogorov slope. The field is defined between a minimum Λ_{min} and maximum Λ_{max} scale, with the resulting $\langle B^2\rangle$ determining the local magnetic field strength.

1.B Dark Matter Density Profile

For a Dark Matter density profile will use Navarro-Frenk-White (NFW) profile (Navarro et al., 1996)

$$\rho_{NFW}(r) = \frac{\rho_s}{\frac{r}{r_s}\left(1 + \frac{r}{r_s}\right)^2} \tag{1.105}$$

where ρ_s and r_S is scale density and scale radius or in the other words are parameters of NFW-density profile.

$$M(x) = 4\pi\rho_s r_s^3 \left[\ln(1+x) - \frac{x}{1+x}\right] \quad (1.106)$$

where $x = r/r_s$.

According to Łokas and Mamon, 2003 the total mass of the Coma cluster within the virial radius of $2.9h_{70}^{-1}$ Mpc is $1.4 \cdot 10^{15} h_{70}^{-1}\ M_\odot$ (with 30% precision), 85%, of which it is dark matter. The distance also according to Łokas and Mamon (2003) is 101.3 Mpc.

Buote et al. (2007) derived an empirical relationship between the virial radius r_{vir} and the scale radius r_s from X-ray observations.

$$x_{vir} = \frac{r_{vir}}{r_s} = 9\left(\frac{M_{vir}}{10^{14} M_0 h^{-1}}\right)^{-0.172} \quad (1.107)$$

In the case of Coma Cluster

$$x_{vir} = 9\left(\frac{1.4 \cdot 10^{15} M_0}{10^{14} M_0 \cdot 0.7^{-1}}\right)^{-0.172} = 6.1 \quad (1.108)$$

$r_s = r_{vir}/x_{vir} = 0.475$ Mpc. And $\rho_s = 9.4 \cdot 10^5 M_0/kpc^3$.

Chapter 2

Coma Cluster

The chapter is organized as follows. In Section 2.1, we introduce the main properties of the Coma Cluster. Section 2.1.1 provides a brief overview of dark matter studies in Coma.

In Section 2.2, we describe the radio observational data used in this work. Next, Section 2.3 presents the astrophysical component of the cluster radio emission. In Section 2.4, we discuss the expected dark matter-induced emission and its dependence on the WIMP properties, including the annihilation cross section, particle mass, and annihilation channel.

In the following sections, we simulate dark matter and astrophysical emission profiles and apply the reconstruction method introduced in Section 1.9. This allows us to test the ability of the method to recover the input parameters of both emission components from synthetic data.

- In Section 2.6.1, we consider simulated dark matter emission alone, without any astrophysical background.
- Then, in Section 2.6.2 we investigate a more realistic scenario in which both the astrophysical and dark matter components are present.
- The simulations discussed in Section 2.6.2 reveal a strong degeneracy between the WIMP mass and the annihilation cross section for the Coma Cluster. As a result, these parameters cannot be constrained simultaneously unless the dark matter signal is unrealistically strong compared with the astrophysical emission. To overcome this limitation, in Section 2.6.3 we fix the annihilation cross section and treat the WIMP mass as the only free dark matter parameter, repeating the validation tests under this assumption.

Finally, in Section 2.7 the developed methodology is applied to the Coma Cluster observations to derive upper limits on the WIMP annihilation cross section as a function of the WIMP mass.

2.1 Coma Galaxy Cluster

The Coma galaxy cluster (Abell 1656) is one of the most studied galaxy clusters (Gunn and Gott, 1972, White and Rees, 1978, Marinacci et al., 2018), located in the constellation Coma Berenices at RA = 12h 59m 48.72s, DEC = $+27^\circ\, 58'\, 51.6''$, with a redshift of $z = 0.02310 \pm 6 \cdot 10^{-5}$ (Dhawan et al., 2018; Bird et al., 2016).

Zwicky (1933), using the virial theorem and the observed velocity dispersion of individual galaxies, estimated the total virial mass of the Coma cluster. By comparing this value with the mass inferred from the cluster luminosity, he was led to propose the existence of unseen (dark) matter. Later studies, for example Łokas and Mamon (2003), performed a more precise analysis of the dark matter distribution in the Coma Cluster. They employed more advanced dynamical models, in particular the Jeans equation (Binney and Mamon, 1982), taking into account orbital anisotropy inferred from galaxy kinematics. They obtained a virial mass and radius of $M_{\rm vir} = 1.4 \times 10^{15}\,M_\odot$ and $r_{\rm vir} = 2.9\,$Mpc, respectively, with an uncertainty of approximately 30%.

Beyond its mass content, the Coma Cluster also hosts a large-scale magnetic field, whose strength and structure are central to this work: the synchrotron emission produced by DM-induced electrons and positrons depends directly on the cluster magnetic field. Bonafede et al. (2010) derived a central magnetic field strength of $B_0 = 4.7 \pm 0.7\,\mu$G, with a radial slope of $\eta = 0.5 \pm 0.2$, both constrained at the 1σ level. Moreover, it was shown that the magnetic field power spectrum is well described by a Kolmogorov spectrum with a minimum scale $\Lambda_{\rm min} \sim 2\,$kpc and a maximum scale $\Lambda_{\rm max} \sim 34\,$kpc.

The main properties of the Coma Cluster are summarized in Table 2.1.

Coma Cluster

Parameter	Value
$M_{vir}\ 10^{15}\ [M_\odot]$	1.4 ± 0.4
R_{vir} [Mpc]	2.9 ± 0.9
R_{vir} [arcmin]	99 ± 29
Distance [Mpc]	101.3
B_0 [μG]	4.7 ± 0.7
η	0.5 ± 0.2
r_c [kpc]	291 ± 17
$n_e(0)$ [10^{-3} cm^{-3}]	3.44 ± 0.04
β	0.75 ± 0.03

Table 2.1 Main properties of the Coma Cluster, summarized from Section 2.1, assuming $h_0 = 0.67$ (Planck Collaboration et al., 2020). The last five parameters describe the electron number density and magnetic field.

2.1.1 Dark Matter Studies in Coma Cluster

The Coma Cluster has played a key role in the study of dark matter since the pioneering work of Zwicky (1933), who first pointed out the presence of a large amount of unseen mass in the system.

Subsequent studies investigated the cluster mass distribution using a variety of techniques, including the spatial distribution of galaxies, galaxy kinematics, and the assumption of hydrostatic equilibrium (Kent and Gunn, 1982; The and White, 1986; Geller et al., 1999; Łokas and Mamon, 2003). In more recent analysis, several authors employed weak gravitational lensing to estimate the virial mass of the cluster, reconstruct its mass distribution, and study dark matter subhalos (Kubo et al., 2007; Gavazzi et al., 2009; Okabe et al., 2014).

The Coma Cluster has also been extensively investigated as a target for indirect dark matter searches. Using observations from VERITAS (Weekes et al., 2002, Very Energetic Radiation Imaging Telescope Array System), Arlen et al. (2012) derived upper limits on the WIMP annihilation cross section in the order of $\sim 10^{-20}$–$10^{-21}\,$cm^{3}s^{-1} for the W^+W^-, $\tau^+\tau^-$, and $b\bar{b}$ annihilation channels, assuming WIMP masses between 100 GeV and 10 TeV.

Similarly, Ackermann et al. (2010) analyzed 11 months of Fermi-LAT observations of nearby galaxy clusters, including Coma, and obtained constraints on dark matter annihilation cross section. For the $b\bar{b}$ annihilation channel, they derived upper limits of approximately

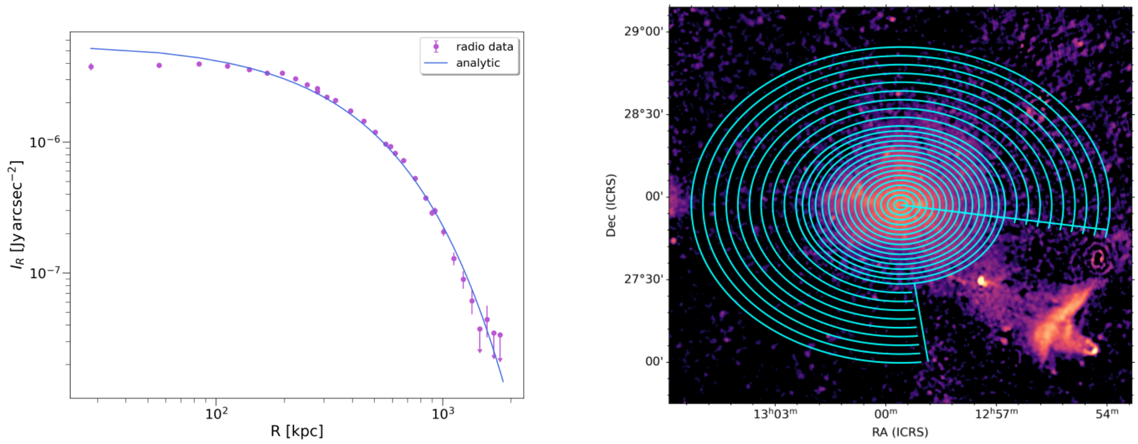

Figure 2.1 Left panel shows Coma cluster observational surface brightness with uncertainties corresponding to 1σ standard deviations at 144 MHz and best-fit model $I_0 \exp(-R/R_0)$. The right panel presents the concentric regions in the Coma Cluster were used to derive its radial emission profile. The radio relic in the lower-right was excluded from the diffuse emission analysis. From Bonafede et al. (2022)

$10^{-23}\,\mathrm{cm^3s^{-1}}$ for a 10 GeV WIMP and $\sim 10^{-21}\,\mathrm{cm^3s^{-1}}$ for a 1 TeV WIMP. Using 12 years of Fermi-LAT observations, Thorpe-Morgan et al. (2021) improved these limits by one order of magnitude.

The possibility of detecting dark matter annihilation through radio observations of the Coma Cluster was discussed by Colafrancesco et al. (2006) and Storm et al. (2017). In particular, Storm et al. (2017) showed that observations with LOFAR, ASKAP, and other radio facilities could probe WIMP models with masses up to approximately 100 GeV with the thermal annihilation cross section. Earlier, Colafrancesco et al. (2006) analyzed radio observations spanning frequencies from 30 MHz to 5 GHz (Thierbach et al., 2003, and others, references therein). Assuming that the entire radio halo emission originates from dark matter annihilation, they obtained a best-fit model with a WIMP mass of approximately 40 GeV and an annihilation cross section of $\langle \sigma v \rangle = 4.7 \cdot 10^{-25}\,\mathrm{cm^3s^{-1}}$ for the $b\bar{b}$ annihilation channel.

In this work, we use sensitive LOFAR observations of the Coma Cluster to test the predictions of Storm et al. (2017). In addition, we assume that the observed diffuse emission consists of both an astrophysical component and a possible contribution from WIMP annihilation.

2.2 Diffuse Radio Emission in the Coma Cluster from LOFAR observations

In this section, we examine the surface radio brightness distribution of the Coma Cluster as observed at 144 MHz with the Low Frequency Array (LOFAR) from Bonafede et al. (2022), see Fig. 2.1. A detailed discussion of the LOFAR instrument is presented in Section 1.8, where we describe the specifics of radio observations, calibration procedures, data reduction, and image reconstruction. Here, we focus on the astrophysical interpretation of the observed emission.

We model the diffuse radio emission as the sum of two components, distinguished by the origin of the relativistic electrons responsible for the emission. Both astrophysical and DM-induced electrons produce synchrotron radiation, and thus the emission mechanism is identical in the two cases. The first component, hereafter denoted as the *astrophysical component*, arises from a population of relativistic electrons of conventional origin (e.g. AGNs, cosmic rays, and other sources) accelerated within the intracluster medium.

The second component, hereafter referred to as *the dark matter component*, is attributed to a potential signal arising from dark matter particle annihilation. It corresponds to synchrotron emission produced by electrons and positrons generated as secondary products of dark matter annihilation, which then radiate via synchrotron emission in the intracluster medium. We assume that the two components radiate independently, owing to the different spatial distributions of their underlying electron populations; therefore, their contributions to the total emission are additive.

2.3 Astrophysical Emission Component

Many galaxy clusters exhibit diffuse radio emission, which is commonly interpreted as synchrotron radiation produced by relativistic cosmic rays propagating in large-scale magnetic fields within the intracluster medium (Feretti et al., 2012; van Weeren et al., 2019). In this work, we do not attempt to model the physical origin of this component; instead, it is treated as an astrophysical background to the potential dark matter-induced emission.

We model this astrophysical component with a simple exponential profile that provides a good empirical description of the observed brightness distribution of the radio halo (Murgia et al., 2009, Boxelaar et al., 2021, Bonafede et al., 2022):

$$I(R) = I_0 e^{(-R/R_0)}\,, \tag{2.1}$$

where I_0 is the central surface brightness and R_0 is the scale radius at which the brightness decreases by a factor of e. The left panel of Fig. 2.1 shows the astrophysical model (solid line) together with the measured emission data of the Coma Cluster (dots).

The dark matter component is modeled separately, with its surface brightness profile depending on the annihilation channel, WIMP mass and annihilation cross section. A detailed analysis of the dark matter emission component is presented in Section 2.4.

Given parametric models for both components, we apply the statistical inference method described in Section 1.9 and applied in Sections 2.6.1–2.7 to recontract their respective parameters, which allows us to assess the detectability of a dark matter annihilation signature in the radio observations of the Coma Cluster.

2.4 Dark Matter Emission Component

DM radio emission in Coma Cluster was initially searched by Colafrancesco et al. (2006), see also Section 2.1.1. Colafrancesco et al. (2006) assumed that the total emission was produced by the DM annihilation process, and neglected the astrophysical background, that is instead included in our analysis. However, they analyzed data at different frequencies, while in this thesis we use observations taken at a single frequency (i.e. 144 MHz).

To compute the spatial profile of the DM-induced synchrotron emission, we use the DarkMatters code (Sarkis and Beck, 2025). The underlying methodology is described in Section 1.5. In Sections 2.4.1 and 2.4.2, we investigate how the predicted signal depends on the WIMP annihilation channel, mass and cross-section.

In Section 2.5, we build an interpolation of the simulated signal, since it was simulated in a fixed grid and we want to find an analytical function that describes it, which will subsequently be used for the reconstruction of dark matter parameters.

2.4.1 Annihilation Channels

In our default setup, we adopt an annihilation cross section of $\langle \sigma v \rangle_0 = 10^{-26}\,\mathrm{cm}^3\,\mathrm{s}^{-1}$, since it is of the same order as the thermal relic cross section (see Section 1.4.3) and is commonly used in dark matter indirect-detection studies. We consider dark matter particle masses of 10 GeV, 100 GeV, and 1000 GeV.

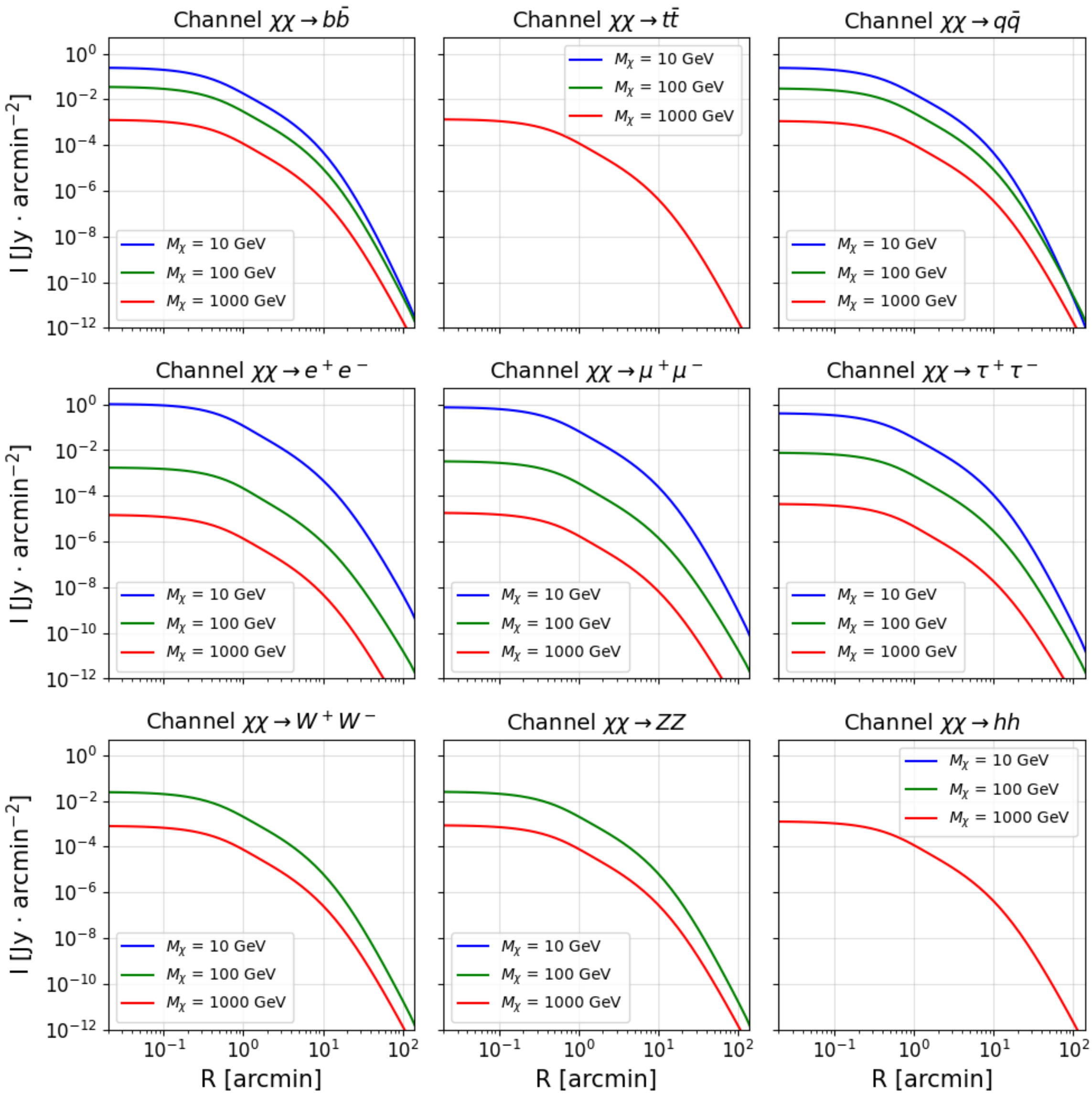

Figure 2.2 Synchrotron surface brightness profiles produced by secondary electrons from dark matter annihilation for nine representative annihilation channels. Each panel shows the predicted synchrotron flux density as a function of the angular distance from the center of the Coma Cluster, for three dark matter masses $M_\chi = 10,\ 100,\ 1000$ GeV. All panels share the same spatial and flux scales to allow a direct comparison of the radial profiles and their mass dependence. For some channels, such as W^+W^-, the spatial profile for a dark matter mass of 10 GeV is not available. This is because, the rest energy of the DM particle is below the rest mass of the W boson.

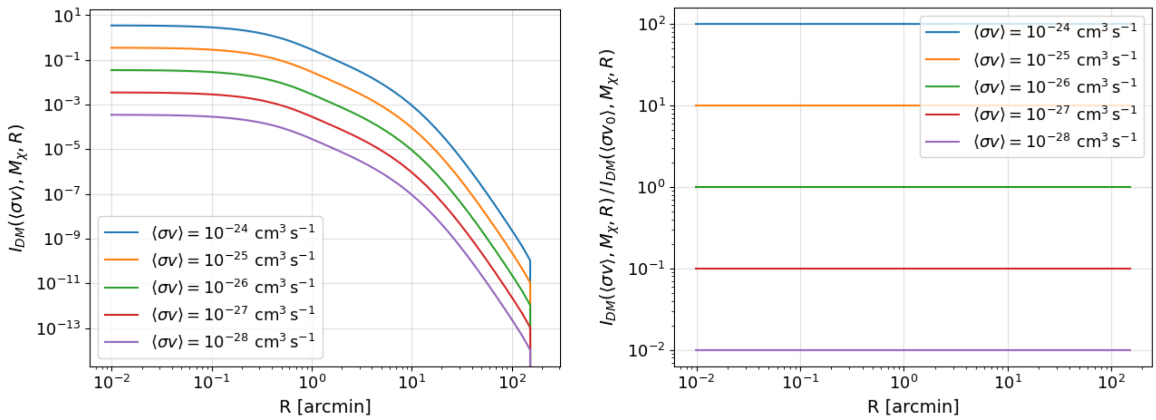

Figure 2.3 Dependence of the expected surface brightness on the dark matter annihilation cross-section for $M_\chi = 100$ GeV. The left panel shows the absolute simulated value of the flux, while the right panel displays the ratio of the surface brightness for a given cross section to that obtained for $\langle \sigma v_0 \rangle = 10^{-26}\,\text{cm}^3\,\text{s}^{-1}$.

Dark matter may annihilate through several channels (Cirelli et al., 2011; Ciafaloni et al., 2011); the final states considered in this work are e^+e^- (electrons and positrons), $\mu^+\mu^-$ (muons), $\tau^+\tau^-$ (tau leptons), $b\bar{b}$ (bottom quarks), $t\bar{t}$ (top quarks), W^+W^- and ZZ (electroweak gauge bosons), and hh (Higgs bosons). The surface brightness profile expected from synchrotron radiation is shown in Fig. 2.2 for each of these channels and for the three different WIMP masses.

In a realistic scenario, all possible annihilation channels should contribute, weighted by their branching ratio (see Eq. 1.59). For simplicity, we restrict our analysis to the $b\bar{b}$ annihilation channel, because this is expected to provide the brightest radio emission among all the channels.

2.4.2 Dependence of the Expected Surface Brightness on the Dark Matter Interaction Cross Section

We generate dark matter surface brightness profiles for the three dark matter particle masses, $M_\chi = 10$, 100, and 1000 GeV, and for five different annihilation cross-sections, $\langle \sigma v \rangle = 10^{-28}$, 10^{-27}, 10^{-26}, 10^{-25}, and 10^{-24} cm^3 s^{-1}. The simulation results demonstrate that the total radio emission flux from the galaxy cluster scales linearly with the WIMP annihilation cross-section (see Fig. 2.3).

Moreover, according to the theoretical framework (see Section 1.5 and Eq. 1.67), the surface brightness $I(r)$ depends linearly on the source term $Q(E, r)$ and therefore scales linearly with the annihilation cross-section. For clarity, we reproduce the relevant equations here:

$$Q(E,r) = \frac{1}{2}\left(\frac{\rho_\chi(r)}{M_\chi}\right)^2 \langle \sigma v \rangle \frac{dN_i}{dE}$$

$$\frac{dn_e}{dE}(E,r) = \frac{1}{b_{loss}(E,r)} \int_E^{M_\chi c^2} Q(E',r)dE'$$

$$J_\nu(r) = 2\int_{m_e c^2}^{M_\chi c^2} P(\nu,E,r)\frac{dn_e}{dE}(E,r)dE$$

$$I(r) = \frac{1}{4\pi}\int_0^\infty J(r')\frac{r'dr'}{\sqrt{r'^2 - r^2}}.$$

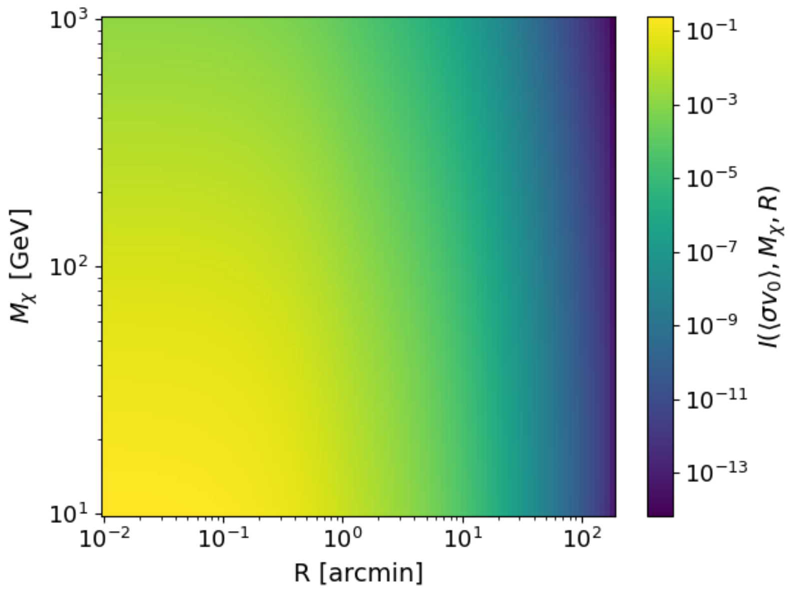

Figure 2.4 Interpolated surface brightness of the Coma cluster in units of Jy $\cdot$ arcmin^{-2} as a function of the WIMP mass M_χ and the distance R from the cluster center. Cross-section is fixed at $\langle\sigma v_0\rangle = 10^{-26}\,\mathrm{cm^3 s^{-1}}$.

Here, dn_e/dE is the injected electron number density power spectrum, $P(\nu, E, r)$ is the single electron synchrotron power emissivity, and $J_\nu(r, \nu)$ is the total cluster emissivity per unit volume at the frequency ν.

We can therefore write I_{DM} (see Eq. 2.2), where we express the profile for any given cross-section as a rescaled function of a reference profile (labeled 0):

$$I_{DM}(\langle\sigma v\rangle, M_\chi, R) = \frac{\langle\sigma v\rangle}{\langle\sigma v_0\rangle} I_{DM}(\langle\sigma v_0\rangle, M_\chi, R). \tag{2.2}$$

2.5 Interpolation of Dark Matter Signal Profiles

To model the expected flux of synchrotron emission from DM-induced particles, we constructed a cubic spline using the `RectBivariateSpline` module from the `scipy.interpolate` library. The resulting spline function is illustrated in Figure 2.4.

The original spline was constrained on 800 points along the radius and 34 logarithmically spaced points in mass. To validate the accuracy of the interpolation, we tested the spline on a separate grid whose nodes differ from those of the original computation grid (179 linearly spaced points in radius and 20 logarithmically spaced points in mass). This test revealed that the main interpolation errors occur at large radial values, corresponding to regions with weak flux. The relative error was found to be below 1%. The relative interpolation errors are shown in Fig. 2.5 and Fig. 2.6.

2.6 Profile Reconstruction

Before applying the inference method discussed in Section 1.9 to the observations, we first verify its ability to recover known input parameters from noisy data. For this purpose, we generate synthetic radial astrophysical profiles $I(R)$ (see Eq. 2.1) using a simple parametric model. Realistic random noise is then added to simulate observational uncertainties. The simulated data are subsequently analyzed with the reconstruction procedure, and the recovered

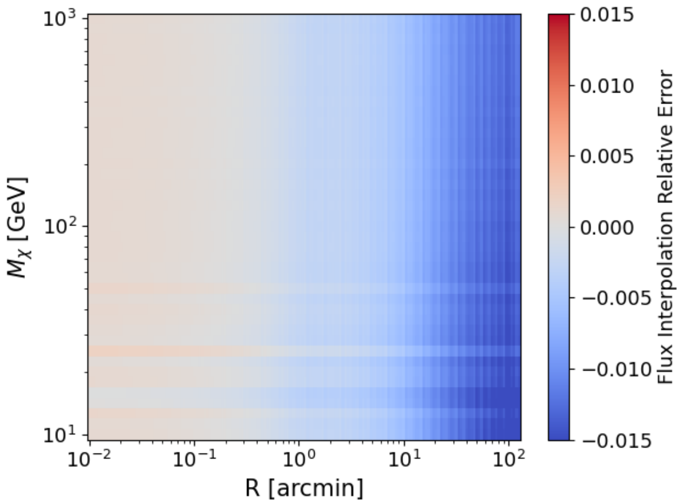

Figure 2.5 Two-dimensional distribution of the spline relative error. The vertical axis corresponds to particle mass [GeV], and the horizontal axis corresponds to radius [arcmin]. The color scale represents the relative error of the interpolation, which does not exceed 1.5% over most of the interpolation domain. The non-smooth behaviour for $M_\chi \lesssim 100\,\text{GeV}$ can be attributed to the relative structure of the computational and test grids, where the spacing between corresponding points is not uniform.

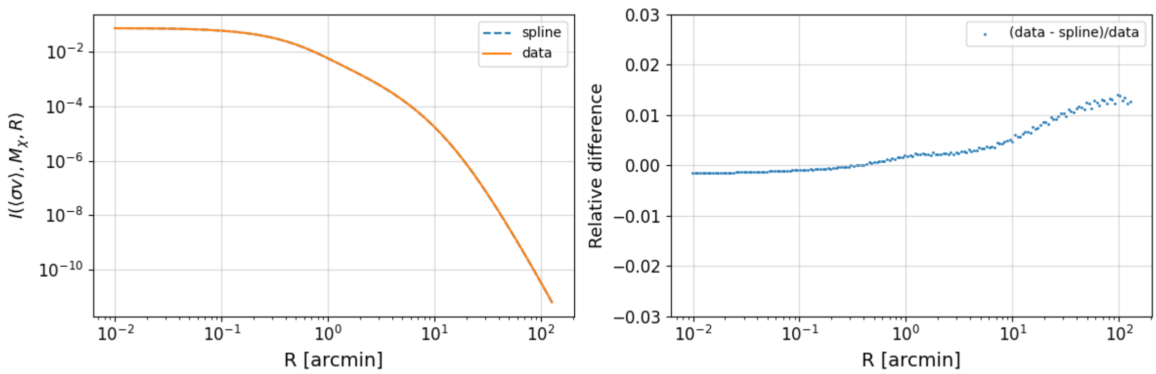

Figure 2.6 One-dimensional slice of the spline at a particle mass of 50 GeV. The horizontal axis represents the distance from the center, while the vertical axis shows the relative difference between the spline interpolation and the original data. This illustrates the interpolation accuracy along the radial coordinate for a representative particle mass.

parameters are compared with the input values. This test allows us to assess the accuracy and robustness of the method before applying it to observational data.

To recover the input parameters, we use the Markov Chain Monte Carlo (MCMC) method, as implemented in the `emcee` Python library Foreman-Mackey et al. (2013). This algorithm allows us to reconstruct the posterior distributions and likelihood surfaces of the parameters and yields their expectation values and covariance matrix.

For the first validation, we adopt a simple exponential profile:

$$I(R) = I_0 \exp\left(-\frac{R}{R_0}\right), \tag{2.3}$$

with input values $I_0 = 20\,\text{mJy} \cdot \text{arcmin}^{-2}$ and $R_0 = 10$ arcmin.

We generated a synthetic profile at 30 radial points between 1 and 60 arcmin. Gaussian noise with zero mean and standard deviations of 1, 5, 10, and 25% was added to the profile, producing one noisy dataset for each noise level. Each dataset was then analyzed independently

Table 2.2 Reconstructed values of the parameters I_0 and R_0 obtained from *MCMC* simulations with different noise levels added to the initial data. The errors correspond to 1σ uncertainties.

Noise level	1%	5%	10%	25%
I_0 [mJy · arcmin^{-2}]	19.94 ± 0.06	20.2 ± 0.3	20.2 ± 0.6	15.7 ± 1.2
R_0 [arcmin]	10.01 ± 0.01	9.93 ± 0.05	9.88 ± 0.10	10.14 ± 0.27

Parameter	1% noise	2% noise	5% noise	10% noise
$\langle\sigma v\rangle$ [$10^{-26}\,\mathrm{cm}^3 \cdot \mathrm{s}^{-1}$]	3.0 ± 0.1	2.9 ± 0.1	2.6 ± 0.3	2.8 ± 0.5
M_χ [GeV]	99 ± 2	97 ± 4	89 ± 9	92 ± 17

Table 2.3 Recovered values of the annihilation cross section $\langle\sigma v\rangle$ and the dark matter particle mass M_χ obtained from the simulated signal for different levels of added noise. The errors correspond to 1σ uncertainties.

using MCMC. The reconstructed parameters and their uncertainties, derived from the posterior distributions, are summarized in Table 2.2.

As expected, the parameter uncertainties increase with the noise level. While the input parameters are recovered within uncertainties for noise levels up to 10%, the parameter I_0 becomes underestimated at 25% noise, indicating a indicating a noise limit at which the parameter best fit values are biased.

As will be shown below, the astrophysical component is recovered with high accuracy in nearly all cases, at a level comparable to the precision of the simulations.

2.6.1 Test 1. Accuracy of Dark Matter Signal Reconstruction at Different Noise Levels

Having validated the reconstruction framework (Section 1.9) using a simple parametric profile, we proceed to a series of validation tests. In particular, we consider three scenarios of increasing complexity: (i) reconstruction of a pure dark matter signal at different noise levels (Section 2.6.1); (ii) joint reconstruction of dark matter and astrophysical components, with the annihilation cross section treated as the only free dark matter parameter (Section 2.6.2); and (iii) a full joint reconstruction in which both the annihilation cross section and the WIMP mass are treated as free parameters (Section 2.6.3).

We simulate a dark matter signal assuming a thermal annihilation cross section $\langle\sigma v\rangle = 3 \cdot 10^{-26}\,\mathrm{cm}^3\,\mathrm{s}^{-1}$ and a WIMP mass $M_\chi = 100\,\mathrm{GeV}$ for all simulated cases. Gaussian noise with relative amplitudes of 1%, 2%, 5%, and 10% is added to the signal. We then analyze how accurately the original signal can be reconstructed under these noise levels. The recovered parameters are presented in Table 2.3.

In all cases, we were able to accurately reconstruct both dark matter parameters mass M_χ and cross-section $\langle\sigma v\rangle$ within 2σ of the statistical uncertainty. An example of the posterior distribution for this case is shown in Figure 2.7.

2.6.2 Test 2. Reconstruction of Both Dark Matter Parameters with an Astrophysical Component

In the second test case, we include an astrophysical component modeled by an exponential profile in addition to the dark matter signal.

We then fix the noise level at 1%, assume a dark matter particle mass of 100 GeV, and vary the annihilation cross section over the range from 1 to 1000 in units of 10^{-26} $\mathrm{cm}^3\mathrm{s}^{-1}$. Increasing the annihilation cross section enhances the dark matter signal (see Eq. 2.2). Subsequently,

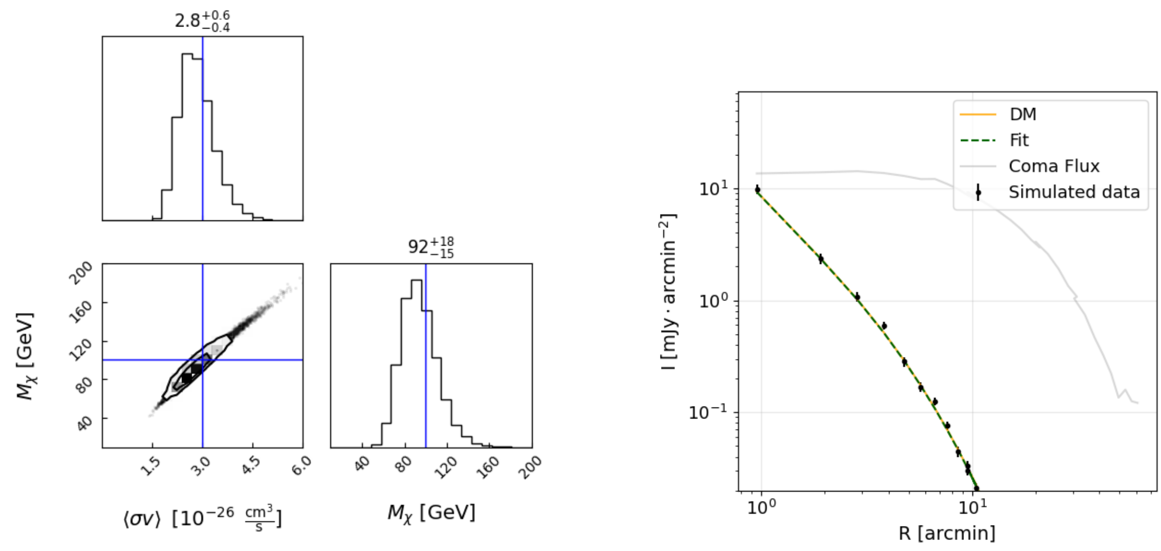

Figure 2.7 Left panel shows posterior distribution and covariance between $\langle\sigma v\rangle$ and M_χ. For simulated data with 10% Gaussian noise amplitude. The contours show the 68% and 95% confidence regions. The right panel shows the simulated dark matter emission (black points) and the corresponding best-fit model (green dashed line). For comparison, the observed Coma Cluster signal is shown in gray.

Table 2.4 Recovered parameters for different input annihilation cross-sections, assuming a fixed noise level of 1% and a WIMP mass of 100 GeV throughout the simulations.

	Astrophysical component		Dark matter		
$\langle\sigma v\rangle_{\mathrm{model}}$ $[10^{-26}\,\mathrm{cm}^3\,\mathrm{s}^{-1}]$	I_0 [mJy arcmin^{-2}]	R_0 [arcmin]	$\langle\sigma v\rangle_{\mathrm{rec}}$ $[10^{-26}\,\mathrm{cm}^3\,\mathrm{s}^{-1}]$	m_{WIMP} [GeV]	I_{DM}/I_A
1000	19.79 ± 0.22	10.02 ± 0.02	1293^{+399}_{-299}	125^{+30}_{-25}	170
500	19.75 ± 0.19	10.03 ± 0.02	865^{+420}_{-275}	157^{+55}_{-42}	86
250	19.81 ± 0.20	10.02 ± 0.02	511^{+565}_{-276}	179^{+391}_{-83}	34
100	19.84 ± 0.12	10.02 ± 0.02	406^{+1007}_{-274}	295^{+391}_{-168}	17
10	19.92 ± 0.07	10.01 ± 0.01	168^{+60}_{-78}	766^{+168}_{-257}	1.7
1	19.93 ± 0.06	10.01 ± 0.01	$17.1^{+6.0}_{-8.6}$	769^{+167}_{-282}	0.17

we reconstruct the parameters of both the astrophysical and dark matter components. The results are presented in Table 2.4.

The astrophysical component is well recovered in all simulations, with an accuracy better than $\sim$ 1%–2%. However, the dark matter parameters show large uncertainties, with posterior distributions that deviate significantly from Gaussian shapes.

Even the simulated noise levels are sufficiently small to allow a detection of both components, the presence of the astrophysical signal introduces strong parameter degeneracies, which lead to biased estimates and increased uncertainties in the dark matter parameters.

At the 95% confidence level, the two components can be reliably disentangled only in the presence of a sufficiently strong dark matter signal, which must exceed the peak amplitude of the astrophysical component by a factor of approximately $I_{\mathrm{DM}}/I_{\mathrm{A}}\big|_{R=0} \approx 34$.

We repeat the analysis at 2% noise to identify the minimum DM-to-astrophysical brightness ratio at which the two DM parameters can still be independently constrained in a worse scenario.

The validation test results are summarized in Table 2.5. When the noise level is increased from 1% to 2%, the minimum annihilation cross section required to distinguish the both

Table 2.5 Recovered parameters for different input annihilation cross-sections, assuming a fixed noise level of 2% and a WIMP mass of 100 GeV throughout the simulations.

	Astrophysical component		Dark matter		
$\langle\sigma v\rangle_{model}$ $[10^{-26}\,\mathrm{cm}^3\,\mathrm{s}^{-1}]$	I_0 [mJy arcmin^{-2}]	R_0 [arcmin]	$\langle\sigma v\rangle_{rec}$ $[10^{-26}\,\mathrm{cm}^3\,\mathrm{s}^{-1}]$	m_{WIMP} [GeV]	I_{DM}/I_A
2000	19.43 ± 0.49	10.06 ± 0.05	3920^{+1770}_{-1050}	152^{+60}_{-41}	340
1500	20.25 ± 0.48	9.95 ± 0.05	1560^{+840}_{-460}	104^{+44}_{-28}	260
1200	19.52 ± 0.51	10.05 ± 0.06	2200^{+1950}_{-1050}	167^{+100}_{-68}	200
1000	19.40 ± 0.49	10.06 ± 0.07	2460^{+2800}_{-1330}	207^{+150}_{-95}	170
500	19.38 ± 0.31	10.07 ± 0.04	3070^{+3940}_{-2020}	395^{+291}_{-212}	86

Table 2.6 Recovered parameters for different input annihilation cross-sections, assuming a WIMP mass of 100 GeV and a fixed noise level of 5% throughout the simulations.

	Astrophysical component		Dark matter		
$\langle\sigma v\rangle_{model}$ $[10^{-26}\,\mathrm{cm}^3\,\mathrm{s}^{-1}]$	I_0 [mJy arcmin^{-2}]	R_0 [arcmin]	$\langle\sigma v\rangle_{rec}$ $[10^{-26}\,\mathrm{cm}^3\,\mathrm{s}^{-1}]$	m_{WIMP} [GeV]	I_{DM}/I_A
12 000	16.95 ± 2.35	10.27 ± 0.25	31400^{+45000}_{-15900}	221^{+202}_{-94}	2000
8 000	17.41 ± 1.44	10.26 ± 0.17	35000^{+52000}_{-24000}	440^{+370}_{-250}	1400
5 000	16.95 ± 2.35	10.27 ± 0.25	32100^{+70300}_{-20600}	300^{+364}_{-162}	860

components at a given confidence level increases by approximately a factor of 4–5. Under these conditions, the dark matter parameters (mass and cross section) can be independently constrained only if the peak brightness of the dark matter component exceeds that of the astrophysical component by a factor of about $I_{\mathrm{D}M}/I_{\mathrm{A}}\big|_{R=0} \approx 200$.

We then performed an analogous simulation for a noise level of 5%. The results are presented in Table 2.6. In this case, the two DM parameters can be independently distinguished at the 95% confidence level only if the peak brightness of the dark matter emission exceeds that of the astrophysical component by a factor of approximately $I_{\mathrm{D}M}/I_{\mathrm{A}}\big|_{R=0} \approx 2000$.

In all of the cases considered, the parameters of the astrophysical component are recovered with an accuracy of up to 15%, even when its peak brightness is 2000 times lower than that of the dark matter emission. This validation test demonstrates that the WIMP parameters, mass and annihilation cross section, are strongly interdependent and exhibit significant mutual correlation, as illustrated in Figures 2.8 and 2.9.

2.6.3 Test 3. Reconstruction of DM Annihilation Cross-section with an Astrophysical Component

In this exercise, we fix the mass of the dark matter particle M_χ at 100 GeV, while treating the annihilation cross-section $\langle\sigma v\rangle$ only as a free parameter and changing its input values. An astrophysical component, analogous to that employed in Section 2.6.2, is added to the dark matter emission. Gaussian random noise with amplitudes of 1% and 10% is subsequently applied to the resulting signal, and we attempt to recover both the dark matter annihilation cross-section $\langle\sigma v\rangle$ and the astrophysical parameters I_0 and R_0.

Table 2.7 presents the recovered components of the astrophysical emission I_0 and R_0, and the WIMP annihilation cross-section $\langle\sigma v\rangle$ for the 1% noise level case. We find that it is possible to reliably identify the presence of dark matter even in cases where the ratio of DM

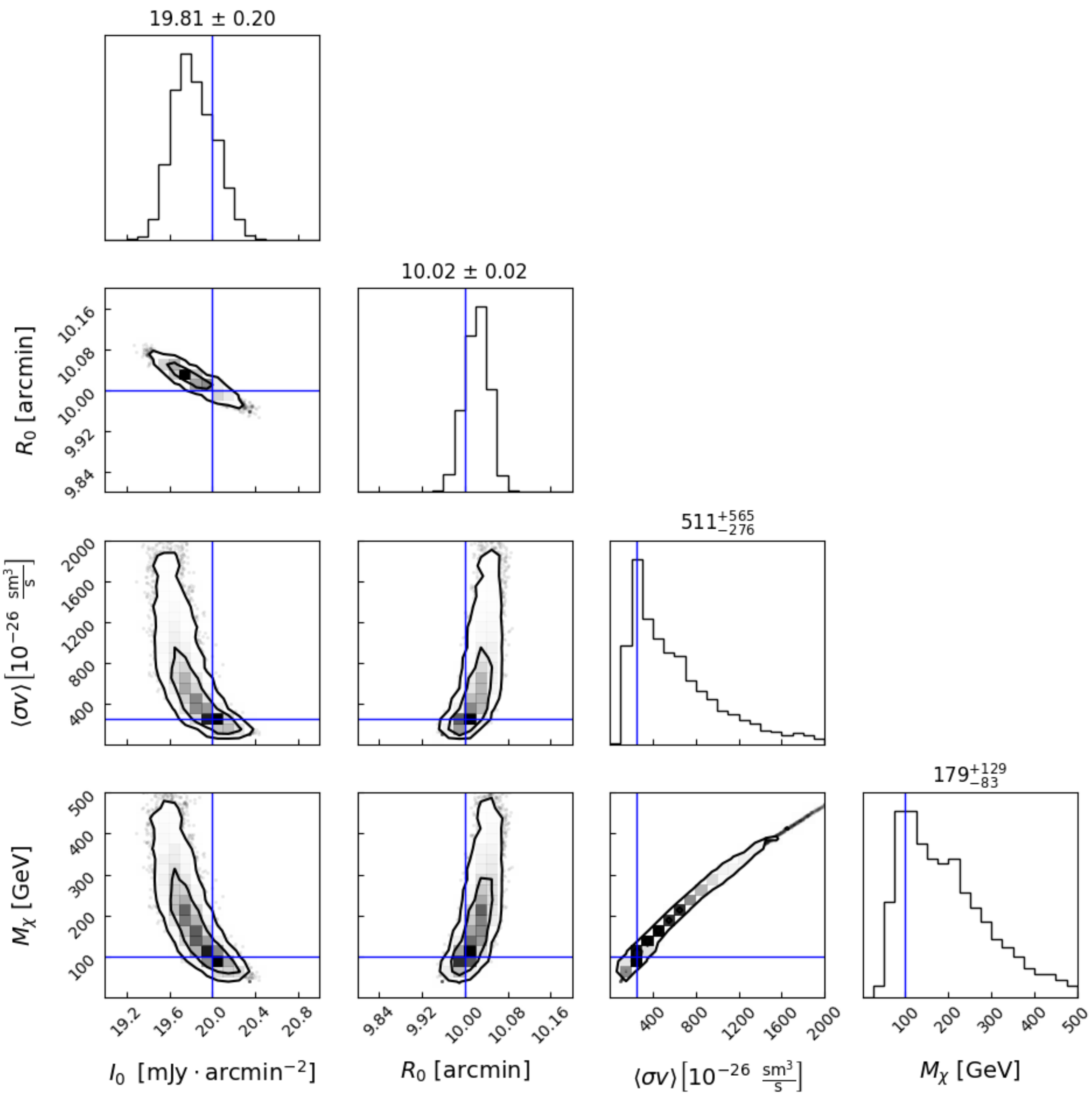

Figure 2.8 Posterior distributions and covariance plots for the astrophysical component parameters I_0 and R_0, as well as the dark matter component parameters (mass M_χ and annihilation cross section $\langle\sigma v\rangle$). The peak dark matter signal is 34 times higher than that of the astrophysical component. Blue lines indicate the input data used in the simulation. The noise level is 1%.

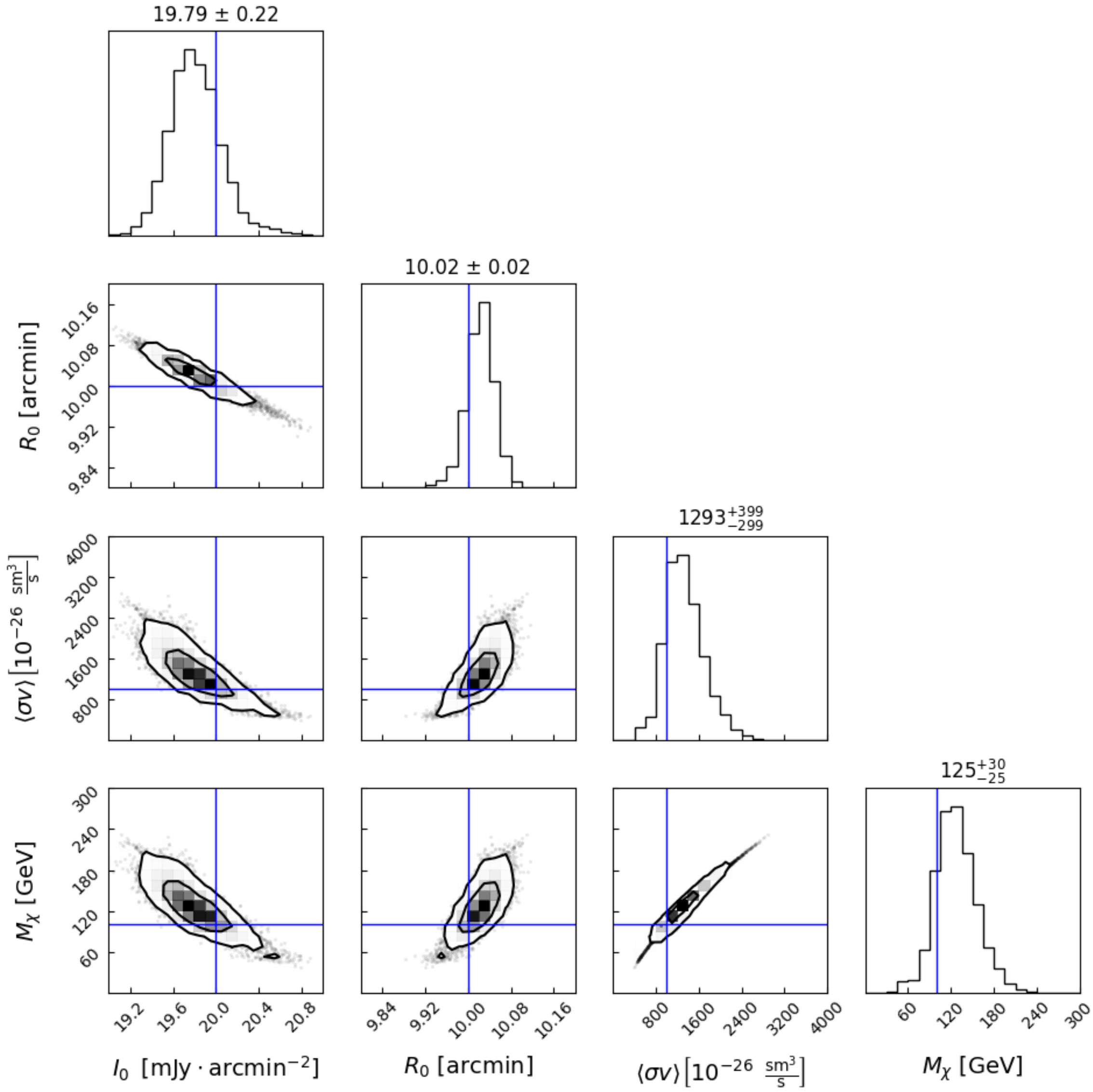

Figure 2.9 Posterior distributions and covariance plots for the astrophysical component parameters I_0 and R_0, as well as the dark matter component parameters (mass M_χ and annihilation cross section $\langle\sigma v\rangle$). The peak dark matter signal is 170 times higher than that of the astrophysical component. Blue lines indicate the input data used in the simulation. The noise level is 1%.

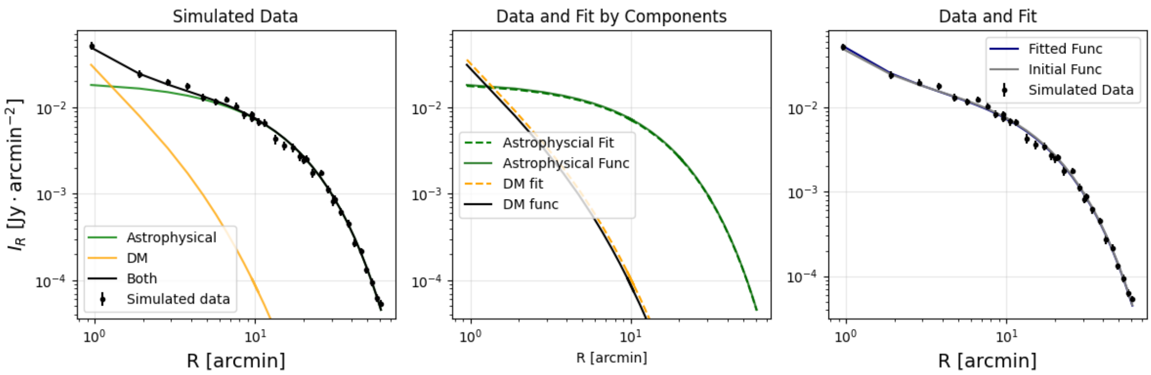

Figure 2.10 The left panel shows the astrophysical component with parameters $I_0 = 20$ mJy $\cdot$ arcmin^{-2} and $R_0 = 10$ arcmin (solid green line), together with the dark matter component (solid orange line) for $\langle\sigma v\rangle = 10 \times 10^{-26}$ cm^3 s^{-1} and $M_\chi = 100$ GeV. The black points represent simulated data with a noise level of 10% of the signal. The central panel presents the recovered astrophysical parameters, $I_0 = 19.47 \pm 0.69$ and $R_0 = 10.02 \pm 0.12$, which are in excellent agreement with the input values. In contrast, the reconstructed dark matter parameters, $\langle\sigma v\rangle = (182^{+77}_{-96}) \times 10^{-26}$ cm^3 s^{-1} and $M_\chi = 749^{+179}_{-243}$ GeV, differ by nearly an order of magnitude from the input values. Nevertheless, these incorrect parameter values still provide a good fit to the dark matter signal, indicating a strong degeneracy between the parameters. The right panel shows the simulated data together with the sum of the reconstructed components.

to the astrophysical component is 0.014, which corresponds to an annihilation cross section $\langle\sigma v\rangle \approx 8 \cdot 10^{-28}$cm^{3}s^{-1}. In such a scenario, the presence of dark matter can be detected at the 95% confidence level.

In Test 2, DM could only be identified when its signal was at least a factor of 34 stronger than the astrophysical component, corresponding to an annihilation cross section $\langle\sigma v\rangle \approx 2.5 \cdot 10^{-24}$cm^{3}s^{-1}. In contrast, in the present case, the dark matter contribution amounts to only 1–2% of the astrophysical component. This corresponds to an improvement in sensitivity of more than three orders of magnitude.

An example of the posterior distributions for the recovered parameters, in the case where the peak dark matter signal is 0.05 of the astrophysical component, is shown in Fig. 2.11.

We then repeated the simulation with the noise level increased to 10%. The results are presented in Table 2.8. In this case, we are still able to confidently identify the presence of a dark matter signal at the 95% confidence level, provided that the dark matter signal is no less

Table 2.7 Recovered parameters for different input annihilation cross-sections, assuming a fixed noise level of 1% and a fixed WIMP mass of 100 GeV throughout the simulations.

	Astrophysical component		Dark matter	
$\langle\sigma v\rangle_{model}$ [10^{-26} cm^3 s^{-1}]	I_0 [mJy arcmin^{-2}]	R_0 [arcmin]	$\langle\sigma v\rangle_{rec}$ [10^{-26} cm^3 s^{-1}]	I_{DM}/I_A
10	19.95 ± 0.07	10.00 ± 0.01	$10.15^{+0.014}_{-0.014}$	1.7
3	19.96 ± 0.06	10.01 ± 0.01	$3.08^{+0.09}_{-0.09}$	0.5
1	19.98 ± 0.06	10.01 ± 0.01	$1.02^{+0.07}_{-0.07}$	0.17
0.3	19.98 ± 0.06	10.01 ± 0.01	$0.321^{+0.064}_{-0.065}$	0.05
0.1	19.98 ± 0.06	10.01 ± 0.01	$0.125^{+0.061}_{-0.061}$	0.017
0.08	19.98 ± 0.06	10.01 ± 0.01	$0.105^{+0.059}_{-0.055}$	0.014

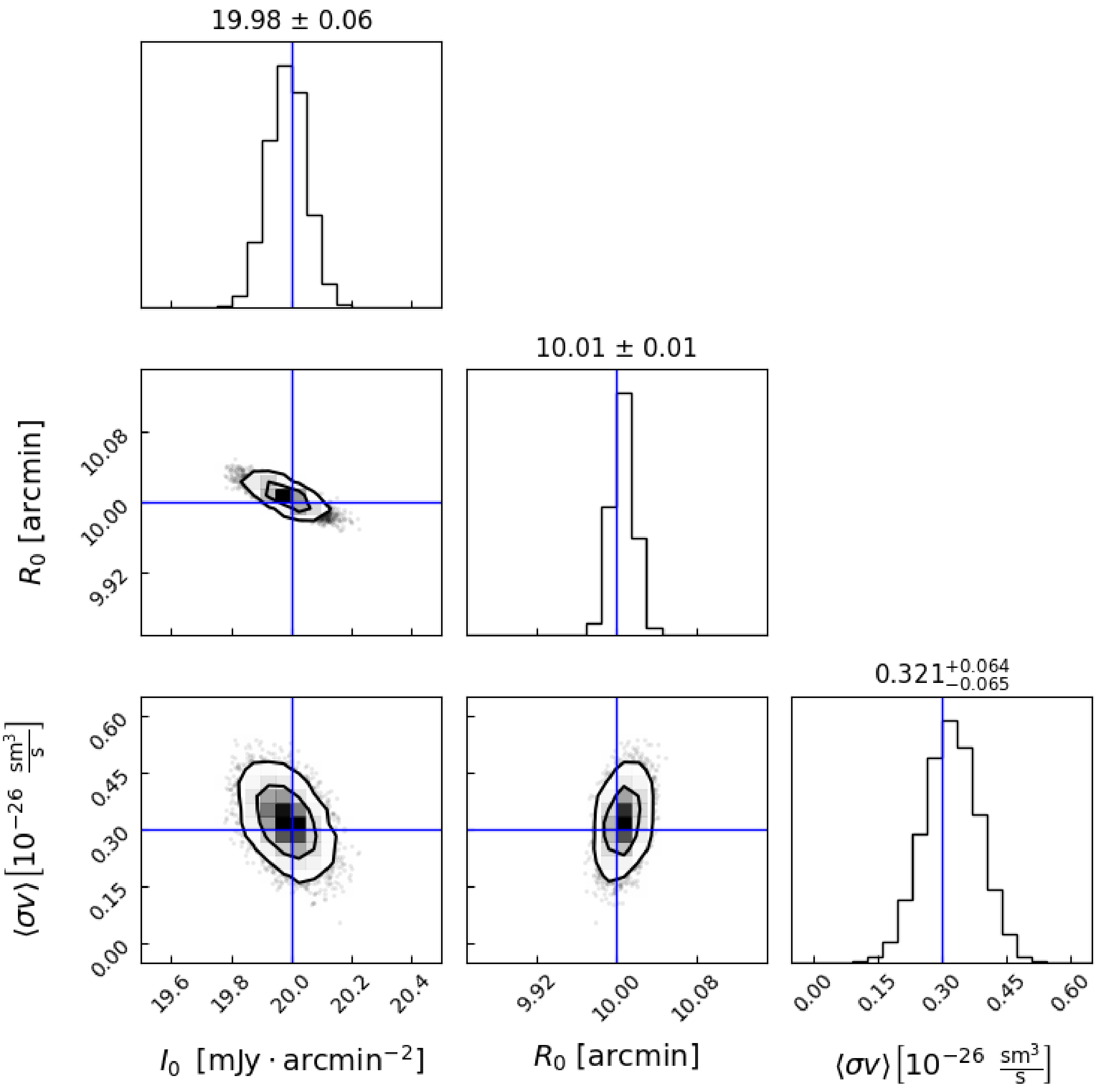

Figure 2.11 Posterior distributions and covariance plots for the astrophysical component parameters I_0 and R_0, as well as the dark matter parameter annihilation cross section $\langle \sigma v \rangle$. Mass of DM particle is fixed along the simulations M_χ at 100 GeV. The peak dark matter signal, as shown in Table 2.7, is 0.05 times the peak of the astrophysical component. Blue lines indicate the input data used in the simulation. The noise level is 1%.

Table 2.8 Recovered parameters for different input annihilation cross-sections, assuming a fixed noise level of 10% and a fixed WIMP mass of 100 GeV throughout the simulations.

	Astrophysical component		Dark matter	
$\langle\sigma v\rangle_{model}$ $[10^{-26}\,\mathrm{cm^3\,s^{-1}}]$	I_0 [mJy arcmin^{-2}]	R_0 [arcmin]	$\langle\sigma v\rangle_{rec}$ $[10^{-26}\,\mathrm{cm^3\,s^{-1}}]$	I_{DM}/I_A
10	19.83 ± 0.66	10.06 ± 0.11	$10.3^{+1.4}_{-1.4}$	1.7
3	19.81 ± 0.65	10.06 ± 0.11	$3.28^{+0.87}_{-0.87}$	0.5
2	19.84 ± 0.062	10.06 ± 0.11	$2.26^{+0.77}_{-0.80}$	0.35
1.5	19.84 ± 0.063	10.06 ± 0.11	$1.74^{+0.72}_{-0.71}$	0.25
1	19.79 ± 0.062	10.07 ± 0.11	$1.26^{+0.66}_{-0.64}$	0.17

than 17% of the astrophysical component, yields an annihilation cross section of approximately $\langle\sigma v\rangle \approx 10^{-26}\mathrm{cm^3 s^{-1}}$.

We then performed a set of analogous simulations in which the annihilation cross-section was fixed, while the dark matter mass was treated as a free parameter. In this case, the mass can also be successfully recovered. However, this type of simulation is subject to certain limitations. Specifically, in constructing the interpolation model for the expected dark matter emission from the Coma Cluster, we considered only a restricted mass range, from 10 GeV to 1000 GeV. As a result, the recovered posterior distributions frequently exhibit tails extending beyond the upper bound of 1000 GeV.

From the theoretical considerations discussed in Sections 1.3–1.5, we can expect WIMP parameters of $\langle\sigma v\rangle \approx 3\cdot 10^{-26}\,\mathrm{cm^3\,s^{-1}}$ and $M_\chi \approx$ 100–1000 GeV. These correspond to a relative flux $I_{\mathrm{D}M}/I_A\big|_{R=0}$ of approximately 1–50%. As shown in Test 2, in order to independently measure both the mass and the annihilation cross-section, the relative flux must be at least 2–3 orders of magnitude higher.

We find a strong degeneracy between the two dark matter parameters. In the regime relevant for current observational noise levels (from 1% to $\sim$ 10%), the two parameters cannot be independently constrained. However, they can be jointly constrained through an effective combined parameter, leading to an improvement in sensitivity of approximately three orders of magnitude compared to the independent-fit case. This degeneracy motivates the introduction of the K_{teDM} parametrization, which will be presented in Section 2.6.6.

2.6.4 Degeneracy of the Dark Matter Mass and Cross Section

The results of the previous validation test demonstrate a strong degeneracy between the dark matter mass and annihilation cross-section. The WIMP mass primarily affects the shape of the emission profile, while the annihilation cross-section determines its normalization.

However, as shown in Fig. 2.12, the spatial brightness profiles are nearly identical for different WIMP masses. Noticeable differences in the profile shapes appear only at large radii (10–100 arcmin), where the absolute flux is low and the signal is dominated by noise or by the astrophysical component.

A similar issue was noted by Regis et al. (2014) in their analysis of WIMP parameters based on radio observations of Local Group dwarf spheroidal galaxies at a wavelength of 16 cm with the Australia Telescope Compact Array. They state: *Since the analysis is performed using a single energy bin and the injected spectrum has only a weak effect on the spatial morphology of the source, the fit cannot disentangle the degeneracy between the particle mass and the annihilation rate, both of which enter primarily through the overall signal normalization.*

In the following Section 2.6.5, we investigate how the expected surface brightness of the dark matter signal depends on the WIMP mass and derive an empirical relation describing this dependence, Eq. 2.6.

We then propose two approaches for reconstructing WIMP parameters. The first method is based on the empirical relation, see Eq. 2.4 and Eq. 2.6, derived in Section 2.6.5, and is described in Section 2.6.3.

The second method follows the approach proposed by Regis et al. (2021), in which the WIMP mass is fixed while the annihilation cross-section is fitted. A 95% confidence interval for the cross-section is then determined, and the procedure is repeated for different assumed WIMP masses.

2.6.5 Dependence of the Expected Surface Brightness on the Dark Matter Interaction Particle Mass

As demonstrated in Section 2.6.2, the presence of the astrophysical component introduces strong degeneracies that prevent a reliable reconstruction of the dark matter parameters. However, the problem can be reformulated. Rather than attempting to determine both dark matter parameters directly, we first ask whether the observational data contain a statistically significant dark matter signal, in the following, we introduce this criterion, denoted by $K_{\rm DM}$. We then investigate its dependence on the WIMP mass and cross section.

For this purpose, We attempted to parameterize the three-dimensional function $I(\langle\sigma v\rangle, M_\chi, R)$. As shown in Section 2.4.2, it is directly proportional to the WIMP annihilation cross-section. First, let us rewrite the Eq. 2.2

$$I(\langle\sigma v\rangle, M_\chi, R) = \frac{\langle\sigma v\rangle}{\langle\sigma v_0\rangle} I(\langle\sigma v_0\rangle, M_\chi, R)\,.$$

We then aim to factorize $I(\langle\sigma v_0\rangle, M_\chi, R)$ into separate functions of mass and radius, effectively performing a separation of variables. For simplicity, we denote $I(M_\chi, R) \equiv I(\langle\sigma v_0\rangle, M_\chi, R)$.

We define

$$F_{ratio}(M_\chi, R) = \frac{I(M_\chi, R)}{I(M_{0\chi}, R)}\,, \tag{2.4}$$

which is the ratio of the dark matter flux for the WIMP masses $M_\chi = 10, 10^3$ and 10^4 GeV to that for a fixed reference mass $M_{0\chi} = 100$ GeV. This is shown in the Fig. 2.12.

As shown in Fig. 2.12, the function $F_{ratio}(M_\chi, R)$ remains approximately constant over a wide range of R see table 2.9. Towards the virial radius, $R \to R_{vir}$ (on the order of 10^2 arcmin), $F_{ratio}(M_\chi, R)$ sharply increases and approaches unity. This behavior arises because both fluxes, $I(M_\chi, R)$ and $I(M_{0\chi}, R)$, rapidly decrease to zero in this regime. When the radius is changed by a factor of 100, from 0.1 to 10 arcmin, we see that the flux for $b\bar{b}$ and $\mu^+\mu^-$-channels changes by several thousand times. However, the ratio of fluxes between different particle masses does not exceed 1.5; see table 2.9.

The dependence of $F_{ratio}(M_\chi, R)$ via all studied mass regions is presented on the left panel of Fig. 2.14.

Based on this observation, we average $F_{ratio}(M_\chi, R)$ over R, obtaining:

$$\langle F_{ratio}(M_\chi)\rangle_R = \langle F_{ratio}(M_\chi, R)\rangle\,. \tag{2.5}$$

The corresponding dependence on M_χ is shown in the left panel of Fig. 2.13. The error bars reflect both the statistical uncertainty from averaging and the contribution from interpolation errors (see Section 2.5).

We then fit $\langle F_{ratio}(M_\chi)\rangle_R$ with the function

$$\langle F_{ratio}(M_\chi)\rangle_{interp} = \exp\left[a\ln^2\left(\frac{M_\chi}{M_{0\chi}}\right) + b\ln\left(\frac{M_\chi}{M_{0\chi}}\right) + c\right]\,, \tag{2.6}$$

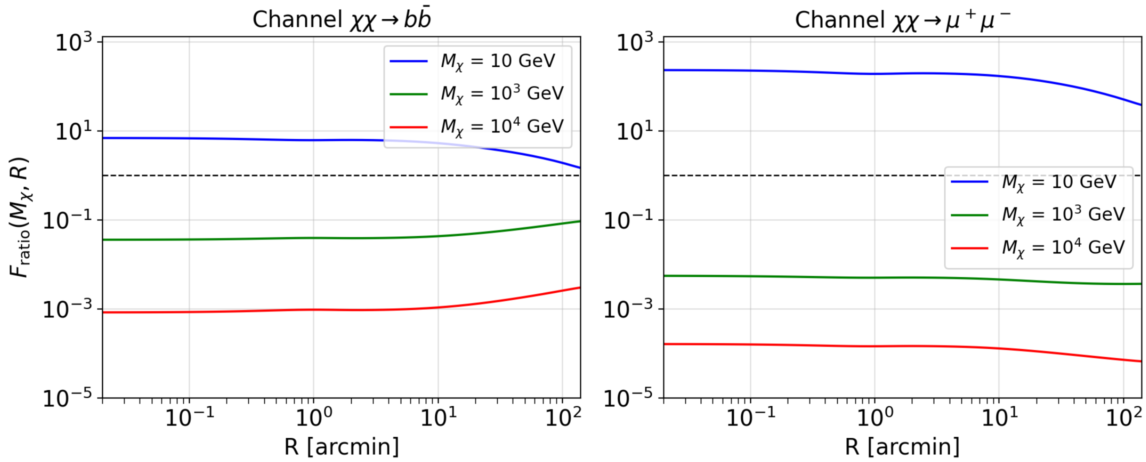

Figure 2.12 Radial profiles of the ratio $F_{ratio}(M_\chi, R) = I(M_\chi, R)/I(M_{0\chi}, R)$ for $b\bar{b}$ and $\mu^+\mu^-$ channels. Dark matter masses $M_\chi = 10$ GeV, 1000 GeV and 10^4 GeV, with $M_{0\chi} = 100$ GeV as the reference. The ratio remains nearly constant over most of the radial range, indicating that the shape of the synchrotron flux profiles is largely independent of the dark matter mass. Near the virial radius ($R \sim 10^2$ arcmin), the ratio rises sharply toward unity, reflecting the rapid decrease of both fluxes at large radii.

which was chosen empirically as it provides an accurate description of the observed mass dependence across the considered range. The best-fit parameters a, b and c, which are presented in table 2.10 and in the right panel of Fig. 2.13.

As a consistency check, we divided $I(M_\chi, R)$ by both $I(M_{0\chi}, R)$ and $\langle F_{ratio}(M_\chi)\rangle_{interp}$ (see Eq. 2.6). The result is shown in the right panel of Fig. 2.14. Perfect agreement between the analytical expression and the interpolated function would correspond to a value of unity on the color-bar. We find that the discrepancy of the model does not exceed a factor of 2 across the parameter space, while the total variation of the original function spans approximately eight orders of magnitude.

Table 2.9 Synchrotron fluxes and ratios for selected radii for the $b\bar{b}$ and $\mu^+\mu^-$ annihilation channels. We focus primarily on the $b\bar{b}$ channel, while also presenting the corresponding behavior for the $\mu^+\mu^-$ channel for comparison. The first column shows the approximate angular distance from the center of the galaxy cluster, the second column the flux for $M_\chi = 10$ GeV, and the third and fourth columns the ratios $I(100\text{ GeV})/I(10\text{ GeV})$ and $I(1000\text{ GeV})/I(10\text{ GeV})$ at this given R.

$b\bar{b}$ channel			
R	$I_{10\text{ GeV}}$	$F(100\text{ GeV})$	$F(1000\text{ GeV})$
$0.1'$	1.919×10^{-1}	1.475×10^{-1}	5.336×10^{-3}
$10'$	5.474×10^{-5}	1.878×10^{-1}	8.063×10^{-3}
Ratio	3.5×10^{-3}	1.27	1.50
$\mu^+\mu^-$ channel			
R	$I_{10\text{ GeV}}$	$F(100\text{ GeV})$	$F(1000\text{ GeV})$
$0.1'$	6.178×10^{-1}	4.446×10^{-3}	2.412×10^{-5}
$10'$	2.711×10^{-4}	5.846×10^{-3}	2.698×10^{-5}
Ratio	2.3×10^{3}	1.31	1.12

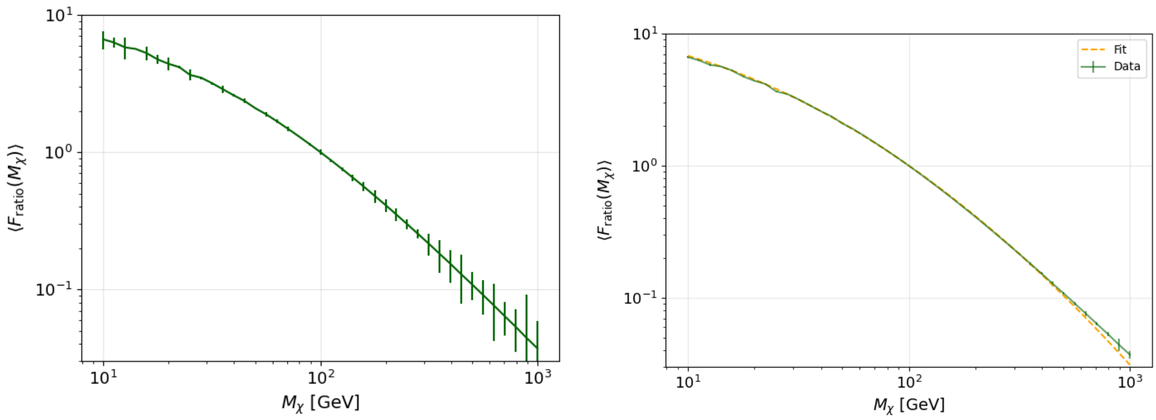

Figure 2.13 The left panel shows $\langle F_{ratio}(M_\chi)\rangle_R$ as a function of the WIMP mass. The error bars are enlarged by a factor of 10 for visualization clarity. The right panel presents the fit described by Eq. 2.6, with error bars shown at their true scale. The corresponding fit parameters are listed in Table 2.10.

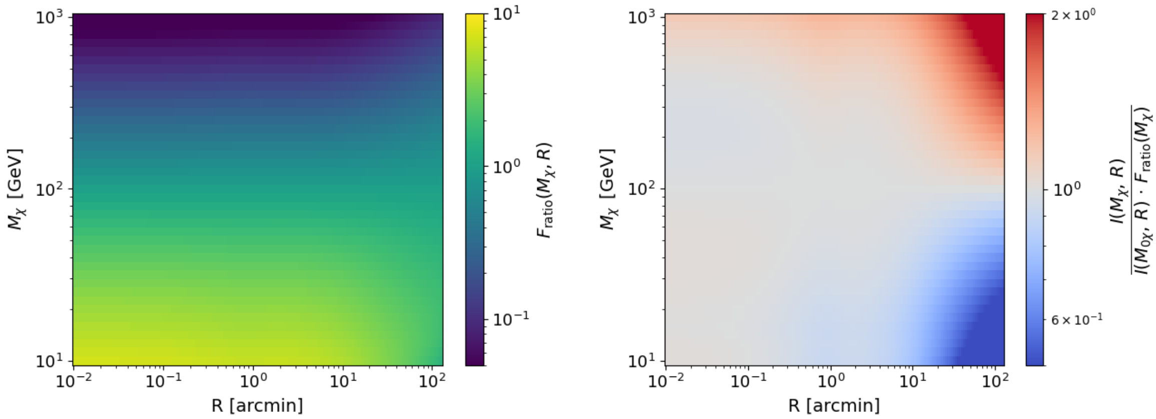

Figure 2.14 The left panel shows $F_{ratio}(M_\chi, R)$ (see Eq. 2.4) as a function of the dark matter particle mass and the distance from the center of the galaxy cluster. The right panel presents the deviation from the factorized model. This deviation does not exceed a factor of 2 across nearly the entire dataset, while the absolute flux varies by approximately eight orders of magnitude over the considered range.

2.6.6 Constraining a Combined Dark Matter Parameter

In this section, we identify a combination of the WIMP mass and annihilation cross-section, rather than attempting to constrain them independently.

The simulated signal is modeled as the sum of an astrophysical component and a contribution of dark matter. The astrophysical component is taken to be the same as before,

$$I_A(R) = I_0 \exp(-R/R_0)\,, \tag{2.7}$$

Table 2.10 Best-fit parameters for $\langle F_{ratio}(M_\chi)\rangle_{interp}$ from Eq. 2.6

Parameter	Value	Uncertainty
a	-1.47×10^{-1}	2×10^{-3}
b	-1.170	3×10^{-3}
c	2.5×10^{-3}	1.4×10^{-3}

Table 2.11 Recovered parameters for different input annihilation cross-sections, assuming a fixed noise level of 10% and a fixed cross-section of $3 \times 10^{-26}\,\mathrm{cm}^3 \cdot \mathrm{s}^{-1}$ throughout the simulations.

DM model		Astrophysical component		Dark matter	
M_χ [GeV]	K_{model}	I_0 [mJy arcmin^{-2}]	R_0 [arcmin]	K_{rec}	I_{DM}/I_A
1000	0.093	19.70 ± 0.60	10.08 ± 0.11	$0.56^{+0.51}_{-0.37}$	0.02
800	0.14	19.73 ± 0.59	10.08 ± 0.10	$0.58^{+0.54}_{-0.38}$	0.0285
500	0.31	18.57 ± 0.61	10.21 ± 0.11	$0.67^{+0.55}_{-0.43}$	0.058
300	0.70	19.77 ± 0.61	10.07 ± 0.11	$1.02^{+0.62}_{-0.58}$	0.123
250	0.91	19.66 ± 0.64	9.99 ± 0.11	$1.51^{+0.70}_{-0.66}$	0.16
100	3.00	19.59 ± 0.66	10.01 ± 0.12	$3.78^{+0.86}_{-0.89}$	0.5

Table 2.12 Recovered parameters for different input annihilation cross-sections, assuming a fixed noise level of 1% and a fixed cross-section of $1 \times 10^{-26}\,\mathrm{cm}^3 \cdot \mathrm{s}^{-1}$ throughout the simulations.

DM model		Astrophysical component		Dark matter	
M_χ [GeV]	K_{model}	I_0 [mJy arcmin^{-2}]	R_0 [arcmin]	K_{rec}	I_{DM}/I_A
1000	0.031	19.97 ± 0.08	10.01 ± 0.01	$0.080^{+0.078}_{-0.050}$	0.0067
750	0.052	19.96 ± 0.09	10.01 ± 0.02	$0.101^{+0.109}_{-0.058}$	0.010
500	0.104	19.97 ± 0.08	10.01 ± 0.01	$0.146^{+0.084}_{-0.065}$	0.019
300	0.232	19.96 ± 0.07	10.00 ± 0.01	$0.299^{+0.081}_{-0.067}$	0.04
150	0.608	19.91 ± 0.06	10.01 ± 0.01	$0.719^{+0.065}_{-0.066}$	0.1

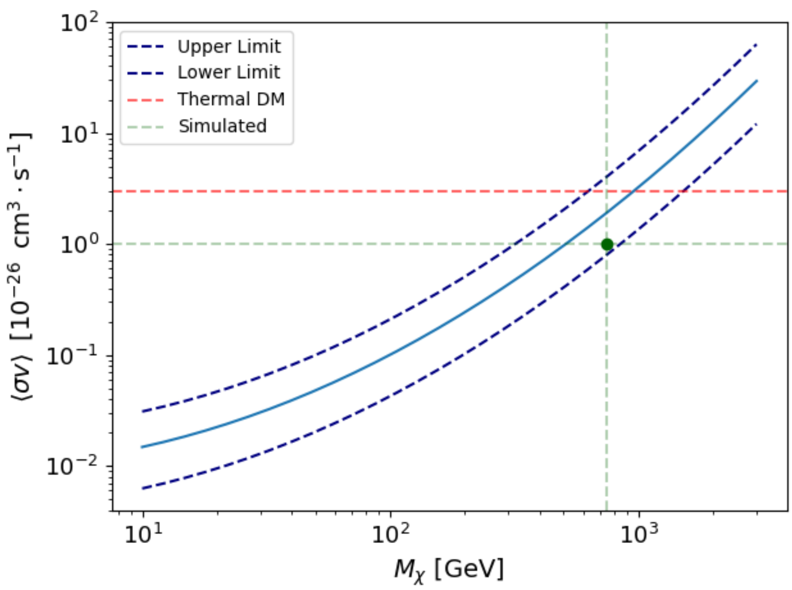

Figure 2.15 The solid blue line shows the dependence of the WIMP annihilation cross-section as a function of the WIMP mass (see Eq. 2.10). The blue dashed lines indicate the upper and lower limits of the dark matter parameter space (1-σ). The green dashed lines represent the mass and annihilation cross-section values used in the simulation, $M_\chi = 750$ GeV and $\langle\sigma v\rangle = 1 \times 10^{-26}$ cm^3 s^{-1}, respectively; their intersection marks the true input value. The noise level along the modeling was set to 1%. The orange line denotes the thermal WIMP annihilation cross-section, $\langle\sigma v\rangle = 3 \times 10^{-26}$ cm^3 s^{-1}.

while the dark matter component is given by

$$I(\langle\sigma v\rangle, M_\chi, R) = \frac{\langle\sigma v\rangle}{\langle\sigma v_0\rangle}\langle F_{ratio}(M_\chi)\rangle_{interp} \cdot I(\langle\sigma v_0\rangle, M_{0\chi}, R)\,. \tag{2.8}$$

We then apply the procedure described in Sections 2.6.2 and 2.6.3. As the reconstructed quantity, we consider a combination of the WIMP mass and annihilation cross-section, defined as

$$K_{\mathrm{D}M} \equiv \frac{\langle\sigma v\rangle}{\langle\sigma v_0\rangle}\langle F_{\mathrm{r}atio}(M_\chi)\rangle\,. \tag{2.9}$$

This allows us to express the annihilation cross-section as a function of mass,

$$\langle\sigma v\rangle(M_\chi) = \frac{K_{\mathrm{D}M}}{\langle F_{\mathrm{r}atio}(M_\chi)\rangle}\,. \tag{2.10}$$

As a criterion for successful signal detection, we use the parameter $K_{\mathrm{D}M}$ and its associated uncertainty $\sigma_{K_{\mathrm{D}M}}$ Specifically, we require

$$K_{\mathrm{D}M} > 2\,\sigma_{K_{\mathrm{D}M}}\,. \tag{2.11}$$

In the case where the dark matter signal is approximately 0.16 of the astrophysical component, we are still able to successfully recover the dark matter parameters. The results of the simulations are presented in Table 2.11.

We then reduced the noise level from 10% to 1% and performed an analogous simulation. The results are presented in Table 2.12. In this case, even if the dark matter signal is about 50–100 times weaker than the astrophysical component, it can still be reliably distinguished according to the 2.11 criteria. An example of the recovered dependence of the WIMP annihilation cross-section on the WIMP mass is shown in Fig. 2.15.

2.7 Constraining Dark Matter Parameters in the Coma Cluster

In this section, we apply the algorithm described in Section 2.6.6 to Coma Cluster data from Bonafede et al. (2022).

The data set consists of 32 points that describe the radial profile over 1 – 60 arcmin from the center of the cluster. We exclude the last three points, which are upper limits on the radio flux. This has negligible impact on the analysis, since simulations indicate that the dark matter signal is expected to be concentrated near the cluster center, flux in the outer regions is 6–8 orders of magnitude lower. The fit combines an astrophysical component (Eq. 2.7) and a dark matter component (Eq. 2.8).

The results of the fitting procedure are presented in Figs. 2.16 and 2.17. In the central region of the Coma Cluster, a lack of excess signal is observed, and the astrophysical component leaves little "room" for a dark matter contribution. From the posterior distribution we recover an upper-limit for the $K_{\mathrm{D}M}$ parameter (see Eq. 2.9), which characterizes the presence of dark matter. We find $K_{\mathrm{D}M} < 0.079$ at 95% of CL (see the left panel of Fig. 2.16).

At the emission peak, the dark matter contribution is significantly weaker than the astrophysical component, with $I_{\mathrm{D}M}/I_A\big|_{R=0} \approx 2.6 \times 10^{-3}$ (see the right panel of Fig. 2.16). Moreover, the peak surface brightness of the dark matter component is approximately 5×10^{-2} mJy · arcmin^{-2}, which is well below the noise level $\sigma_{rms} = 0.4$ mJy · arcmin^{-2} according to Bonafede et al. (2022, Table 2).

Using Eq. 2.10, we derive the dependence of the annihilation cross-section on the WIMP mass. Assuming a thermal annihilation cross-section of $\langle\sigma v\rangle = 3 \times 10^{-26}$ cm^3 s^{-1}, we find that our analysis excludes the WIMP masses below 1070 GeV with 95% of confidence level (see Fig. 2.17). The quoted confidence intervals account only for the statistical uncertainties of the profile reconstruction. Systematic uncertainties associated with the magnetic field model, dark matter density profile, and other cluster parameters are not included.

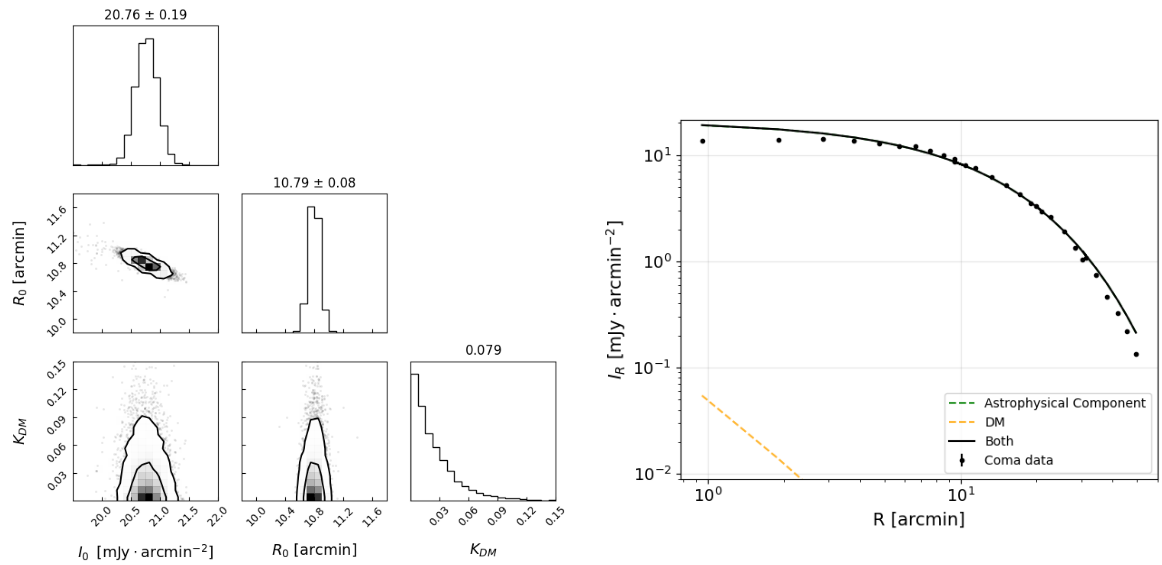

Figure 2.16 The left panel shows the posterior distributions and covariance of the astrophysical parameters I_0 and R_0, together with the 95% CL upper limit on the dark matter parameter K_{DM} (see Eq. 2.9). The right panel shows the best-fit astrophysical (green dashed) and dark matter (orange dashed) components. The data points represent the observations, while the total model (black solid) is nearly indistinguishable from the astrophysical component alone.

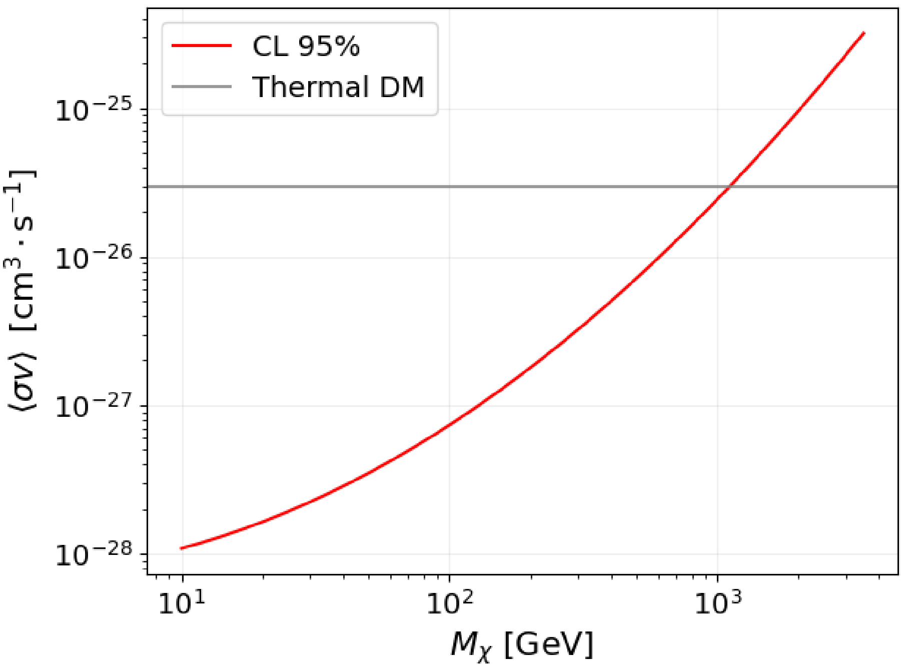

Figure 2.17 Constraints on the WIMP annihilation cross-section and mass, derived from the Coma Cluster data. Assuming a thermal annihilation cross-section (grey line), the allowed WIMP mass is larger than ~ 1 TeV (red line).

Chapter 3

Abell 2199

Abell 2199 is a promising candidate for the search for dark matter annihilation signatures. It is a nearby and massive galaxy cluster that does not exhibit strong diffuse radio emission.

The remainder of this chapter is divided into three parts. First, in Section 3.1, we introduce the main properties of Abell 2199, such as its virial mass, virial radius, and magnetic field. Second, in Section 3.2 we describe the processing of the radio observational data. Finally, in Section 3.3 we explain how the astrophysical information was extracted from the processed data and how the diffuse radio-emission component was determined. Next, we show how these results were used to derive constraints on the WIMP parameters.

3.1 Abell 2199 Galaxy Cluster

Abell 2199 (A2199 hereafter, see Fig. 3.1) is a galaxy cluster in the Hercules constellation, located at RA $= 16^h28^m38.0^s$ and Dec $= +39°32'55''$, with a redshift $z = 0.030$, corresponding to a luminosity distance of 128 Mpc (Sereno and Ettori, 2015).

Based on ROSAT (ROntgenSATellit, Truemper, 1982) X-ray observations, Markevitch et al. (1999) determined the gas temperature profile of A2199. The average temperature, corrected for the presence of cooling flows, is 4.8 ± 0.2 keV (90% CL). From the temperature profile they also derived the total gas and virial mass profile by solving the hydrostatic equilibrium equation within the X-ray core radius of 30 arcmin. The basic principles of this approach are discussed in Section 1.2.2.

Girardi et al. (1998) proposed a method based on the virial theorem and optical observations to estimate the dynamical mass of galaxy clusters (see also Section 1.2.2). Using this prescription, Rines et al. (2002) investigated the kinematics of cluster galaxies and estimated a virial radius of $r_v = 1.6h_{100}^{-1} = 2.4$ Mpc and a corresponding virial mass within r_v of $M_v = 5.34 \cdot 10^{14} h_{100}^{-1} M_\odot = 7.97 \cdot 10^{14} M_\odot$ with 30% uncertainty. According to Rines et al. (2002), the two methods—one based on galaxy kinematics and the other on the hydrostatic equilibrium equation—yield different results, with the latter giving mass estimates that are approximately a factor of two lower.

A2199 hosts a bright radio source, 3C 338, which is an FR-I radio galaxy associated with the bright central galaxy NGC 6166 (Burns et al., 1983). Vacca et al. (2012) used the VLA observations to measure the Faraday rotation toward 3C 338 to constrain the magnetic field (the method has been discussed in Section 1.A). They found that the magnetic field power spectrum follows a power law with an index of $n = 2.8 \pm 1.3$, between a maximum and minimum fluctuation scale of $\Lambda_{max} = 35 \pm 28$ kpc and $\Lambda_{min} = 0.7 \pm 0.1$ kpc, respectively. By including X-ray cavities coincident with the radio lobes in their modeling, they derived a magnetic field strength of $B_0 = 11.7 \pm 9.0$ μG at the cluster center. The field strength

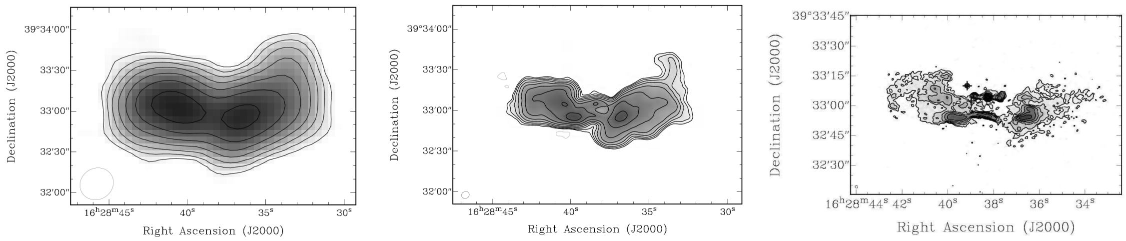

(a) 74 MHz. **(b)** 330 MHz. **(c)** 8400 MHz.

Figure 3.1 VLA observations of Abell 2199 at three different frequencies from Gentile et al. (2007). The contour levels are 0.35 (5σ), 0.7, 1.4, 2.8 ... Jy/beam, 5 (4.5σ), 10, 20, 40 ... mJy/beam and are 32 (4σ), 64, 128, 256, ... μJy/beam respectively.

decreases with radius, following the gas density profile with $\eta = 0.9 \pm 0.5$:

$$\langle B(r) \rangle = \langle B_0 \rangle \left(\frac{n_e(r)}{n_0} \right)^{\eta}, \tag{3.1}$$

where $n_e(r)$ is the electron number density as a function of radius and n_0 is its central value. Vacca et al. (2012) adopted a double β-model to estimate the electron number density, motivated by the central excess observed in the density profile:

$$n_e(r) = n_{0,int} \left(1 + \frac{r^2}{r_{c,int}^2} \right)^{-\frac{3}{2}\beta_{int}} + n_{0,ext} \left(1 + \frac{r^2}{r_{c,ext}^2} \right)^{-\frac{3}{2}\beta_{ext}}, \tag{3.2}$$

where r_c is the characteristic number density scale radius. This model was originally introduced by Mohr et al. (1999) as an empirical prescription that fits the observations better than a single β-model. Physically, however, it can be read as a superposition of two gas components: a centrally concentrated component with $n_{0,\mathrm{int}} = 74^{+4}_{-10} \times 10^{-3}\,\mathrm{cm}^{-3}$ and $r_{c,\mathrm{int}} = 9^{+2}_{-3}$ kpc, and a more extended component with $n_{0,\mathrm{ext}} = 27^{+3}_{-3} \times 10^{-3}\,\mathrm{cm}^{-3}$ and $r_{c,\mathrm{ext}} = 26^{+0.8}_{-6.0}$ kpc.

The virial mass and radius, as well as the magnetic field distribution, allow us to estimate the J-factor (Eq. 1.78), and consequently, to predict the expected signal from dark matter annihilation. For convenience, these parameters are summarized in Table 3.1.

3.2 LOFAR Data Processing

This section describes the steps of the radio data processing.

3.2.1 Data Extraction

The second LOFAR Two-metre Sky Survey (LoTSS-DR2, Shimwell et al., 2022) consists of more than 800 pointings and covers more than 5,000 square degrees of the sky. Each pointing was observed for 8 h across the 120–168 MHz frequency range. The average data volume of a single 8-hour observation is approximately 8.8 TB. All observations are hosted in the LOFAR Long Term Archive.

The data have been firstly calibrated using the standard direction-independent calibration pipeline (van Weeren et al., 2016). This pipeline corrects for effects such as station clock offsets, ionospheric Faraday rotation, XX–YY phase and amplitude calibration uncertainties.

The direction-independent calibrated observations were averaged to resulting in a time resolution of 8 s and a frequency resolution of 0.195 MHz. Subsequently, a direction-dependent calibration pipeline (DDFacet; Tasse et al., 2018; Shimwell et al., 2019) was applied to correct for ionospheric distortions.

Abell 2199

Parameter	**Value**
M_{vir} 10^{14} $[M_\odot]$	8.0 ± 2.4
R_{vir} [Mpc]	2.4 ± 0.7
R_{vir} [arcmin]	64 ± 19
Distance [Mpc]	128
B_0 [μG]	11.7 ± 9.0
η	0.9 ± 0.5
r_c [kpc]	9^{+2}_{-3}, $26^{+0.8}_{-6}$
$n_e(0)$ $[10^{-3}\,\mathrm{cm}^{-3}]$	$74^{+0.4}_{-1}$, 27^{+3}_{-3}
β	$1.5^{+0.2}_{-0.5}$, $0.39^{+0.01}_{-0.03}$

Table 3.1 Abell 2199 galaxy cluster parameters, summarized from Section 3.1, assuming $h_0 = 0.67$ (Planck Collaboration et al., 2020). The last five parameters describe the electron number density and magnetic field. The electron number density was obtained using a double-β model. For the parameters r_c, $n_e(0)$, and β, two values are given, corresponding to the inner and outer components of the model.

To reduce the data volume, Dysco compression (Offringa, 2016) was applied, typically decreasing the storage size by a factor of five.

According to Shimwell et al. (2022), the nominal sensitivity of the final LoTSS DR2 images is approximately 100 μJy/beam at a central frequency of 144 MHz, which has been achieved in about $\sim 70\%$ of the survey area.

The target of interest (A2199) is not located at the center of any LoTSS pointing. We downloaded visibility data containing the cluster within 2 degrees from the observing center (van Weeren et al., 2021), to avoid significant time and bandwidth smearing effects, and rephased the visibilities to the cluster center coordinates.

This selection results in three LoTSS pointings covering the target (P235+38, P235+40, and P238+40). Sources located farther than 15 arcmin from the phase center were subtracted by applying the direction-dependent calibration solutions to the sky model derived during the direction-independent calibration step.

3.2.2 Self-calibration Process

After data extraction, the calibration procedure had already been applied to the downloaded visibilities. Here, we performed an additional self-calibration step to further refine the calibration solutions. First, we produced a dirty image (see Fig. 3.2) to verify the source position and to estimate the PSF size, which was used to set the image pixel scale for all three datasets.

We adopted a pixel size of 1 arcsec to satisfy the Nyquist sampling criterion. This choice is based on a synthesized PSF with major- and minor-axis FWHM values of 3.4 and 2.2 arcsec, respectively, at 144 MHz, and a theoretical angular resolution of 3.1 arcsec at the same frequency, as given by Eq. 1.93. The virial radius of the cluster is of the order of 3800 arcsec, which is comparable to the adopted image size of 4000 $\times$ 4000 arcsec. Therefore, the field of view covers a substantial fraction of the cluster environment, including its central region. In particular, the expected dark matter annihilation signal is predicted to extend over angular scales of approximately 60–600 arcsec (see Section 3.3).

We then proceeded with the cleaning process using WSClean (Offringa et al., 2014) and used the multi-scale deconvolution algorithm (Offringa and Smirnov, 2017).

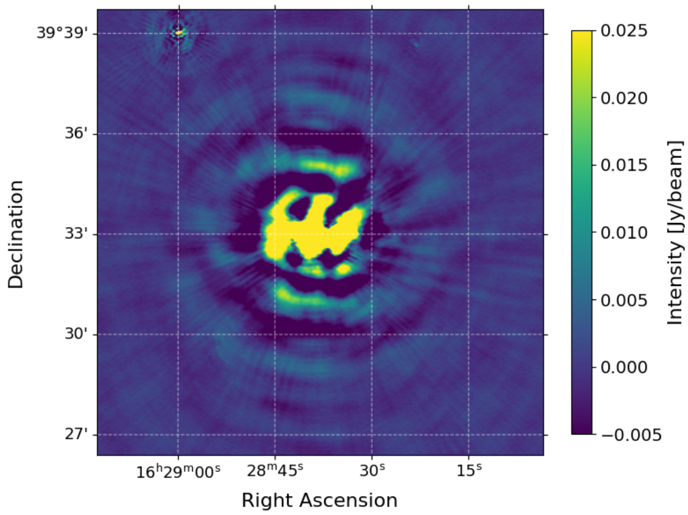

Figure 3.2 Dirty image of the central region of the Abell 2199 galaxy cluster at 144 MHz.

The central source was found to have a complex structure and to be bright, with a total flux density of approximately 70 Jy. During the deeper cleaning, we identified a significant number of imaging artifacts. Therefore, we adopted an absolute flux threshold 30 mJy, corresponding to the highest level of the sidelobes of 3C 338 measured from the dirty image. At this stage, we constructed the initial sky model for self-calibration.

3C 338 is present in three pointings (P235+38, P235+40, and P238+40). However, based on a measurement of the dynamic range in each field we excluded P235 + 38 and P235 + 40, as they exhibited dynamic ranges that were 1.5 and 2.1 times worse, respectively, than those of P238 + 40. In addition, the first two pointings showed a large scatter in the phase solutions over the second half of the observation period.

To improve the image quality, we performed additional flagging of corrupted visibilities using AOFlagger (Offringa et al., 2012) with the default LOFAR-HBA strategy (Fig. 3.3). This additional flagging step removed 23% of the visibilities. Furthermore, the RS508HBA station was fully flagged due to excessively noisy calibration solutions (Fig. 3.4), which resulted in the removal of a further 1.8% of the data.

The previously derived sky model was subsequently used for phase calibration, which helped to better focus the emission. The calibration solutions were determined over time intervals of 10 minutes and frequency intervals of 5 MHz, corresponding to a division of the full bandwidth into roughly 10 spectral sub-bands.

Solving equation 1.91, the complex gains $G_i(t, \nu)$ for each antenna were computed (see Fig. 3.4) and then combined in baseline gains $G_{ij}(\nu, t)$ to be applied to visibilities. This procedure was carried out using the Default Pre-Processing Pipeline (DP3, van Diepen et al., 2018).

We then repeated the imaging process, obtaining an updated sky model (Left panel Fig. 3.5). The phase calibration procedure described above was subsequently repeated two additional times. During the second iteration, additional data obtained after subtracting the model from the calibrated data in the visibility space were flagged; however, the additional fraction of flagged data was small (1–2%). In the third iteration, no additional flagging was applied.

At each step, the image quality improved, with a progressive increase of the dynamic range. At this stage, the final model was represented by 59 point-like and Gaussian sources (abs threshold 100 mJy) which described the central radio source and one distant source. Using this sky model we then applied amplitude and phase self-calibration (Right panel Fig. 3.5). This calibration was applied to initial extracted and flagged visibilities, to avoid convergence

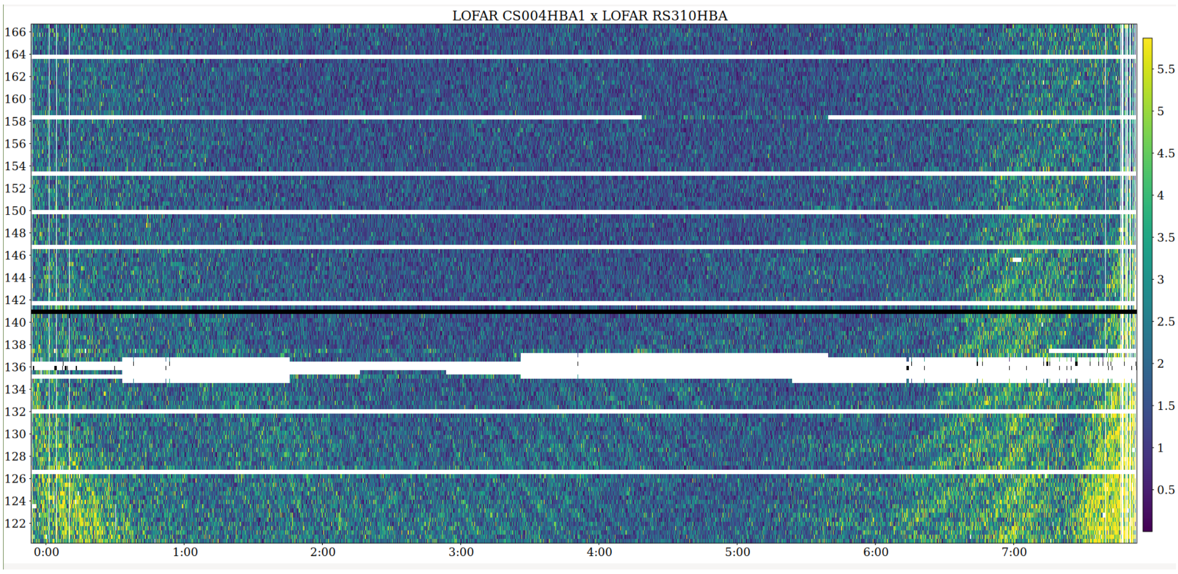

Figure 3.3 Amplitude of XX visibilities for the baseline between CS004HBA1 and RS310HBA (baseline length of 51.8 km). Data flagged during the LoTSS processing are shown in black, while data flagged in our additional flagging step are shown in white.

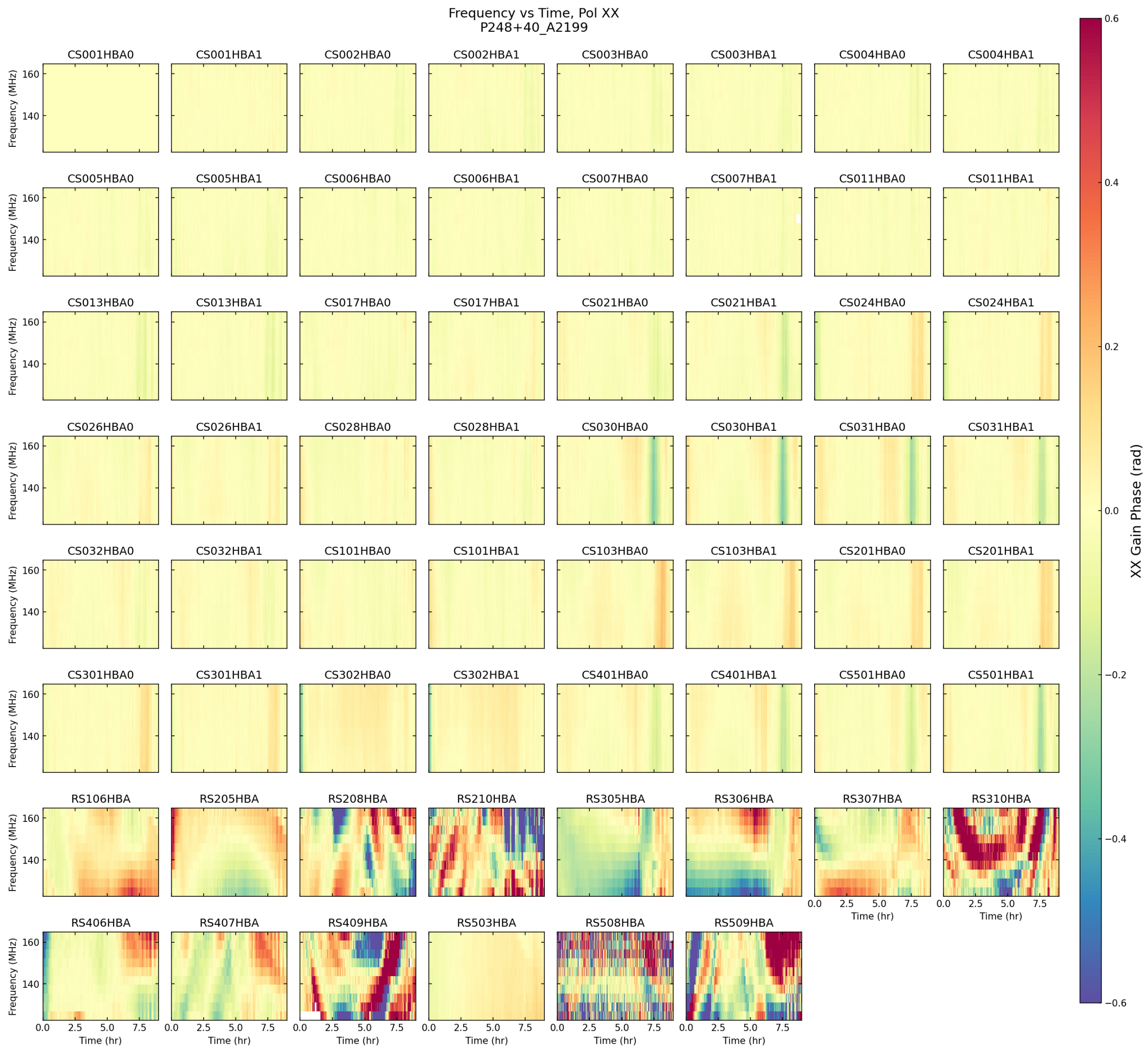

Figure 3.4 Gains solutions for a phase calibration. XX polarization.

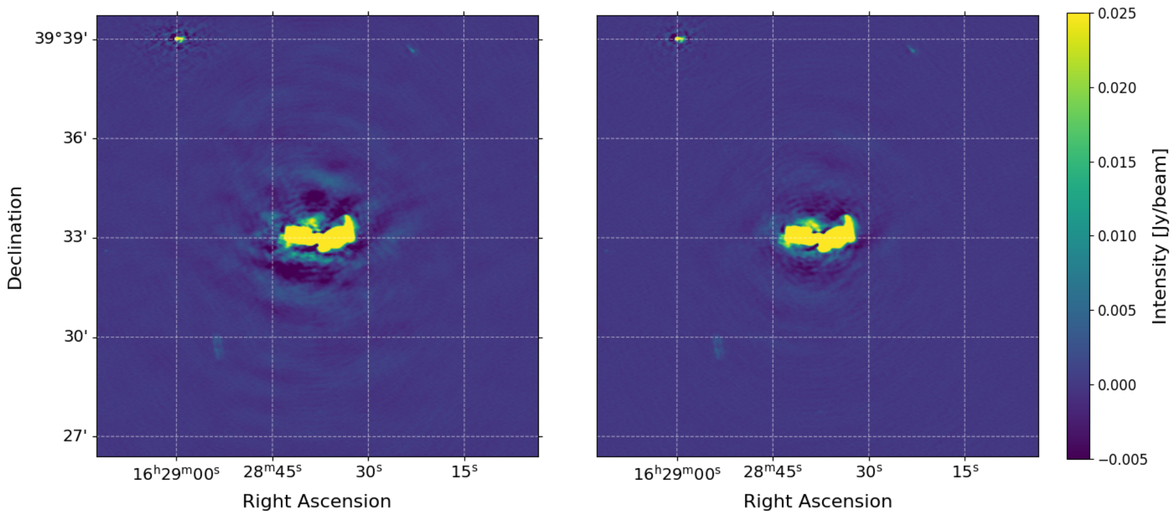

Figure 3.5 Comparison of A2199 images at different calibration stages. The left one after phase calibration and the right one after amplitude and phase calibration. Images are cropped around the central source. The images correspond to the P238+40 pointing.

to a local minimum in the gain solutions. In total we applied three steps of amplitude-phase calibration.

3.2.3 Image Deconvolution and Sky Model Construction

Significant calibration artifacts and sidelobes remained around the central source after self-calibration. To suppress them, we applied a clean mask defined by contours at the 21 mJy/beam level (three times the local RMS around the source). This provided a compromise between excluding regions dominated by artifacts and avoiding overly restrictive constraints on the deconvolution.

Since the residuals are dominated by artifacts in the vicinity of 3C 338, the standard deviation of the residual image is not isotropic and varies significantly across the field, ranging from 1—1.5 mJy/beam. in the eastern and southern regions up to 7 mJy/beam toward the northern and western directions from the source. The thermal noise level, measured far from the central source, is approximately 0.2 mJy/beam.

The final sky model was obtained using deconvolution with an absolute threshold of 3 mJy. The previously defined mask around the target source was applied to suppress sidelobes.

3.2.4 Extraction of the Diffuse Emission

We completed the image calibration and constructed a sky model for the central source 3C 338, as well as for other point-like and extended sources. We generate residual images by subtracting the sky model.

We apply Briggs weighting with a robust parameter of 0 and a Gaussian taper with FWHM values of 5 and 10 arcsec in the uv-plane. The taper additionally down-weights the contribution of long baselines. Combined with the adopted visibility weighting, this results in PSFs with FWHM values of 12.4 and 21 arcsec, respectively.

The image with an angular resolution of 12.4 arcsec (Fig. 3.6) was used to estimate the diffuse emission.

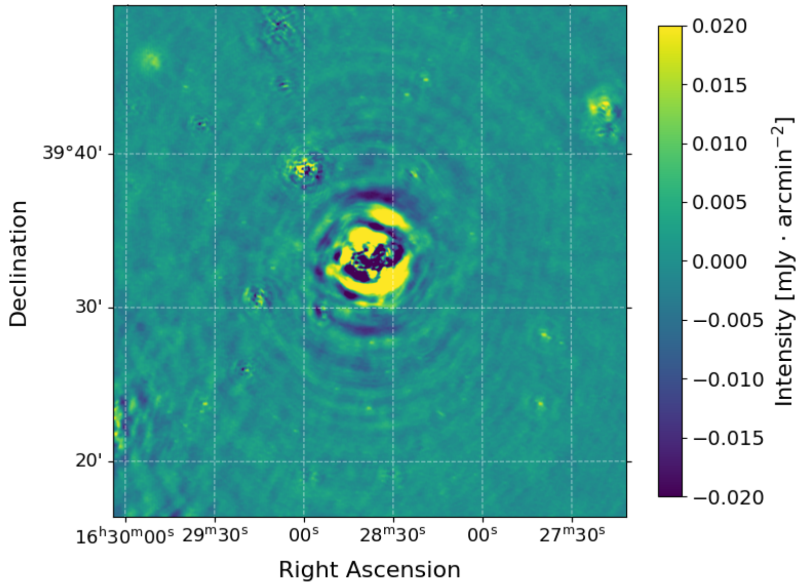

Figure 3.6 Residual image of 3C 338 obtained after sky model subtraction. The image was produced using Briggs weighting (robust = 0) and Gaussian tapering. The resulting synthesized beam is of 12.4 arcsec. Artifacts from the central source are still visible.

3.3 Constraints on WIMP Parameters

The residual image is contaminated by calibration artifacts and show no evidence of a DM-like signal (see Fig. 3.6).

We estimated the integrated flux density and the noise RMS within the region used for the dark matter analysis. This region is defined as the area enclosed by the predefined mask, which excludes the emission associated with 3C 338, and is further limited to the region containing 99% of the expected dark matter-induced synchrotron emission (Fig. 3.7). The size of the extraction region depends slightly on the WIMP mass, with its radius ranging from approximately 2.2 arcmin for a 10 GeV WIMP to 3.7 arcmin for a 10 TeV WIMP. The measured integrated flux densities and RMS noise levels are summarized in Table 3.2.

We add the simulated dark matter signal into the residual image and recompute the integrated flux density. As the dark matter signal increases with the annihilation cross section (Eq. 3.3), there exists a threshold cross section value above which the signal becomes detectable.

$$J_{\mathrm{D}M}(M_\chi, \langle\sigma v\rangle) = \frac{\langle\sigma v\rangle}{\langle\sigma v\rangle_0} J_{\mathrm{D}M}(M_\chi, \langle\sigma v\rangle_0). \tag{3.3}$$

For the reference model ($\langle\sigma v\rangle_0 = 10^{-26}\mathrm{cm}^3\mathrm{s}^{-1}$), we compute the integrated dark matter-induced flux $J_{\mathrm{D}M}(M_\chi)$ within the same region used for the observational flux estimation. The corresponding values are also reported in Table 3.2. Here we use the notation $J_{\mathrm{D}M}(M_\chi)$. A different notation is adopted compared with Chapter 2, since here we work with integrated flux densities in Jy rather than surface brightness in Jy/beam.

The dark matter emission was simulated using the *DarkMatters* code, adopting the parameters of the Abell 2199 cluster, the $b\bar{b}$ annihilation channel, a reference annihilation cross section of $\langle\sigma v\rangle_0 = 10^{-26}\,\mathrm{cm}^3\mathrm{s}^{-1}$, and WIMP masses of 10, 100 GeV, and 1 and 10 TeV (see Fig. 3.8).

To quantify this threshold, we consider the dark matter annihilation cross section for which the integrated flux density after the DM injection, J_{tot}, exceeds the residual integrated flux density by a factor of three (i.e., a signal-to-noise ratio of 3). This defines our detection criterion:

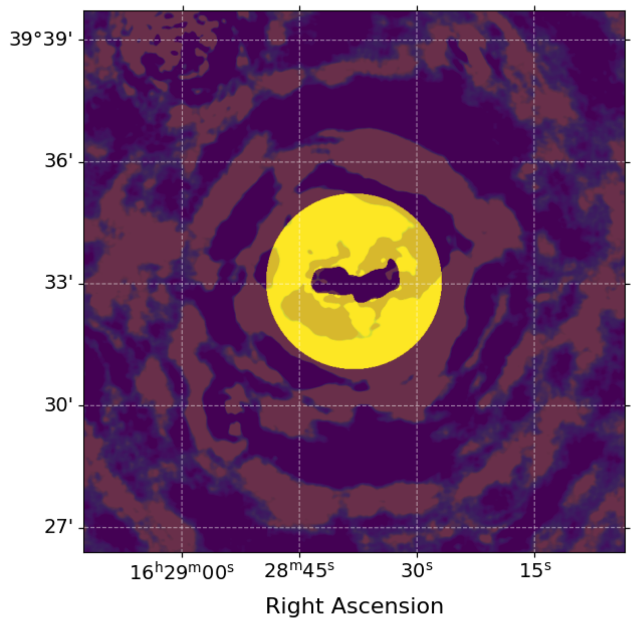

Figure 3.7 The yellow region indicates the area used for the signal estimation. This region is defined as the area outside the mask that includes the emission from 3C 338, and is further edged to the region enclosing 99% of the expected dark matter-induced emission. The result is shown for a WIMP mass of 10 GeV.

$$J_{\rm res} + J_{{\rm D}M} \geq {\rm SNR} \cdot J_{res}. \tag{3.4}$$

Using the relation between the WIMP annihilation cross section and the total dark matter flux (Eq. 3.3), and detection criteria (Eq. 3.4) we determine the annihilation cross section for which the dark matter signal becomes detectable.

$$\langle \sigma v \rangle = \langle \sigma v \rangle_0 \cdot ({\rm SNR} - 1) \cdot \frac{J_{\rm res}}{J_{\rm DM}(M_\chi, \langle \sigma v \rangle_0)}. \tag{3.5}$$

Assuming SNR = 3, for the lightest WIMP in our analysis, we determine the upper limit on the detectable cross section as $5 \cdot 10^{-25}\,{\rm cm}^3{\rm s}^{-1}$, see Fig. 3.9.

Then we repeat this procedure for all WIMP masses and construct the dependence of the WIMP annihilation cross section on the WIMP mass, see Fig. 3.10.

M_χ [GeV]	10	10^2	10^3	10^4
R [arcmin]	2.16	2.87	3.50	3.74
$J_{\rm res}$ [mJy]	640	810	994	1020
RMS [mJy]	7.7	8.2	8.6	8.7
$J_{\rm DM}$ [mJy]	26.6	6.2	0.32	8.9×10^{-3}

Table 3.2 In the table, R denotes the radius enclosing 99% of the expected DM-induced synchrotron emission, while $J_{\rm res}$ and RMS denote the total flux and image RMS at 144 MHz integrated within this region from the residual image. The $J_{\rm DM}$ denotes the integrated DM-induced flux density, assuming an annihilation cross section of $10^{-26}{\rm cm}^3{\rm s}^{-1}$. The values are computed for WIMP masses of 10, 100 GeV, 1 and 10 TeV.

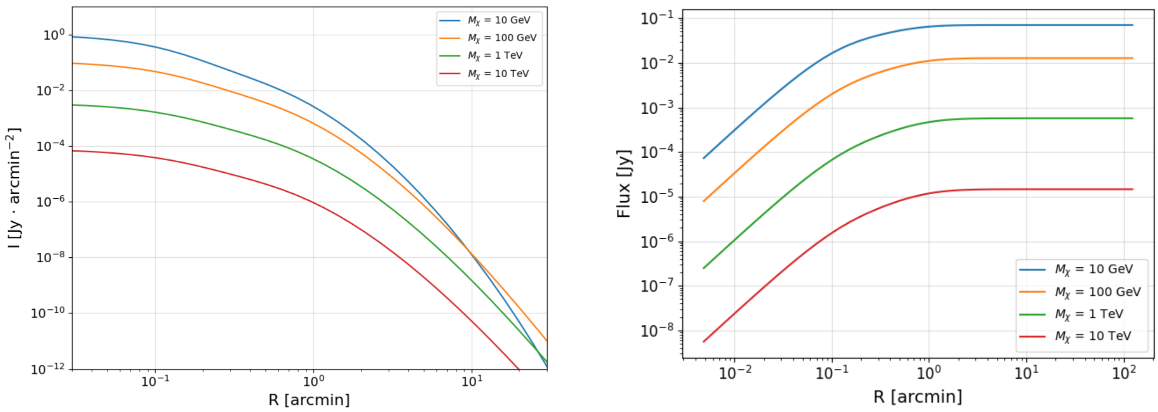

Figure 3.8 The left panel shows the simulated WIMP annihilation brightness profile for $b\bar{b}$ annihilation channel, annihilation cross section $10^{-26}\mathrm{cm}^3\mathrm{s}^{-1}$ and WIMP masses 10, 100 GeV, 1 and 10 TeV. The right panel shows the cumulative total flux in Jy as a function of distance from the source center.

Since the residual image is dominated by calibration artifacts associated with the imperfect subtraction of 3C 338, the derived upper limits should be regarded as conservative and primarily limited by systematic rather than thermal noise.

Ideally, if the source emission could be perfectly modeled and subtracted, the image noise would approach the RMS level. Now we compute the RMS noise over the area using the RMS noise in the image divided by the square root of the number of resolution elements included in the area. Repeating the same analysis under this assumption, we obtain

$$\langle \sigma v \rangle = \langle \sigma v \rangle_0 \cdot \mathrm{SNR} \cdot \frac{\mathrm{RMS}}{J_{\mathrm{D}M}(M_\chi, \langle \sigma v \rangle_0)} \tag{3.6}$$

This would allow significantly stronger constraints, reaching the thermal annihilation cross section for WIMP masses up to approximately 100 GeV (see Fig.3.10).

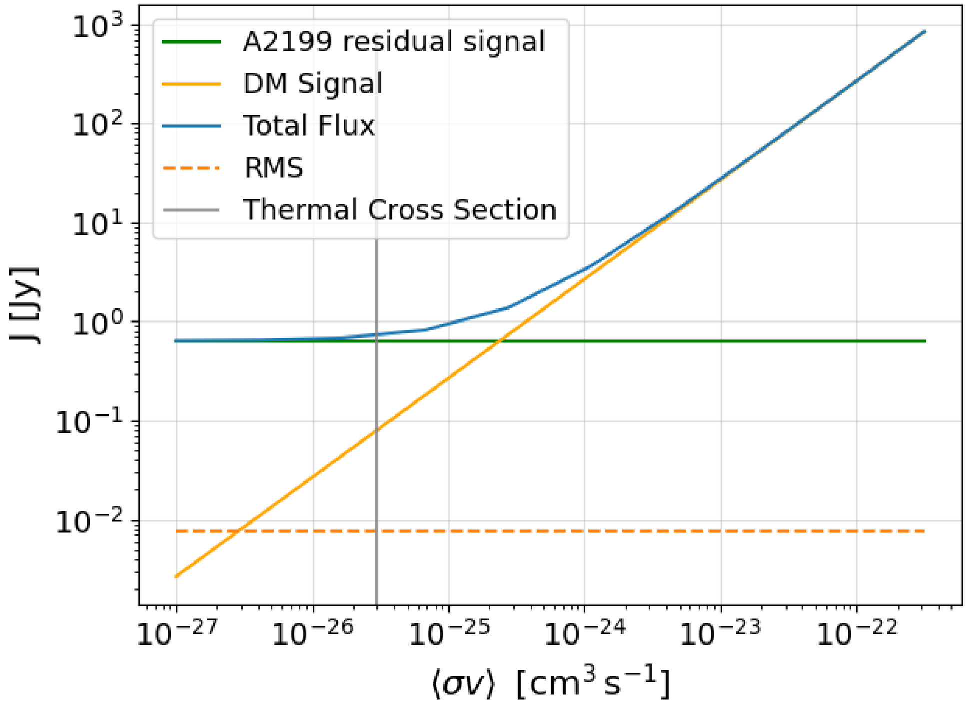

Figure 3.9 The DM-induced signal as a function of the WIMP annihilation cross section is shown by the yellow dashed line. The green solid line and the orange dashed line show the integrated residual flux and the RMS level, respectively. The blue solid line represents the sum of the DM-induced signal and the integrated residual flux. The thermal relic annihilation cross section is shown by the gray solid line.

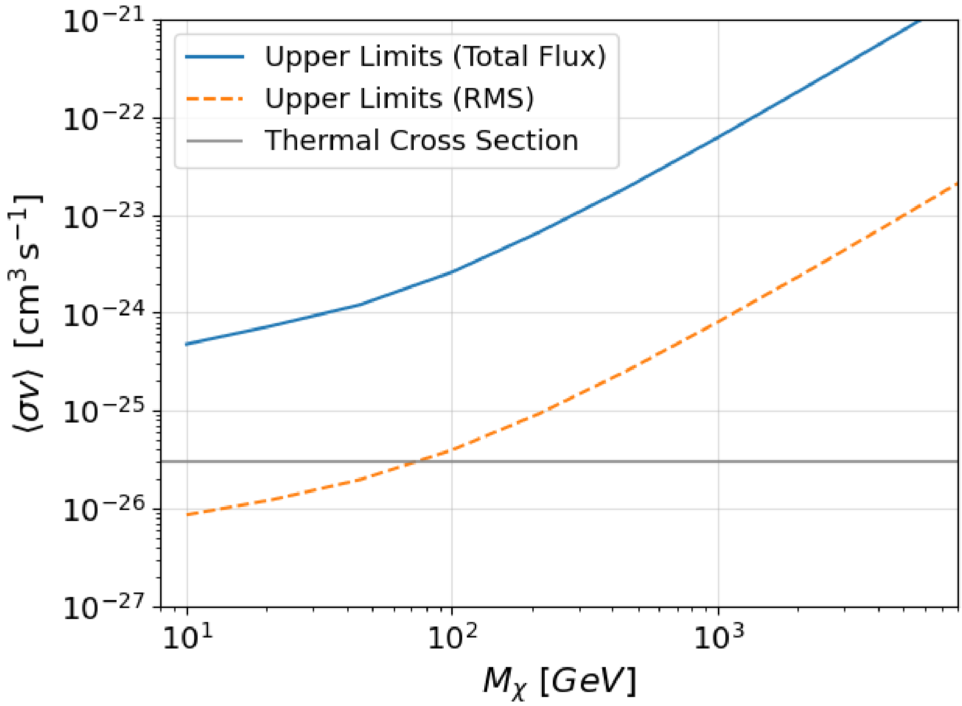

Figure 3.10 Upper limits on the WIMP annihilation cross section derived from the total residual flux (blue solid line) and the RMS level (orange dashed line) in the Abell 2199 observations. The thermal relic cross section is shown as a gray solid line.

Chapter 4

Conclusions

Dark matter remains one of the major unsolved problems of modern physics. In this thesis, the Weakly Interacting Massive Particle (WIMP) paradigm was investigated through radio observations of galaxy clusters. The study focused on the Coma and Abell 2199 clusters

We reviewed the main properties of dark matter, the mechanisms responsible for dark matter-induced synchrotron emission, and the principles of radio interferometric observations. Numerical simulations of the expected radio signal for different WIMP masses and annihilation channels were performed using the DarkMatters software package.

The analysis of radio emission signatures from dark matter annihilation is challenging because many astrophysical sources exhibit strong intrinsic radio emission unrelated to dark matter. A major difficulty is separating the potential dark matter contribution from conventional astrophysical emission. For the Coma cluster, the observed diffuse radio emission was modeled as a combination of an astrophysical component and a possible dark matter contribution. The analysis showed that the data are well described by the astrophysical component alone, with no statistically significant evidence for an additional dark matter signal. Nevertheless, upper limits on the dark matter contribution were derived, resulting in constraints on the WIMP annihilation cross section as a function of particle mass. Assuming the thermal annihilation cross section, the analysis disfavors WIMP masses below ~ 1 TeV at the 95% confidence level. This result is consistent with recent γ-ray and radio constraints. However, these confidence intervals account only for statistical uncertainties in the profile reconstruction. Systematic uncertainties from the magnetic field model, dark matter density profile are not included.

For Abell 2199, we analyzed 8-hour LOFAR observations at 144 MHz that were calibrated, imaged, and searched for diffuse radio emission. The detection of a diffuse component was complicated by the presence of a bright central bright (~ 70 Jy) source 3C 338 with a complex morphology. The final image was indeed affected by residual artifacts due to imperfect subtraction of 3C 338, limiting the sensitivity of the DM search. Upper limits on the WIMP annihilation cross section were derived from the residual image. For a WIMP mass of 10 GeV, we obtained an upper limit of approximately $10^{-24}\,\mathrm{cm}^3\,\mathrm{s}^{-1}$, which is about two orders of magnitude above the thermal annihilation cross section. Moreover, we demonstrate that improved source subtraction up to thermal noise level could significantly strengthen these constraints and potentially probe WIMP masses up to approximately 100 GeV assuming the thermal annihilation cross section.

Overall, no evidence for a dark matter-induced radio signal was found in either cluster. However, the study demonstrates that low-frequency radio observations provide a powerful approach to indirect dark matter searches. Future observations with improved calibration, deeper integrations, and next-generation facilities, such as the Square Kilometre Array (SKA), are expected to further improve the sensitivity of this method.

Acknowledgements

I would like to thank Dr. Gianni Bernardi for his wise and effective scientific supervision and for the opportunity to engage with real research at a high level. I am grateful for the opportunity to learn the subtleties of statistical data analysis, as well as the methods of scientific reasoning and practice.

I would like to thank Dr. Emillio Ceccotti for answering countless questions, for his constant willingness to help, guidance in the data reduction and presentation, and for pointing out mistakes and explaining how to correct them. I am also grateful for his introduction to the field of radio observation data processing. I wish Emilio great scientific progress and many significant achievements in his career.

I would also like to thank Andrey Egorov for consultations on dark matter phenomenology and for valuable suggestions regarding the relevant literature.

I am grateful to Prof.ssa Annalisa Bonafede for providing the Coma cluster data and for her support and enthusiasm throughout this work.

Finally, I would like to thank Prof. Franco Vazza for believing in me.

"*Perhaps the greatest triumph of human genius is that man can understand things that he can no longer imagine.*" — Lev Landau

Bibliography

Ackermann, M. et al. (May 2010). “Constraints on dark matter annihilation in clusters of galaxies with the Fermi large area telescope”. In: 2010.5, 025, p. 025. DOI: 10.1088/1475-7516/2010/05/025. arXiv: 1002.2239 [astro-ph.CO].

Alcock, C. et al. (Apr. 1995). “Experimental Limits on the Dark Matter Halo of the Galaxy from Gravitational Microlensing”. In: *Phys. Rev. Lett.* 74.15, pp. 2867–2871. DOI: 10.1103/PhysRevLett.74.2867. arXiv: astro-ph/9501091 [astro-ph].

Arlen, T. et al. (Oct. 2012). “Constraints on Cosmic Rays, Magnetic Fields, and Dark Matter from Gamma-Ray Observations of the Coma Cluster of Galaxies with VERITAS and Fermi”. In: *ApJ* 757.2, 123, p. 123. DOI: 10.1088/0004-637X/757/2/123. arXiv: 1208.0676 [astro-ph.HE].

Balazs, Csaba et al. (Jan. 2026). “A primer on dark matter”. In: *Encyclopedia of Astrophysics, Volume 5.* Vol. 5, pp. 17–32. DOI: 10.1016/B978-0-443-21439-4.00070-5. arXiv: 2411.05062 [astro-ph.CO].

Bergström, Lars, Joakim Edsjö, and Paolo Gondolo (Nov. 1998). “Indirect detection of dark matter in km-size neutrino telescopes”. In: *Phys. Rev. D* 58.10, 103519, p. 103519. DOI: 10.1103/PhysRevD.58.103519. arXiv: hep-ph/9806293 [hep-ph].

Bernardi, G. et al. (Sept. 2016). “Bayesian constraints on the global 21-cm signal from the Cosmic Dawn”. In: *MNRAS* 461.3, pp. 2847–2855. DOI: 10.1093/mnras/stw1499. arXiv: 1606.06006 [astro-ph.CO].

Bertone, Gianfranco, Dan Hooper, and Joseph Silk (Jan. 2005). “Particle dark matter: evidence, candidates and constraints”. In: *Phys. Rep.* 405.5-6, pp. 279–390. DOI: 10.1016/j.physrep.2004.08.031. arXiv: hep-ph/0404175 [hep-ph].

Bertone, Gianfranco and Tim M. P. Tait (Oct. 2018). “A new era in the search for dark matter”. In: *Nature* 562.7725, pp. 51–56. DOI: 10.1038/s41586-018-0542-z. arXiv: 1810.01668 [astro-ph.CO].

Binney, J. and G. A. Mamon (July 1982). “M/L and velocity anisotropy from observations of spherical galaxies, or must M87 have a massive black hole ?” In: *MNRAS* 200, pp. 361–375. DOI: 10.1093/mnras/200.2.361.

Bird, A. J. et al. (Mar. 2016). “The IBIS Soft Gamma-Ray Sky after 1000 Integral Orbits”. In: *ApJS* 223.1, 15, p. 15. DOI: 10.3847/0067-0049/223/1/15. arXiv: 1601.06074 [astro-ph.HE].

Bonafede, A. et al. (Apr. 2010). “The Coma cluster magnetic field from Faraday rotation measures”. In: *A&A* 513, A30, A30. DOI: 10.1051/0004-6361/200913696. arXiv: 1002.0594 [astro-ph.CO].

Bonafede, A. et al. (July 2022). “The Coma Cluster at LOFAR Frequencies. II. The Halo, Relic, and a New Accretion Relic”. In: *ApJ* 933.2, 218, p. 218. DOI: 10.3847/1538-4357/ac721d. arXiv: 2203.01958 [astro-ph.HE].

Boxelaar, J. M., R. J. van Weeren, and A. Botteon (Apr. 2021). “A robust model for flux density calculations of radio halos in galaxy clusters: Halo-FDCA”. In: *Astronomy and Computing* 35, 100464, p. 100464. DOI: 10.1016/j.ascom.2021.100464. arXiv: 2103.08554 [astro-ph.CO].

Briel, U. G., J. P. Henry, and H. Boehringer (June 1992). "Observation of the Coma cluster of galaxies with ROSAT during the all-sky-survey." In: *A&A* 259, pp. L31–L34.

Buote, David A. et al. (July 2007). "The X-Ray Concentration-Virial Mass Relation". In: *ApJ* 664.1, pp. 123–134. DOI: 10.1086/518684. arXiv: astro-ph/0610135 [astro-ph].

Burns, J. O., E. Schwendeman, and R. A. White (Aug. 1983). "CD galaxy dynamics and an aged ridge (jet) in 3C 338." In: *ApJ* 271, pp. 575–585. DOI: 10.1086/161224.

Carr, Bernard et al. (Nov. 2021). "Constraints on primordial black holes". In: *Reports on Progress in Physics* 84.11, 116902, p. 116902. DOI: 10.1088/1361-6633/ac1e31. arXiv: 2002.12778 [astro-ph.CO].

Ciafaloni, Paolo et al. (Mar. 2011). "Weak corrections are relevant for dark matter indirect detection". In: 2011.3, 019, p. 019. DOI: 10.1088/1475-7516/2011/03/019. arXiv: 1009.0224 [hep-ph].

Cirelli, Marco, Alessandro Strumia, and Jure Zupan (June 2024). "Dark Matter". In: *arXiv e-prints*, arXiv:2406.01705, arXiv:2406.01705. DOI: 10.48550/arXiv.2406.01705. arXiv: 2406.01705 [hep-ph].

Cirelli, Marco et al. (Mar. 2011). "PPPC 4 DM ID: a poor particle physicist cookbook for dark matter indirect detection". In: 2011.3, 051, p. 051. DOI: 10.1088/1475-7516/2011/03/051. arXiv: 1012.4515 [hep-ph].

Clark, B. G. (Sept. 1980). "An efficient implementation of the algorithm 'CLEAN'". In: *A&A* 89.3, p. 377.

Clowe, Douglas et al. (Sept. 2006). "A Direct Empirical Proof of the Existence of Dark Matter". In: *ApJ* 648.2, pp. L109–L113. DOI: 10.1086/508162. arXiv: astro-ph/0608407 [astro-ph].

Colafrancesco, S., S. Profumo, and P. Ullio (Aug. 2006). "Multi-frequency analysis of neutralino dark matter annihilations in the Coma cluster". In: *A&A* 455.1, pp. 21–43. DOI: 10.1051/0004-6361:20053887. arXiv: astro-ph/0507575 [astro-ph].

Coles, Peter and Francesco Lucchin (2002). *Cosmology: The Origin and Evolution of Cosmic Structure, Second Edition.*

Cornwell, T. J. (Nov. 2008). "Multiscale CLEAN Deconvolution of Radio Synthesis Images". In: *IEEE Journal of Selected Topics in Signal Processing* 2.5, pp. 793–801. DOI: 10.1109/JSTSP.2008.2006388.

Cui, Xiangyi et al. (Nov. 2017). "Dark Matter Results from 54-Ton-Day Exposure of PandaX-II Experiment". In: *Phys. Rev. Lett.* 119.18, 181302, p. 181302. DOI: 10.1103/PhysRevLett.119.181302.

de Blok, W. J. G. et al. (Dec. 2008). "High-Resolution Rotation Curves and Galaxy Mass Models from THINGS". In: *AJ* 136.6, pp. 2648–2719. DOI: 10.1088/0004-6256/136/6/2648. arXiv: 0810.2100 [astro-ph].

Dewdney, P. E. et al. (Aug. 2009). "The Square Kilometre Array". In: *IEEE Proceedings* 97.8, pp. 1482–1496. DOI: 10.1109/JPROC.2009.2021005.

Dhawan, Suhail, Saurabh W. Jha, and Bruno Leibundgut (Jan. 2018). "Measuring the Hubble constant with Type Ia supernovae as near-infrared standard candles". In: *A&A* 609, A72, A72. DOI: 10.1051/0004-6361/201731501. arXiv: 1707.00715 [astro-ph.CO].

Dodelson, Scott and Fabian Schmidt (2020). *Modern Cosmology.* DOI: 10.1016/C2017-0-01943-2.

Egorov, Andrei E. (July 2022). "Updated constraints on WIMP dark matter annihilation by radio observations of M31". In: *Phys. Rev. D* 106.2, 023023, p. 023023. DOI: 10.1103/PhysRevD.106.023023. arXiv: 2205.01033 [astro-ph.CO].

— (Aug. 2023). "Nature of M31 gamma-ray halo in relation to dark matter annihilation". In: *Phys. Rev. D* 108.4, 043028, p. 043028. DOI: 10.1103/PhysRevD.108.043028. arXiv: 2305.07590 [astro-ph.HE].

Ellingson, S. W. et al. (Aug. 2009). "The Long Wavelength Array". In: *IEEE Proceedings* 97.8, pp. 1421–1430. DOI: 10.1109/JPROC.2009.2015683.

Feretti, Luigina et al. (May 2012). "Clusters of galaxies: observational properties of the diffuse radio emission". In: *A&A Rev.* 20, 54, p. 54. DOI: 10.1007/s00159-012-0054-z. arXiv: 1205.1919 [astro-ph.CO].

Foreman-Mackey, Daniel et al. (Mar. 2013). "emcee: The MCMC Hammer". In: *PASP* 125.925, p. 306. DOI: 10.1086/670067. arXiv: 1202.3665 [astro-ph.IM].

Fukuda, Y. et al. (Aug. 1998). "Evidence for Oscillation of Atmospheric Neutrinos". In: *Phys. Rev. Lett.* 81.8, pp. 1562–1567. DOI: 10.1103/PhysRevLett.81.1562. arXiv: hep-ex/9807003 [hep-ex].

Gaskins, Jennifer M. (Oct. 2016). "A review of indirect searches for particle dark matter". In: *Contemporary Physics* 57.4, pp. 496–525. DOI: 10.1080/00107514.2016.1175160. arXiv: 1604.00014 [astro-ph.HE].

Gavazzi, R. et al. (May 2009). "A weak lensing study of the Coma cluster". In: *A&A* 498.2, pp. L33–L36. DOI: 10.1051/0004-6361/200911841. arXiv: 0904.0220 [astro-ph.CO].

Geller, M. J., Antonaldo Diaferio, and M. J. Kurtz (May 1999). "The Mass Profile of the Coma Galaxy Cluster". In: *ApJ* 517.1, pp. L23–L26. DOI: 10.1086/312024. arXiv: astro-ph/9903305 [astro-ph].

Gentile, G. et al. (Apr. 2007). "Monitoring the Bidirectional Relativistic Jets of the Radio Galaxy 3C 338". In: *ApJ* 659.1, pp. 225–234. DOI: 10.1086/512479. arXiv: astro-ph/0612233 [astro-ph].

Geringer-Sameth, Alex, Savvas M. Koushiappas, and Matthew G. Walker (Apr. 2015). "Comprehensive search for dark matter annihilation in dwarf galaxies". In: *Phys. Rev. D* 91.8, 083535, p. 083535. DOI: 10.1103/PhysRevD.91.083535. arXiv: 1410.2242 [astro-ph.CO].

Girardi, Marisa et al. (Sept. 1998). "Optical Mass Estimates of Galaxy Clusters". In: *ApJ* 505.1, pp. 74–95. DOI: 10.1086/306157. arXiv: astro-ph/9804187 [astro-ph].

Greisen, Eric W., Kristine Spekkens, and Gustaaf A. van Moorsel (June 2009). "Aperture Synthesis Observations of the Nearby Spiral NGC 6503: Modeling the Thin and Thick H I Disks". In: *AJ* 137.6, pp. 4718–4733. DOI: 10.1088/0004-6256/137/6/4718. arXiv: 0902.0989 [astro-ph.GA].

Griest, Kim and Marc Kamionkowski (Feb. 1990). "Unitarity limits on the mass and radius of dark-matter particles". In: *Phys. Rev. Lett.* 64.6, pp. 615–618. DOI: 10.1103/PhysRevLett.64.615.

Gunn, James E. and J. Richard Gott III (Aug. 1972). "On the Infall of Matter Into Clusters of Galaxies and Some Effects on Their Evolution". In: *ApJ* 176, p. 1. DOI: 10.1086/151605.

Gupta, Y. et al. (Aug. 2017). "The upgraded GMRT: opening new windows on the radio Universe". In: *Current Science* 113.4, pp. 707–714. DOI: 10.18520/cs/v113/i04/707-714.

Hamaker, J. P., J. D. Bregman, and R. J. Sault (May 1996). "Understanding radio polarimetry. I. Mathematical foundations." In: *A&AS* 117, pp. 137–147.

Hastings, W. K. (Apr. 1970). "Monte Carlo Sampling Methods using Markov Chains and their Applications". In: *Biometrika* 57.1, pp. 97–109. DOI: 10.1093/biomet/57.1.97.

Hawking, S. W. (Mar. 1974). "Black hole explosions?" In: *Nature* 248.5443, pp. 30–31. DOI: 10.1038/248030a0.

Hegyi, Dennis J. and Keith A. Olive (June 1983). "Can galactic halos be made of baryons?" In: *Physics Letters B* 126.1-2, pp. 28–32. DOI: 10.1016/0370-2693(83)90009-6.

Högbom, J. A. (June 1974). "Aperture Synthesis with a Non-Regular Distribution of Interferometer Baselines". In: *A&AS* 15, p. 417.

Hogg, David W. et al. (May 2005). "Cosmic Homogeneity Demonstrated with Luminous Red Galaxies". In: *ApJ* 624.1, pp. 54–58. DOI: 10.1086/429084. arXiv: astro-ph/0411197 [astro-ph].

Jungman, G., M. Kamionkowski, and K. Griest (Mar. 1996). “Supersymmetric dark matter”. In: *Phys. Rep.* 267, pp. 195–373. DOI: 10.1016/0370-1573(95)00058-5. arXiv: hep-ph/9506380 [hep-ph].

Kent, S. M. and J. E. Gunn (July 1982). “The dynamics of rich clusters of galaxies. I. The Coma cluster.” In: *AJ* 87, pp. 945–960. DOI: 10.1086/113178.

Kolmogorov, A. (Jan. 1941). “The Local Structure of Turbulence in Incompressible Viscous Fluid for Very Large Reynolds’ Numbers”. In: *Akademiia Nauk SSSR Doklady* 30, pp. 301–305.

Kubo, Jeffrey M. et al. (Dec. 2007). “The Mass of the Coma Cluster from Weak Lensing in the Sloan Digital Sky Survey”. In: *ApJ* 671.2, pp. 1466–1470. DOI: 10.1086/523101. arXiv: 0709.0506 [astro-ph].

Lewis, Antony and Sarah Bridle (Nov. 2002). “Cosmological parameters from CMB and other data: A Monte Carlo approach”. In: *Phys. Rev. D* 66.10, 103511, p. 103511. DOI: 10.1103/PhysRevD.66.103511. arXiv: astro-ph/0205436 [astro-ph].

Łokas, Ewa L. and Gary A. Mamon (Aug. 2003). “Dark matter distribution in the Coma cluster from galaxy kinematics: breaking the mass-anisotropy degeneracy”. In: *MNRAS* 343.2, pp. 401–412. DOI: 10.1046/j.1365-8711.2003.06684.x. arXiv: astro-ph/0302461 [astro-ph].

Lonsdale, C. J. et al. (Aug. 2009). “The Murchison Widefield Array: Design Overview”. In: *IEEE Proceedings* 97.8, pp. 1497–1506. DOI: 10.1109/JPROC.2009.2017564. arXiv: 0903.1828 [astro-ph.IM].

Marinacci, Federico et al. (Nov. 2018). “First results from the IllustrisTNG simulations: radio haloes and magnetic fields”. In: *MNRAS* 480.4, pp. 5113–5139. DOI: 10.1093/mnras/sty2206. arXiv: 1707.03396 [astro-ph.CO].

Markevitch, M. et al. (Dec. 1999). “Mass Profiles of the Typical Relaxed Galaxy Clusters A2199 and A496”. In: *ApJ* 527.2, pp. 545–553. DOI: 10.1086/308124. arXiv: astro-ph/9904382 [astro-ph].

Metropolis, Nicholas et al. (June 1953). “Equation of State Calculations by Fast Computing Machines”. In: *J. Chem. Phys.* 21.6, pp. 1087–1092. DOI: 10.1063/1.1699114.

Mohr, Joseph J., Benjamin Mathiesen, and August E. Evrard (June 1999). “Properties of the Intracluster Medium in an Ensemble of Nearby Galaxy Clusters”. In: *ApJ* 517.2, pp. 627–649. DOI: 10.1086/307227. arXiv: astro-ph/9901281 [astro-ph].

Mróz, Przemek et al. (Aug. 2024). “No massive black holes in the Milky Way halo”. In: *Nature* 632.8026, pp. 749–751. DOI: 10.1038/s41586-024-07704-6. arXiv: 2403.02386 [astro-ph.GA].

Murgia, M. et al. (June 2009). “Comparative analysis of the diffuse radio emission in the galaxy clusters A1835, A2029, and Ophiuchus”. In: *A&A* 499.3, pp. 679–695. DOI: 10.1051/0004-6361/200911659. arXiv: 0901.1943 [astro-ph.CO].

Navarro, Julio F., Carlos S. Frenk, and Simon D. M. White (May 1996). “The Structure of Cold Dark Matter Halos”. In: *ApJ* 462, p. 563. DOI: 10.1086/177173. arXiv: astro-ph/9508025 [astro-ph].

Niikura, Hiroko et al. (Apr. 2019). “Microlensing constraints on primordial black holes with Subaru/HSC Andromeda observations”. In: *Nature Astronomy* 3, pp. 524–534. DOI: 10.1038/s41550-019-0723-1. arXiv: 1701.02151 [astro-ph.CO].

Offringa, A. R. (Nov. 2016). “Compression of interferometric radio-astronomical data”. In: *A&A* 595, A99, A99. DOI: 10.1051/0004-6361/201629565. arXiv: 1609.02019 [astro-ph.IM].

Offringa, A. R. and O. Smirnov (Oct. 2017). “An optimized algorithm for multiscale wideband deconvolution of radio astronomical images”. In: *MNRAS* 471.1, pp. 301–316. DOI: 10.1093/mnras/stx1547. arXiv: 1706.06786 [astro-ph.IM].

Offringa, A. R., J. J. van de Gronde, and J. B. T. M. Roerdink (Mar. 2012). “A morphological algorithm for improving radio-frequency interference detection”. In: *A&A* 539, A95, A95. DOI: 10.1051/0004-6361/201118497. arXiv: 1201.3364 [astro-ph.IM].

Offringa, A. R. et al. (Oct. 2014). “WSCLEAN: an implementation of a fast, generic wide-field imager for radio astronomy”. In: *MNRAS* 444.1, pp. 606–619. DOI: 10.1093/mnras/stu1368. arXiv: 1407.1943 [astro-ph.IM].

Okabe, Nobuhiro et al. (Apr. 2014). “Subaru Weak-lensing Survey of Dark Matter Subhalos in the Coma Cluster: Subhalo Mass Function and Statistical Properties”. In: *ApJ* 784.2, 90, p. 90. DOI: 10.1088/0004-637X/784/2/90. arXiv: 1304.2399 [astro-ph.CO].

Perley, R. A. et al. (Sept. 2011). “The Expanded Very Large Array: A New Telescope for New Science”. In: *ApJ* 739.1, L1, p. L1. DOI: 10.1088/2041-8205/739/1/L1. arXiv: 1106.0532 [astro-ph.IM].

Perlmutter, S. et al. (June 1999). “Measurements of Ω and Λ from 42 High-Redshift Supernovae”. In: *ApJ* 517.2, pp. 565–586. DOI: 10.1086/307221. arXiv: astro-ph/9812133 [astro-ph].

Planck Collaboration et al. (Sept. 2020). “Planck 2018 results. VI. Cosmological parameters”. In: *A&A* 641, A6, A6. DOI: 10.1051/0004-6361/201833910. arXiv: 1807.06209 [astro-ph.CO].

Regis, Marco et al. (Oct. 2014). “Local Group dSph radio survey with ATCA (III): constraints on particle dark matter”. In: 2014.10, pp. 016–016. DOI: 10.1088/1475-7516/2014/10/016. arXiv: 1407.4948 [astro-ph.CO].

Regis, Marco et al. (Apr. 2015). “Local Group dSph radio survey with ATCA - II. Non-thermal diffuse emission”. In: *MNRAS* 448.4, pp. 3747–3765. DOI: 10.1093/mnras/stv127. arXiv: 1407.5482 [astro-ph.GA].

Regis, Marco et al. (Nov. 2021). “The EMU view of the Large Magellanic Cloud: troubles for sub-TeV WIMPs”. In: 2021.11, 046, p. 046. DOI: 10.1088/1475-7516/2021/11/046. arXiv: 2106.08025 [astro-ph.HE].

Riess, Adam G. et al. (Sept. 1998). “Observational Evidence from Supernovae for an Accelerating Universe and a Cosmological Constant”. In: *AJ* 116.3, pp. 1009–1038. DOI: 10.1086/300499. arXiv: astro-ph/9805201 [astro-ph].

Rines, K. et al. (Sept. 2002). “Mass Profile of the Infall Region of the Abell 2199 Supercluster”. In: *AJ* 124.3, pp. 1266–1282. DOI: 10.1086/342344. arXiv: astro-ph/0206226 [astro-ph].

Rogstad, D. H. and G. S. Shostak (Sept. 1972). “Gross Properties of Five Scd Galaxies as Determined from 21-CENTIMETER Observations”. In: *ApJ* 176, p. 315. DOI: 10.1086/151636.

Rubin, V. C., W. K. Ford Jr., and N. Thonnard (Nov. 1978). “Extended rotation curves of high-luminosity spiral galaxies. IV. Systematic dynamical properties, Sa -> Sc.” In: *ApJ* 225, pp. L107–L111. DOI: 10.1086/182804.

Sarkis, Michael and Geoff Beck (Feb. 2025). “DarkMatters: A powerful tool for WIMPy analysis”. In: *Physics of the Dark Universe* 47, 101745, p. 101745. DOI: 10.1016/j.dark.2024.101745. arXiv: 2408.07053 [hep-ph].

Schwab, F. R. (July 1984). “Relaxing the isoplanatism assumption in self-calibration; applications to low-frequency radio interferometry”. In: *AJ* 89, pp. 1076–1081. DOI: 10.1086/113605.

Scrimgeour, Morag I. et al. (Sept. 2012). “The WiggleZ Dark Energy Survey: the transition to large-scale cosmic homogeneity”. In: *MNRAS* 425.1, pp. 116–134. DOI: 10.1111/j.1365-2966.2012.21402.x. arXiv: 1205.6812 [astro-ph.CO].

Sereno, Mauro and Stefano Ettori (July 2015). “CoMaLit - IV. Evolution and self-similarity of scaling relations with the galaxy cluster mass”. In: *MNRAS* 450.4, pp. 3675–3695. DOI: 10.1093/mnras/stv814.

Sharma, Sanjib (Aug. 2017). “Markov Chain Monte Carlo Methods for Bayesian Data Analysis in Astronomy”. In: *ARA&A* 55.1, pp. 213–259. DOI: 10.1146/annurev-astro-082214-122339. arXiv: 1706.01629 [astro-ph.IM].

Shimwell, T. W. et al. (Feb. 2019). “The LOFAR Two-metre Sky Survey. II. First data release”. In: *A&A* 622, A1, A1. DOI: 10.1051/0004-6361/201833559. arXiv: 1811.07926 [astro-ph.GA].

Shimwell, T. W. et al. (Mar. 2022). “The LOFAR Two-metre Sky Survey. V. Second data release”. In: *A&A* 659, A1, A1. DOI: 10.1051/0004-6361/202142484. arXiv: 2202.11733 [astro-ph.GA].

Smirnov, Juri and John F. Beacom (Aug. 2019). “Tev-scale thermal WIMPs: Unitarity and its consequences”. In: *Phys. Rev. D* 100.4, 043029, p. 043029. DOI: 10.1103/PhysRevD.100.043029. arXiv: 1904.11503 [hep-ph].

Sofue, Yoshiaki and Vera Rubin (Jan. 2001). “Rotation Curves of Spiral Galaxies”. In: *ARA&A* 39, pp. 137–174. DOI: 10.1146/annurev.astro.39.1.137. arXiv: astro-ph/0010594 [astro-ph].

Steigman, Gary, Basudeb Dasgupta, and John F. Beacom (July 2012). “Precise relic WIMP abundance and its impact on searches for dark matter annihilation”. In: *Phys. Rev. D* 86.2, 023506, p. 023506. DOI: 10.1103/PhysRevD.86.023506. arXiv: 1204.3622 [hep-ph].

Storm, Emma et al. (Apr. 2017). “Synchrotron Emission from Dark Matter Annihilation: Predictions for Constraints from Non-detections of Galaxy Clusters with New Radio Surveys”. In: *ApJ* 839.1, 33, p. 33. DOI: 10.3847/1538-4357/aa6748. arXiv: 1607.01049 [astro-ph.CO].

Tasse, C. et al. (Apr. 2018). “Faceting for direction-dependent spectral deconvolution”. In: *A&A* 611, A87, A87. DOI: 10.1051/0004-6361/201731474. arXiv: 1712.02078 [astro-ph.IM].

Taylor, G. B., C. L. Carilli, and R. A. Perley, eds. (Jan. 1999). *Synthesis Imaging in Radio Astronomy II.* Vol. 180. Astronomical Society of the Pacific Conference Series.

The, Lih Sin and Simon D. M. White (Dec. 1986). “The mass of the Coma cluster.” In: *AJ* 92, pp. 1248–1253. DOI: 10.1086/114258.

Thierbach, M., U. Klein, and R. Wielebinski (Jan. 2003). “The diffuse radio emission from the Coma cluster at 2.675 GHz and 4.85 GHz”. In: *A&A* 397, pp. 53–61. DOI: 10.1051/0004-6361:20021474. arXiv: astro-ph/0210147 [astro-ph].

Thompson, A. Richard, James M. Moran, and George W. Swenson Jr. (2017). *Interferometry and Synthesis in Radio Astronomy, 3rd Edition.* DOI: 10.1007/978-3-319-44431-4.

Thorpe-Morgan, Charles et al. (Apr. 2021). “Annihilating dark matter search with 12 yr of Fermi LAT data in nearby galaxy clusters”. In: *MNRAS* 502.3, pp. 4039–4047. DOI: 10.1093/mnras/stab208. arXiv: 2010.11006 [astro-ph.HE].

Tremaine, Scott and James E. Gunn (Feb. 1979). “Dynamical role of light neutral leptons in cosmology”. In: *Phys. Rev. Lett.* 42.6, pp. 407–410. DOI: 10.1103/PhysRevLett.42.407.

Truemper, J. (Jan. 1982). “The ROSAT mission”. In: *Advances in Space Research* 2.4, pp. 241–249. DOI: 10.1016/0273-1177(82)90070-9.

Udalski, A., M. K. Szymański, and G. Szymański (Mar. 2015). “OGLE-IV: Fourth Phase of the Optical Gravitational Lensing Experiment”. In: 65.1, pp. 1–38. DOI: 10.48550/arXiv.1504.05966. arXiv: 1504.05966 [astro-ph.SR].

Vacca, V. et al. (Apr. 2012). “The intracluster magnetic field power spectrum in A2199”. In: *A&A* 540, A38, A38. DOI: 10.1051/0004-6361/201116622. arXiv: 1201.4119 [astro-ph.CO].

van Diepen, Ger, Tammo Jan Dijkema, and André Offringa (Apr. 2018). *DPPP: Default Pre-Processing Pipeline.* Astrophysics Source Code Library, record ascl:1804.003. ascl: 1804.003.

van Haarlem, M. P. et al. (Aug. 2013). “LOFAR: The LOw-Frequency ARray”. In: *A&A* 556, A2, A2. DOI: 10.1051/0004-6361/201220873. arXiv: 1305.3550 [astro-ph.IM].

van Weeren, R. J. et al. (Mar. 2016). “LOFAR Facet Calibration”. In: *ApJS* 223.1, 2, p. 2. DOI: `10.3847/0067-0049/223/1/2`. arXiv: `1601.05422 [astro-ph.IM]`.

van Weeren, R. J. et al. (Feb. 2019). “Diffuse Radio Emission from Galaxy Clusters”. In: *Space Sci. Rev.* 215.1, 16, p. 16. DOI: `10.1007/s11214-019-0584-z`. arXiv: `1901.04496 [astro-ph.HE]`.

van Weeren, R. J. et al. (July 2021). “LOFAR observations of galaxy clusters in HETDEX. Extraction and self-calibration of individual LOFAR targets”. In: *A&A* 651, A115, A115. DOI: `10.1051/0004-6361/202039826`. arXiv: `2011.02387 [astro-ph.CO]`.

Vikhlinin, A. et al. (Apr. 2006). “Chandra Sample of Nearby Relaxed Galaxy Clusters: Mass, Gas Fraction, and Mass-Temperature Relation”. In: *ApJ* 640.2, pp. 691–709. DOI: `10.1086/500288`. arXiv: `astro-ph/0507092 [astro-ph]`.

Weekes, T. C. et al. (May 2002). “VERITAS: the Very Energetic Radiation Imaging Telescope Array System”. In: *Astroparticle Physics* 17.2, pp. 221–243. DOI: `10.1016/S0927-6505(01)00152-9`. arXiv: `astro-ph/0108478 [astro-ph]`.

Weltman, A. et al. (Jan. 2020). “Fundamental physics with the Square Kilometre Array”. In: *PASA* 37, e002, e002. DOI: `10.1017/pasa.2019.42`. arXiv: `1810.02680 [astro-ph.CO]`.

White, S. D. M. and M. J. Rees (May 1978). “Core condensation in heavy halos: a two-stage theory for galaxy formation and clustering.” In: *MNRAS* 183, pp. 341–358. DOI: `10.1093/mnras/183.3.341`.

Workman, R. L. et al. (Aug. 2022). “Review of Particle Physics”. In: *Progress of Theoretical and Experimental Physics* 2022.8, 083C01, p. 083C01. DOI: `10.1093/ptep/ptac097`.

Zarka, P. et al. (Dec. 2012). “LSS/NenuFAR: The LOFAR Super Station project in Nançay”. In: *SF2A-2012: Proceedings of the Annual meeting of the French Society of Astronomy and Astrophysics*. Ed. by S. Boissier et al., pp. 687–694.

Zwicky, F. (Jan. 1933). “Die Rotverschiebung von extragalaktischen Nebeln”. In: *Helvetica Physica Acta* 6, pp. 110–127.